CONTACT INDUCED MICRO-PLASTICITY NEAR SURFACE:

A NOVEL BOUNDARY ELEMENT TECHNIQUE

by

MAZEN DIAB

A dissertation submitted to the Graduate Faculty in Mechanical Engineering in partial fulfillment of the requirements for the degree of Doctor of Philosophy, The City University of New York

2010 (year degree awarded)

This manuscript has been read and accepted for the
Graduate Faculty in Engineering in satisfaction of the
dissertation requirement for the degree of Doctor of Philosophy.

Dr. Honghui Yu

Date

Chair of Examining Committee

Dr. Mumtaz Kassir

Date

Executive Officer

Dr. Feridun Delale

Dr. Benjamin Liaw

Dr. Jackie Li

Dr. Haim Waisman

Supervisory Committee

THE CITY UNIVERSITY OF NEW YORK

ABSTRACT

Contact Induced Micro-Plasticity near Surface:
A Novel Boundary Element Technique.

by

Mazen Diab

Adviser: Professor Honghui Yu

Contact induced micro-surface plasticity is of crucial importance in many applications, such as surface treatment via severe plastic deformation. A clear understanding of the evolution of dislocation structure near the surface and the mutual interactions among neighboring asperities is important in understanding micro-surface plasticity. In this dissertation, rough surfaces under contact are analyzed using a discrete dislocation model.

A new Boundary Element Method (BEM) that takes into consideration singular fields due to dislocations is derived to solve the boundary value problem. At the heart of this method, a complex variable boundary integral equation that is weakly singular. First order singular integral equations capable of measuring stresses accurately close to the surface are developed. The new method offers a unified approach where two-dimensional discrete dislocation boundary value problems are solved directly in a similar fashion as in two-dimensional elasticity.

Using the new technique, indentation of single crystals with rough surfaces by flat contacts is analyzed. Simulation results show the size effect where it is very hard to yield small size asperities. If only surface sources are activated, dislocations nucleated form surface-steps exhibit different behavior depending on the asperity width and spacing. For asperities of small widths and large spacing, dislocations nucleated from surface-steps form dipolar bands within which materials are inserted from the surface leading to the formation of zones with high compressive stresses. For asperities of large widths, dislocations nucleated form the surface segregate into anti-load and pro-load dislocations. Anti-load dislocations pile up under the surface leading to the formation of tensile spots at the edges of the asperities. When bulk material yields dislocations nucleated from bulk sources glide towards the surface and relieve the high compressive stresses that may develop within the shear bands. Also, they block the motion of dislocations nucleated from the surface making it harder for subsequent dislocations to nucleate from surface asperities. For small asperity width to asperity spacing ratios, a large material pile-up is observed on both sides of the asperity. For big ratios, deformation mode is similar to that of a plane strain compressions. Between these two modes materials experience shear band deformation.

DEDICATION

To my mom.

ACKNOWLEDGEMENTS

Before I started my Ph.D. journey, I was doing a Masters of Engineering at the City College of New York (CCNY). During the first two semesters, I took several mechanical engineering classes from which I learned a lot. At that time, I was still not able to define what I want from my studies other than the Master's degree. One class that may have changed my life forever is Theory of Plasticity that I took with Prof. Honghui Yu. Two semesters later, I started my Ph.D. studies with Prof. Yu and the main topic of my Ph.D. was plastic deformation of micro-surfaces. Prof. Yu is a remarkable mentor. He taught me how to think on my own. I am very grateful to him for his guidance, ideas, encouragement, understanding and support during the years towards the publication of this dissertation.

I also want to thank my committee members, Prof. Feridun Delale, Prof. Benjamin Liaw and Prof. Jackie Li for their guidance and support throughout the course of this research. I am especially thankful to Prof. Haim Waisman for reading my dissertation and for his helpful comments on my research work.

Thanks also go to my friends and colleagues at the department of Mechanical Engineering at CCNY. I am especially indebted to Prof. Gary Benenson with whom I had the chance to co-teach a class. He always volunteered to provide the support and the guidance whenever needed. Prof. Benenson is a great educator from whom and without any doubt I learned a lot about the role of an educator in shaping the future of his students.

Last but not least, I could have not completed this dissertation without the support and love of my family especially my mother Latifa, my wife Dana, and my sister Zoya. Thank you Dana

for always believing in me. Finally, all the love goes to my nephews, Ali and Karim, and my son, Jad. I promise you Jad that I will spend more time playing with you in the coming days.

TABLE OF CONTENTS

LIST OF TABLES

LIST OF FIGURES

CHAPTER 1

INTRODUCTION

1.1. Introduction

In many cases, material failures such as fatigue fracture, fretting fatigue, wear and corrosion occur on surfaces. Therefore the structure and properties of material surfaces have a tremendous impact on the global behavior and reliability of mechanical components. For this reason, surface treatments such as severe plastic deformation (SPD); e.g. ultrasonic shot-peening [1], high-energy shot peening [2], surface mechanical attrition treatment [3], surface nanocrystallization and hardening [4], air blast shot peening [5], wire brushing [6], friction sliding [7] and ultrasonic impact peening [8] have become more and more important in modern engineering applications.

Surfaces treated via severe plastic deformation methods have shown to develop a nanostructured layer at the surface (see Fig. 1.1). This phenomenon is known as surface nanocrystallization. The main concept of these techniques is to severely and randomly plastify the surface of bulk materials by subjecting the surface to repetitive high contact loads. The key issue is to generate walls of dislocations. These dislocations may annihilate, nucleate and rearrange into small angle grain boundaries that divide the original grains into randomly oriented finer grains (see Fig. 1.2).

Experimental evidences have shown that this nanostructured layer possesses novel properties and performances that are fundamentally different from its conventional coarse-grained polycrystalline counterparts, such as high hardness and strength, enhanced physical properties, improved tribological properties, and superplasticity at low temperatures [11-16].

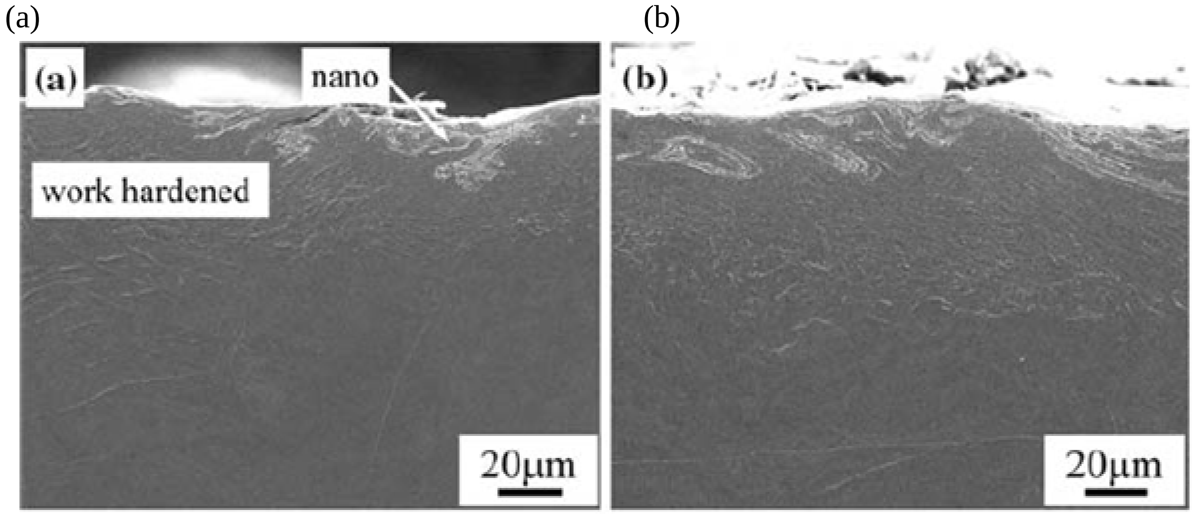

Figure 1.1. Microstructure of as shot peened Fe-3.29 Si with different coverage: (a) 3,000 %, (b) 10,000% [9].

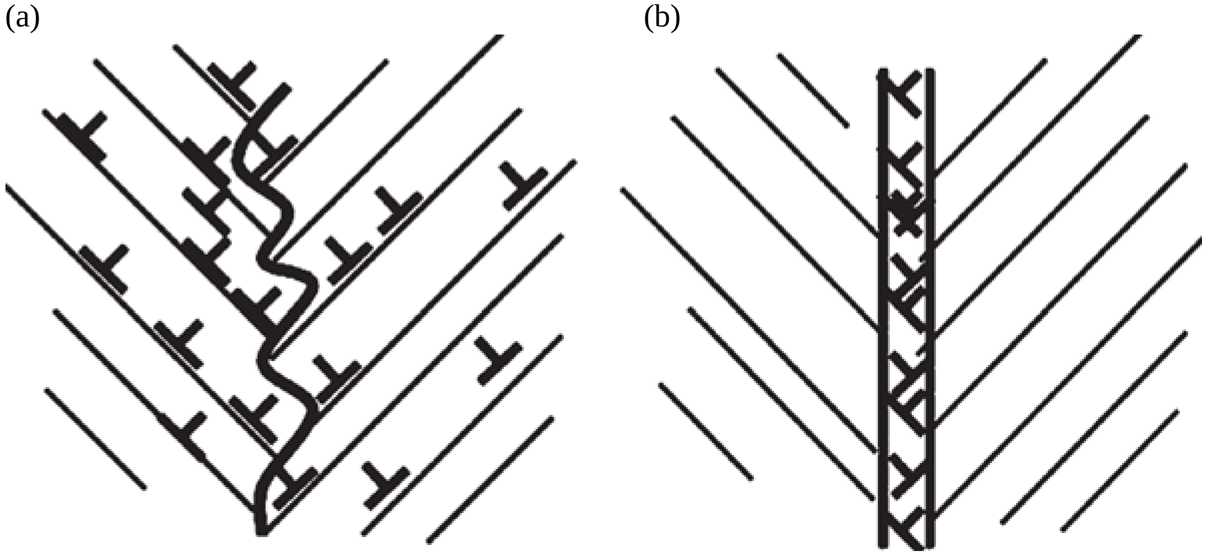

Figure 1.2. Arrangement of grain boundaries in nanostructured layers: (a) dislocation structure during SPD processing, (b) dislocation structure after SPD processing leading to the formation of nonequilibrium grain boundaries [10].

Despite the wealth of experimental evidences, there is still no theoretical framework to give a clear picture on the formation of the nanocrystalline surface layer. The reason is that the system is too complicate to be modeled. Material surfaces have roughness down to a very small scale at which continuum plasticity is not valid. Moreover, Material surfaces play the role of both sink and source for dislocations.

Surfaces are unavoidably rough and when two rough surfaces are pressed into contact, they meet only at their highest spots. Accordingly, the sizes of the resulting contact spots, the true contact pressure, and the true area of contact have to be predicted in a contact problem. The classic approach of rough surface contact is the Greenwood-Williamson model [17] that represents a rough surface as a collection of discrete spherical asperities with same radius of curvature but different heights and gives a statistical way to deduce multi-asperity contact from single-asperity contact. The statistical parameters of the model depend upon the measurement window and instrumentation resolution. However, surfaces are typically self-affine fractal and the Greenwood-Williamson model cannot describe fractal surfaces uniquely. Several models that adapt the Greenwood-Williamson model have been proposed to analyze fractal surfaces, e.g. [18-20], but they appear to suffer from the same difficulties as the original Greenwood-Williamson analysis: no unambiguous way to determine the surface profile. A big step forward was achieved recently by Ciavarella et al. [21]. They adopted the Weierstrass profile function to capture the multi-scale nature of surface roughness under elastic contact load. In this model, the true contact area of an elastic solid with a self-affine fractal surface consists of an infinite number of contact spots, each of zero size so that the total contact area is zero, but the pressure on each contact is infinite. Gao and Bower [22] has extended this approach to perform an elastic-plastic contact analysis of a fractal rough surface by a model of the Weierstrass-Archard type; see also Pei et al. [23].

The conventional plasticity theory fails to account for the dependence of the mechanical response on the size of the structure. This is due to the fact that the conventional plasticity theory relates the plastic strain at a point to the history of the deformation at that point without taking into consideration the possible interactions with other material points in the vicinity of that point. There have been strong experimental evidences that at micron and sub-micron level, the yield strength increases as the length scale of the specimen decreases. Among these experiments, we name a few. Fleck et al [24] have showed a length scale hardening in micro-torsion test of thin copper wires (see Fig. 1.3).

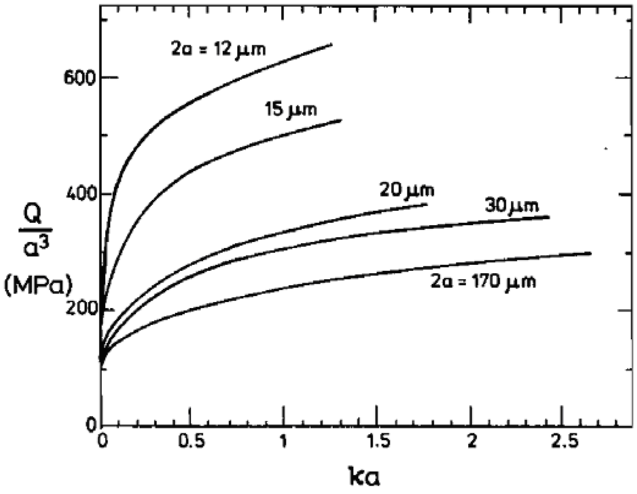

Figure 1.3. Torsional response of copper wires of diameter 2a in the range 12-170 μm. If the constitutive law were independent of strain gradients, the plots of normalized torque Q/a^3 vs. κa would all lie on the same curve, where κa is the twist per unit length of the wire [24].

Furthermore, bending of thin beams was reported by Stolken and Evans [25]. Moreover, micro/nano-indentation hardness experiments have repeatedly revealed the increase of indentation hardness with the decrease of indentation depth [26-28]. The size dependency is believed to be due to the following mechanisms: (i) strain gradients leading to geometrically necessary dislocations, (ii) obstacles to dislocation glide leading to boundary layers, (iii) limited number of sources and of obstacles to glide leading to dislocation starvation.

Extensive work has been conducted in the last two decades in order to derive a non-local continuum theory to account for the size effects [29-33]. All of these proposed formulations have focused on representing in phenomenological constitutive relation size effects that stem from geometrically necessary dislocations arising from strain gradients. Some of the formulations have accounted for the boundary layer mechanism by introducing additional boundary conditions and balance conditions. However, a continuum framework that accounts for the size effects arising due to dislocation starvation is still lacking.

In the absence of a well developed continuum framework to catch the heterogeneity of plastic deformation at nano/micro scale and the limitations of the atomistic simulations to sizes less than hundred nanometers and time scales less than tens of nanoseconds, transitional scales modeling techniques have become necessary to assess the reliability of mechanical components at small scales. Discrete dislocation plasticity in which the size effect is introduced implicitly through the material length and the Burgers vector has been used to bridge the gap between the length scales extremes.

With the advances in the computer speed and hardware, discrete dislocation plasticity has gained a tremendous popularity to study plastic deformations at small scales. Due to the large computational demands, three dimensional discrete dislocation simulations are still limited to small strains. Therefore, two-dimensional discrete dislocation plasticity has been used widely to gain qualitative understandings of materials deformation at small scales. Some examples of what can be done in three dimensions are illustrated in [34-39].

1.2. Contact Induced Plasticity of Material Surfaces

During the last two decades, a variety of discrete dislocation plasticity studies have been carried out to investigate the size dependency of microscopic asperity contacts [40-44]. Most of these studies have dealt with isolated asperities under contact loading partly due to the wide application of micro- and nano-indentation measurements. Below is a summary of these studies.

1.2.1. Discrete Dislocation Plasticity Studies

Polonsky and Keer [40] were the pioneers in using discrete dislocation plasticity to investigate the scale effects of elastic-plastic asperity micro-contact. They have simulated ploughing tests of an initially flat surface by a sinusoidal rigid asperity. Simulations results revealed that when the asperity size becomes comparable to the dislocation source spacing, the asperity can sustain considerably higher loads than those predicted by continuum plasticity. Furthermore, they have concluded that below a certain threshold, the asperity deforms purely elastically. Kreuzer and Pippan et al. [41-42] have considered indentation by indenters of various shapes. Their model was limited to dislocations along slip planes parallel to the surface. Two cases with different dislocation source density were considered. The analysis has confirmed a major experimental finding that hardness decreases with increasing indentation. Also, they have noted that increasing the friction stress leads to dislocations pile-up at the sides of the indenter, and therefore the nominal hardness decreases. Moreover, they have showed that the shape of the indenter affects the indentation behavior of the material. Similarly, discrete dislocation plasticity calculations conducted by Widjaja et al. [43] showed that the indentation response of thin films with a cylindrical indenter is qualitatively different from that with the wedge indenters. A more detailed work of the indentation problem was reported by Balint et al. [44]. Their simulation results revealed size dependant indentation pressure that approaches the continuum plasticity solution for large contact sizes and the elastic solution for small contact sizes. None of these studies have considered the role of the surface as a source for dislocations. Dislocations were nucleated from material defects such as Frank-Read sources that were distributed randomly in the material bulk.

1.2.2. Theoretical Unit Step Model

An important feature of the material surface that differentiates it from the material bulk is that a surface can play the role of both sink and source for dislocations. It has been predicted theoretically [45-47] and observed experimentally [48-51] that dislocations can nucleate from surface-steps or ledges. These geometric features are stress concentration sources which lead to dislocation nucleation similar to dislocation nucleation from a crack tip [52-54].

In an attempt to understand micro-plastic deformation of rough surfaces under contact loading, Yu and his collaborators [47,55] have proposed a theoretical unit step model to study near surface plasticity under contact loading. They have modeled the surface roughness as a distribution of surface-steps. In Fig. 1.4, the Unit Step Model is sketched. The surface of solid I is assumed to be flat and rigid and the rough surface of solid II is modeled with a surface step. When the two solids are brought in contact, they perfectly bond outside a gap of size *a*. The right end of the gap is determined by matching the energy release rate and the work of adhesion as in the classic Griffith crack.

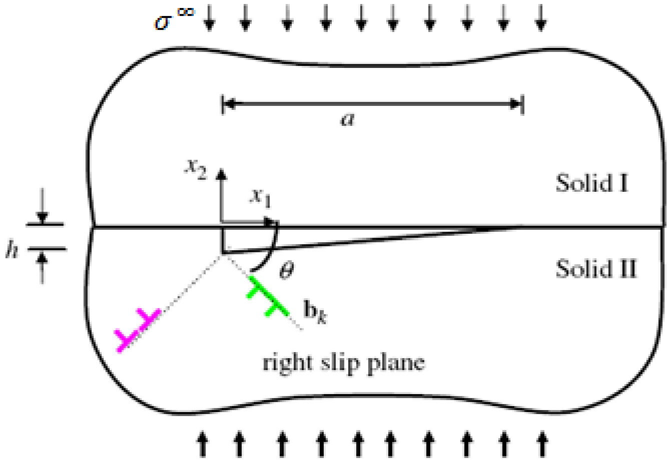

Figure 1.4. Schematic representation of a stepped solid (solid II) indented by a rigid plate (solid I) [55].

A dislocation can be nucleated and move out from the surface step. The driving force on the dislocation was calculated using conservation integrals. The effects of surface adhesion, step size and lattice resistance on the driving force were analyzed. The driving force in conjunction with the Rice-Thompson criterion [52] determines the threshold condition for dislocation nucleation and its final equilibrium position; i.e., the equilibrium distance from the dislocation to the surface step. Fig. 1.5 shows the normalized equilibrium position l/b as a function of applied remote load ($-\sigma^\infty/c_{11}$) for two slip planes at angles of $\theta = -\pi/4$ and $\theta = -3\pi/4$ respectively. In the figure, h is the step height, Γ the work of adhesion at the interface, C_{11} the elastic stiffness, and G_p is the Peierls force. The two curves correspond to two different G_p. Along the slip plane at $\theta = -\pi/4$, dislocation emission occurs only after the normal load becomes larger than a threshold value. Once emitted, the dislocation is pushed closer to the step as the load increases. In contrast, along the slip plane at $\theta = -3\pi/4$, the dislocation is easy to nucleate and the distance between the dislocation and the surface step increases as the load increases. The results can be understood as follows. The forces on dislocation due to the surface step, gap, and interface all decay as the dislocation moves away from the step while the remote driving force is a constant, which tends to push dislocation up at slip plane of θ = -π/4 and down at θ = -3π /4. The dislocation stops when the total driving force is less than the Peierls force.

The equilibrium positions of the dislocations clearly indicate that dislocations nucleated from the surface step along different slip planes segregate. Under the normal contact load, the dislocations at slip planes at the right hand side of the step, for example, at θ = -π/4, are localized near the surface step while the dislocations along the slip planes at the other side are easily pushed away from the step. They named the former dislocations as anti-load dislocations and the latter ones as pro-load dislocations.

They also observed that slip planes, if acting separately, exhibit different hardening behavior. As shown by the two smooth curves in Fig. 1.6., this difference in the hardening behavior can be interpreted as follows: The slip plane at θ = -π/4 yields at an applied pressure of one order of magnitude easier than the slip plane at θ = -3π/4. However, dislocations nucleated along the slip plane at θ = -π/4 are of anti-load type and therefore they pile up close to the step and generate a large back stress which make**s** nucleation of subsequent dislocations very hard. In contrast, the dislocation nucleated along the slip plane at θ = -3π/4 are of pro-load type and therefore they move away from the step making it easier to nucleate subsequent dislocations. Interestingly, it was found that dislocation nucleation along one slip plane can make the dislocation nucleation along the other slip plane much easier. Thus, the critical applied pressure required was found to be an order of magnitude less than that needed in the case where nucleation was considered along a slip plane separately. This phenomenon is called latent softening and is shown in the stair-way like curve in Fig. 1.6.

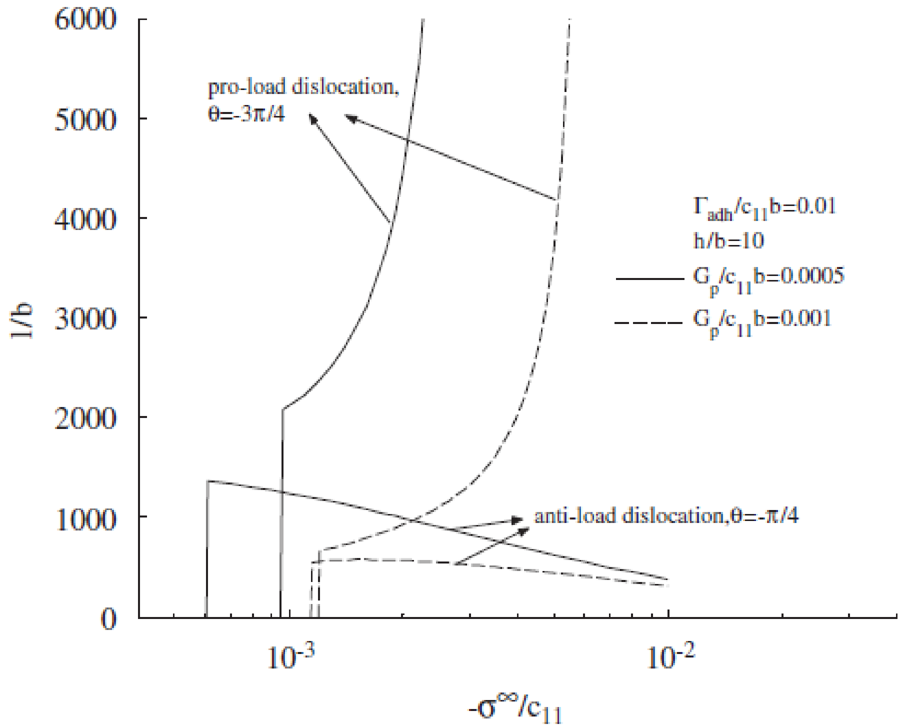

Figure 1.5. Equilibrium position (*l/b*) versus the applied remote load $(-\sigma^{\infty}/c_{11})$ for a dislocation moving along the slip plane at $\theta = -\pi/4$ or at θ = -π /4 [47].

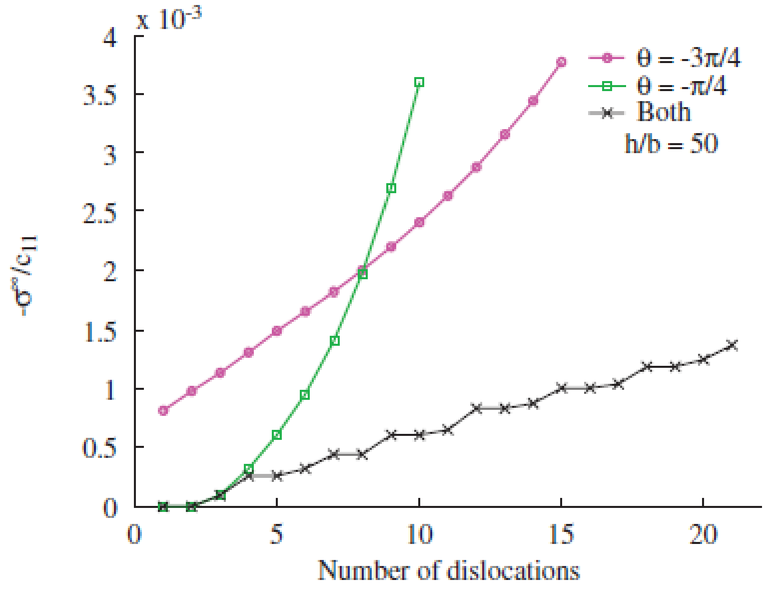

Figure 1.6. Applied remote load $(-\sigma^{\infty}/c_{11})$ versus number of dislocations nucleated along slip plane at θ = -π/4, θ = -3π/4 or both [55].

This analytical model has two major limitations. First, it simulates rough surfaces only under single asperity contact; thus interaction between different asperities is not taken into consideration. Second, it can deal with a very limited number of dislocations.

1.3. Statement of Dissertation Work

In this dissertation, a numerical model that is capable of measuring stresses accurately near the surface is developed. At the heart of this model is a complex variable boundary integral equation that is weakly singular. The numerical model takes into consideration singular fields due to the presence of dislocations in finite solids. Using this numerical model, boundary value problems are solved directly to predict size dependant plasticity in finite solids. A fast numerical code is created using C++ and Matlab.

A Multi-Asperities model is devised to study contact induced micro-plasticity under rough surfaces using the new boundary element technique. Interaction between neighboring asperities is modeled using periodic boundary conditions. Being aware of the complexity of the problem and the current knowledge on the subject, we adopt two approaches. First approach is to perform simple analysis to shed some lights on dislocation behavior underneath the contact area. Like the theoretical Unit-Step Model described above. Although, it is based on a very simplified analysis, it revealed important phenomena that helped us understand how the complicated dislocation structure evolves near the surface. Second approach is to conduct large scale simulations where yield of both material surface and bulk is considered. Connection between deformation patterns and geometric properties of the rough surface, i.e., asperity size and spacing, is investigated.

1.4. Outline of the Dissertation

Chapter 2 presents the new boundary element formulation developed in this dissertation. Numerical schemes are developed and elastic benchmark problems are solved and compared to mechanics of materials results.

In Chapter 3, the new boundary element method is extended to take into consideration the singular fields due to dislocations. Thus, a new discrete dislocation approach is developed. The advantage of the new approach over existent approaches is discussed. Boundary value problems solved in the literature are solved to validate the proposed technique and show its robustness in solving size dependant plasticity in finite solids.

Chapter 4 presents a Multi-Asperities model that adopts the boundary element approach developed in Chapter 3. The model is used to analyze the dislocation behavior underneath the surface and the interaction among the various asperities. Only dislocation nucleation from surface-steps is considered in this chapter. The results obtained by Yu et al. and Gao et al. in [47,55] are checked using the new model. New observations are discussed and further improvements of the Multi-Asperities model are offered.

In Chapter 5, the Multi-Asperities model is extended to take into consideration nucleation of dislocations from bulk sources. Effect of dislocation nucleation from bulk sources on dislocation behavior and dislocation structure underneath the surface are discussed. Connection between mean contact pressure, deformation patterns and geometric properties of rough surfaces are investigated.

CHAPTER 2

A WEAKLY SINGULAR BOUNDARY ELEMENT METHOD

2.1. Introduction

The seminal work by Rizzo [56] was pioneering in deriving boundary integral equations for two dimensional boundary value problems. Rizzo's work was based on the application of Betti's reciprocal theorem to the fundamental solution of the Navier equations for an infinite three-dimensional medium subjected to a point force called the Kelvin solution. This formulation is known as the conventional boundary element formulation. The conventional boundary integral equation relates the displacement and the traction at the boundary. The traction kernel is first order singular and the displacement kernel is logarithmic singular. The Somigliana identity is used to calculate the displacement at an internal point; then after differentiating and applying Hook's law, the stress field can be computed at that internal point. The main drawback of this approach is that the displacement kernel in the Somigliana identity is second order singular, which makes the results of the stress field at internal points close to the boundary very poor. In addition, differentiating the displacement at internal points may introduce numerical errors. Gosh et al [57] used integration by parts to eliminate the first order singularity from the traction kernel and reformulate the conventional boundary integral equation in terms of the tangential gradient displacements $d\mathbf{u}/ds$ and the tractions $\mathbf{t}$ at the boundary. The proposed formulation is logarithmic singular. The stress field is first order singular and can be calculated directly from the values of tractions and gradient displacements at the boundary. This new approach showed a great advantage over the conventional boundary element in eliminating the so called boundary layer effect. Similar approach was also used by Wu et al. [58] for anisotropic materials. Okada et al. [59] solved boundary displacements and tractions by the conventional boundary element method, and then obtained internal stresses from the integrals involving the gradient of displacements and tractions at the boundary. Their numerical results showed that the integrals could calculate internal stresses accurately even when the points were extremely close to the boundary.

In this dissertation, we propose a unified set of complex boundary integral equations starting from the Stroh formulation and using the Cauchy integral theorem. Two boundary integral equations of this set are of main interest. The two equations are derived in terms of the tangential gradient displacements and the tractions at the boundary. We also derive integral equations for the stress field at any domain point in terms of the gradient displacements and tractions at the boundary. The complex forms of the integral equations allow the evaluation of these integrals analytically. The new formulation permits the direct calculation of stresses at any domain point from the boundary values. Moreover, The stress field integral equations are first order singular which eliminates the problem of the boundary layer effect as it will be shown later in this chapter.

This chapter is organized as follows. Section 2.2, reviews the fundamental Stroh formulation. In Section 2.3, we present the methodology followed to derive several boundary integral equations for two-dimensional anisotropic problems. Section 2.4 uses the approach followed by Yu and Yang [60] to deduce the isotropic forms of the derived equations. In Section 2.5, we discuss the numerical implementation of the isotropic formulations and offer expressions which are used to solve elastic problems numerically. Section 2.6 shows the results obtained for five elastic problems and discusses the accuracy of the results and the advantages of the new formulation in eliminating the boundary layer effect. Finally, in Section 2.7, a conclusion is provided.

2.2. Fundamental Formulation

It has been shown by Eshelby et al. [61], Stroh [62] and Lekhnitski [63] that for a two dimensional problem, i.e., with both geometry and external loading invariant in the direction normal to *xy*-plane, the elastic field can be represented in terms of three functions. These are the displacement u_i, stress σ_{ij}, and the resultant force T_i on an arc,

$$u_i = 2\,\mathrm{Re}[\sum_{\alpha=1}^{3} A_{i\alpha} f_\alpha(z_\alpha)] \quad ; \quad T_i = -2\,\mathrm{Re}[\sum_{\alpha=1}^{3} L_{i\alpha} f_\alpha(z_\alpha)] \tag{2.1}$$

$$\sigma_{2i} = 2\,\mathrm{Re}[\sum_{\alpha=1}^{3} L_{i\alpha} f'_\alpha(z_\alpha)] \quad ; \quad \sigma_{1i} = -2\,\mathrm{Re}[\sum_{\alpha=1}^{3} L_{i\alpha} p_\alpha f'_\alpha(z_\alpha)] \tag{2.2}$$

where function f_α is holomorphic in its argument, $z_\alpha = x + p_\alpha y$, and f'_α is its derivative with positive imaginary part, which can be solved as roots of the following sixth order polynomial,

$$\left| C_{i1k1} + pC_{i1k2} + pC_{i2k1} + p^2 C_{i2k2} \right| \tag{2.3}$$

where C_{ijkl} are the stiffness tensor of the material.

Each column of **A** is solved from the following eigenvalue problem,

$$\sum_{k=1}^{3} (C_{i1k1} + p_\alpha C_{i1k2} + p_\alpha C_{i2k1} + p_\alpha^2 C_{i2k2}) A_{k\alpha} = 0 \tag{2.4}$$

The matrix **L** is given by,

$$L_{i\alpha} = \sum_{k=1}^{3} [C_{i2k1} + p_\alpha C_{i2k2}] A_{k\alpha} \tag{2.5}$$

The notations used in this chapter follow those in Suo [64] who proved that the schemes derived by Lekhnitskii and Eshelby are consistent.

2.3. Boundary Integral Equations for Anisotropic Materials

Denote $\mathbf{f} \equiv [f_1(z_1), f_2(z_2), f_3(z_3)]^{\mathrm{T}}$, $\mathbf{u}$ as the displacement vector and $\mathbf{T}$ as the resultant force vector at the boundary of a solid. From Eq. (2.1), we have

$$\mathbf{u} = \mathbf{A} \cdot \mathbf{f} + \overline{\mathbf{A}} \cdot \bar{\mathbf{f}} \tag{2.6a}$$

$$-\mathbf{T} = \mathbf{L} \cdot \mathbf{f} + \overline{\mathbf{L}} \cdot \bar{\mathbf{f}} \tag{2.6b}$$

Eliminating $\bar{\mathbf{f}}$ from Eqs. (2.6a) and (2.6b), we get

$$\mathbf{f} = \mathbf{L}^{-1} \cdot (\mathbf{B} + \overline{\mathbf{B}})^{-1} \cdot [i\mathbf{u} - \overline{\mathbf{B}} \cdot \mathbf{T}] \tag{2.7}$$

where $\mathbf{B} = i\mathbf{A}\mathbf{L}^{-1}$ is a Hermitian matrix.

Denote $\partial\Omega$ as the boundary of a simply connected domain Ω in *z*-plane ($z = x + iy$, $i = \sqrt{-1}$) and $\partial\Omega_\alpha$ the image of $\partial\Omega$ in z_α-plane. For any internal point *z* in domain Ω, its image is $z_\alpha = x + p_\alpha y$ in z_α-plane. From Cauchy's theorem,

$$f_\alpha(z_\alpha) = \frac{1}{2\pi i} \oint_{\partial\Omega_\alpha} \frac{f_\alpha(\zeta_\alpha)}{\zeta_\alpha - z_\alpha} d\zeta_\alpha \tag{2.8}$$

We have $\mathbf{f}$ inside the solid as,

$$\mathbf{f} = \frac{1}{2\pi i} \oint_{\partial\Omega} \left\langle (C + p_\alpha S)/(\varsigma_\alpha - z_\alpha) \right\rangle \cdot \mathbf{L}^{-1} \cdot (\mathbf{B} + \overline{\mathbf{B}})^{-1} \cdot [i\mathbf{u} - \overline{\mathbf{B}} \cdot \mathbf{T}]\Big|_\zeta ds \tag{2.9}$$

where $\left\langle (C + p_\alpha S)/(\varsigma_\alpha - z_\alpha) \right\rangle$ is a diagonal matrix whose α-th diagonal component is $(C + p_\alpha S)/(\varsigma_\alpha - z_\alpha)$. ζ is a point on $\partial\Omega$ and ζ_α is its image on $\partial\Omega_\alpha$. $C = \cos(\theta)$, $S = \sin(\theta)$, θ is the tangent angle at ζ (Fig. 2.1) and *ds* is an infinitesimal arc length at $\partial\Omega$ so that $d\varsigma = (C + iS)ds$ and $d\varsigma_\alpha = (C + p_\alpha S)ds$. The original integrals in Eq. (2.8) along $\partial\Omega_\alpha$ are converted into integrations along $\partial\Omega$. In this chapter, $\langle * \rangle$ represents a diagonal matrix whose α-th diagonal component is indicated inside the bracket.

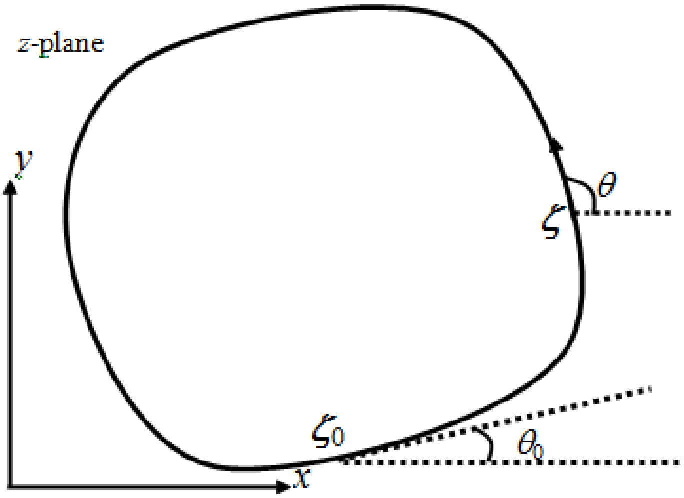

Figure 2.1. Boundary of a single connected domain in z-plane.

Integrating Eq. (2.9) by part and replacing $d\mathbf{T}/ds$ by the traction vector $\mathbf{t} = (t_x,t_y,t_z)^T$, yields the following expression for the holomorphic function,

$$\mathbf{f}\big|_z = -\frac{1}{2\pi i}\oint_{\partial\Omega}\left\langle \ln(\varsigma_\alpha - z_\alpha)\right\rangle \cdot \mathbf{L}^{-1}\cdot(\mathbf{B}+\overline{\mathbf{B}})^{-1}\cdot\left(i\frac{d\mathbf{u}}{ds}-\overline{\mathbf{B}}\cdot\mathbf{t}\right)\Big|_{\varsigma} ds + \mathbf{L}^{-1}\cdot(\mathbf{B}+\overline{\mathbf{B}})^{-1}\cdot(i\mathbf{u}-\overline{\mathbf{B}}\cdot\mathbf{T})\Big|_{\varsigma^{(r)}} \tag{2.10}$$

where $\varsigma^{(r)}$ is a reference point on the boundary used to determine the single value branch of the logarithmic functions. In Eq. (2.10), the single-valued branch-cut of $\ln(\varsigma_\alpha - z_\alpha)$ in z_α-plane is line from z_α and passing ς_α^r (Fig. A.1(a)), so that the argument of $(\varsigma_\alpha - z_\alpha)$ is from $\arg(\varsigma_\alpha^{(r)} - z_\alpha)$ to $\arg(\varsigma_\alpha^{(r)} - z_\alpha) + 2\pi$. In deriving the last term of Eq. (2.10), we assume the external loads on the boundary are self-equilibrated, ($\oint_{\partial\Omega}\mathbf{t}ds = 0$), so that $\mathbf{T}$ is periodic around the boundary.

The displacement field is obtained as:

$$\mathbf{u}\big|_{z} = -\frac{1}{\pi}\operatorname{Re}\oint_{\partial\Omega}\mathbf{A}\cdot\left\langle \ln(\varsigma_{\alpha}-z_{\alpha})\right\rangle\cdot\mathbf{L}^{-1}\cdot(\mathbf{B}+\overline{\mathbf{B}})^{-1}\cdot\left(\frac{d\mathbf{u}}{ds}+i\overline{\mathbf{B}}\cdot\mathbf{t}\right)\Bigg|_{\zeta} ds+\mathbf{u}\big|_{\varsigma^{(r)}} \qquad (2.11)$$

The stress field derived from Eq. (2.2) is

$$[\sigma_{21},\sigma_{22},\sigma_{23}]^{\mathrm{T}}\big|_{z} = \frac{1}{\pi}\operatorname{Re}\int_{\partial\Omega}\mathbf{L}\cdot\left\langle 1/(\varsigma_{\alpha}-z_{\alpha})\right\rangle\cdot\mathbf{L}^{-1}\cdot(\mathbf{B}+\overline{\mathbf{B}})^{-1}\cdot\left(\frac{d\mathbf{u}}{ds}+i\overline{\mathbf{B}}\cdot\mathbf{t}\right)\Bigg|_{\zeta} ds \qquad (2.12a)$$

$$[\sigma_{11},\sigma_{12},\sigma_{13}]^{\mathrm{T}}\big|_{z} = -\frac{1}{\pi}\operatorname{Re}\int_{\partial\Omega}\mathbf{L}\cdot\left\langle p_{\alpha}/(\varsigma_{\alpha}-z_{\alpha})\right\rangle\cdot\mathbf{L}^{-1}\cdot(\mathbf{B}+\overline{\mathbf{B}})^{-1}\cdot\left(\frac{d\mathbf{u}}{ds}+i\overline{\mathbf{B}}\cdot\mathbf{t}\right)\Bigg|_{\zeta} ds \qquad (2.12b)$$

Note that the integral kernels in Eq. (2.12) have *1/r* singularity.

If we only integrate by parts the integral part over the resultant force **T** in Eq. 2.9, we can obtain boundary integral equations in terms of the displacement **u** and the traction **t (**see Appendix A). By extracting the real parts of these boundary integral equations we obtain the boundary integral equations used in the conventional boundary element method [65]. However, the integral kernels will have ($1/r^2$) singularity (see Eqs. A.3(a) and (b)).

Thus, by integrating over the boundary in terms of the displacement gradient instead of the displacement, the singularity is reduced and therefore the new stress expressions provide very accurate stress measurements at internal points very close to the boundary.

For two dimensional elasticity, usually, only two independent boundary conditions are given at each single point along the boundary. We need to set up boundary integral equation to solve **u** and **t** along the boundary.

For a point $\zeta_0 = x_0 + iy_0$ at boundary $\partial\Omega$, its image is $\zeta_{\alpha}^{0} = x_0 + p_{\alpha} y_0$ at $\partial\Omega_{\alpha}$. For analytic function $f_{\alpha}(z_{\alpha})$, its boundary value is

$$f_{\alpha}(\zeta_{\alpha}^{0}) = \frac{1}{\pi i}\oint_{\partial\Omega_{\alpha}}\frac{f_{\alpha}(\zeta_{\alpha})}{\zeta_{\alpha}-\zeta_{\alpha}^{0}}d\zeta_{\alpha} \qquad (2.13)$$

Since ζ_0 is a point on the boundary, the singular integration at the right hand side of Eq. (2.13) takes Cauchy Principal Value. If ζ_0 is a corner point, the coefficient at the left hand side is $\Theta_{\text{corner}}/\pi$ instead of 1, where Θ_{corner} is the angle formed by the two sides at the corner.

Since $f_\alpha(z_\alpha)$ is an analytic function, $f'_\alpha(z_\alpha)$ is also analytic. f_α in Eq. (2.8) can be replaced by f'_α. Using $df_\alpha = f'_\alpha(\zeta_\alpha)d\zeta_\alpha = \dfrac{df_\alpha}{ds}ds$, we obtain the integral equations about the derivatives of displacements $d\mathbf{u}/ds$ and tractions $\mathbf{t}$,

$$\frac{1}{\pi i}\oint_{\partial\Omega}\left\langle 1/(\varsigma_\alpha-\varsigma_\alpha^0)\right\rangle\cdot\mathbf{L}^{-1}\cdot(\mathbf{B}+\overline{\mathbf{B}})^{-1}\cdot[i\frac{d\mathbf{u}}{ds}-\overline{\mathbf{B}}\cdot\mathbf{t}]\bigg|_{\zeta}ds=\left\langle 1/(C_0+p_\alpha S_0)\right\rangle\cdot\mathbf{L}^{-1}\cdot(\mathbf{B}+\overline{\mathbf{B}})^{-1}\cdot[i\frac{d\mathbf{u}}{ds}-\overline{\mathbf{B}}\cdot\mathbf{t}]\bigg|_{\zeta_0} \tag{2.14}$$

where ς_0 is a point on the boundary $\partial\Omega$, $C_0 = \cos(\theta_0)$, $S_0 = \sin(\theta_0)$, and θ_0 is the tangent angle at point ς_0 on $\partial\Omega$ (Fig. 2.1). Both sides of the equation can be multiplied by matrices **A** or **L** so that even in the degenerate cases, in which **A** and **L** are singular, the limit of $\mathbf{A}\cdot\langle *\rangle\cdot\mathbf{L}^{-1}$ or $\mathbf{L}\cdot\langle *\rangle\cdot\mathbf{L}^{-1}$ still exists and the equations still hold even for the case of isotropic materials. Here, $\langle *\rangle$ represents any diagonal matrix listed above.

Furthermore, $d\mathbf{u}/ds$ and $\mathbf{t}$ on the boundary can be explicitly expressed by boundary integrals. First eliminate the matrices at the right hand side of Eq. (2.14), then take the real part,

$$\mathbf{t}\big|_{\zeta_0}=-2\,\mathrm{Re}\{\frac{1}{\pi i}\oint_{\partial\Omega}\mathbf{L}\cdot\left\langle(C_0+p_\alpha S_0)/(\varsigma_\alpha-\varsigma_\alpha^0)\right\rangle\cdot\mathbf{L}^{-1}\cdot(\mathbf{B}+\overline{\mathbf{B}})^{-1}\cdot[i\frac{d\mathbf{u}}{ds}-\overline{\mathbf{B}}\cdot\mathbf{t}]\bigg|_{\varsigma}ds\} \tag{2.15}$$

If we take the imaginary part of Eq. (2.14), we have

$$\frac{d\mathbf{u}}{ds}\bigg|_{\zeta_0}=\mathrm{Im}\{\frac{1}{\pi i}\oint_{\partial\Omega}(\mathbf{B}+\overline{\mathbf{B}})\cdot\mathbf{L}\cdot\left\langle(C_0+p_\alpha S_0)/(\varsigma_\alpha-\varsigma_\alpha^0)\right\rangle\cdot\mathbf{L}^{-1}\cdot(\mathbf{B}+\overline{\mathbf{B}})^{-1}\cdot[i\frac{d\mathbf{u}}{ds}-\overline{\mathbf{B}}\cdot\mathbf{t}]\bigg|_{\varsigma}ds\}-\mathrm{Im}(\mathbf{B})\cdot\mathbf{t}\big|_{\varsigma_0} \tag{2.16}$$

Insert Eq. (2.15) into the last term of Eq. (2.16), then use $(\mathbf{B}+\overline{\mathbf{B}})=2\,\mathrm{Re}(\mathbf{B})$ and $\mathbf{BL}=i\mathbf{A}$, we have,

$$\left.\frac{d\mathbf{u}}{ds}\right|_{\zeta_0} = 2\,\mathrm{Re}\{\frac{1}{\pi i}\oint_{\partial\Omega}\mathbf{A}\cdot\left\langle (C_0 + p_\alpha S_0)/(\varsigma_\alpha - \varsigma_\alpha^0)\right\rangle\cdot\mathbf{L}^{-1}\cdot(\mathbf{B}+\overline{\mathbf{B}})^{-1}\cdot\left.[i\frac{d\mathbf{u}}{ds} - \overline{\mathbf{B}}\cdot\mathbf{t}]\right|_{\varsigma} ds\} \qquad (2.17)$$

Because of the weak singularity of the integral kernels of Eq. (2.11), the displacements at a boundary point ς_0 can be obtained from Eq. (2.11) by simply replacing z by ς_0,

$$\left.\mathbf{u}\right|_{\varsigma_0} = -\frac{1}{\pi}\mathrm{Re}\oint_{\partial\Omega}\mathbf{A}\cdot\left\langle \ln(\varsigma_\alpha - \varsigma_\alpha^0)\right\rangle\cdot\mathbf{L}^{-1}\cdot(\mathbf{B}+\overline{\mathbf{B}})^{-1}\cdot\left.(\frac{d\mathbf{u}}{ds} + i\overline{\mathbf{B}}\cdot\mathbf{t})\right|_{\zeta} ds + \left.\mathbf{u}\right|_{\varsigma^{(r)}} \qquad (2.18a)$$

.Let $\varsigma^{(r)} = \varsigma_0$, we have

$$\oint_{\partial\Omega}\mathbf{A}\cdot\left\langle \ln(\varsigma_\alpha - \varsigma_\alpha^0)\right\rangle\cdot\mathbf{L}^{-1}\cdot(\mathbf{B}+\overline{\mathbf{B}})^{-1}\cdot\left.(\frac{d\mathbf{u}}{ds} + i\overline{\mathbf{B}}\cdot\mathbf{t})\right|_{\zeta} ds = 0 \qquad (2.18b)$$

The branch cut of the logarithm function is a line from point ς_0 going outward and not intersecting the boundary at other places (Fig. A.1(c)). Even though **A** and **L** are singular for degenerate cases, the limit of $\mathbf{A}\cdot\left\langle \ln(\varsigma_\alpha - \varsigma_\alpha^0)\right\rangle\cdot\mathbf{L}^{-1}$ exists, so Eq. (2.18) holds for any material. Indeed, if we take the limit of Eq. (2.18b) for isotropic materials, then pick the real part, we obtain the integral equations used in [65] for constructing a boundary element scheme. Complex variable boundary integral equations in terms of the displacement **u** and the traction **t** are derived in Appendix A.

2.4. Boundary Integral Equations for Isotropic Materials

In this section and the sections that follow, the calculations are carried out only for Eqs. (2.14) and (2.18b). However, the kernels in Eqs. (2.15) and (2.17) are similar to the kernel in Eq. (2.14). Therefore, isotropic formulation and numerical schemes for Eqs (2.15) and (2.17) can be deduced easily from their counterparts for Eq. (2.14).

Consider a two dimensional bonded isotropic domain subjected to a plane stress state. The anti-plane and in-plane deformations decouple. Thus, the Eigen values of the Stroh formulations reduce to two. For a moving source at a constant speed v inside the isotropic domain, the matrices **A**, **L** and **B** are

$$\mathbf{A} = \begin{bmatrix} 1 & -p_2 \\ p_1 & 1 \end{bmatrix} \tag{2.19a}$$

$$\mathbf{L} = \mu \begin{bmatrix} 2p_1 & 1-p_2^2 \\ -(1-p_2^2) & 2p_2 \end{bmatrix} \tag{2.19b}$$

$$\mathbf{B} = \frac{i}{\mu[4p_1p_2 + (1-p_2^2)^2]} \begin{bmatrix} p_2(1+p_2^2) & -(2p_1p_2 + (1-p_2^2)) \\ 2p_1p_2 + (1-p_2^2) & p_1(1+p_2^2) \end{bmatrix} \tag{2.19c}$$

where $p_1 = i\sqrt{1 - \frac{v^2}{c_1^2}}$ and $p_2 = i\sqrt{1 - \frac{v^2}{c_s^2}}$; v is the source speed, c_1 and c_s are the longitudinal and shear wave speeds respectively given by $c_1 = \left[\frac{2(1-\nu)\mu}{(1-2\nu)\rho}\right]^{1/2}$ and $c_s = \left[\frac{\mu}{\rho}\right]^{1/2}$; μ is the shear modulus, ν is Poisson's ratio and ρ is the mass density.

For the sake of abbreviation, denote the diagonal matrices $\left\langle 1/(\varsigma_\alpha - \varsigma_\alpha^0)\right\rangle$, $\left\langle \ln(\varsigma_\alpha - \varsigma_\alpha^0)\right\rangle$, $\left\langle p_\alpha/(\varsigma_\alpha - \varsigma_\alpha^0)\right\rangle$ and $\left\langle 1/(C_0 + p_\alpha S_0\right\rangle$ as $\mathbf{D}(\zeta_\alpha, \zeta_\alpha^0)$, $\mathbf{D}_{\mathbf{ln}}(\zeta_\alpha, \zeta_\alpha^0)$, $\mathbf{D}_{\mathbf{p}}(\zeta_\alpha, \zeta_\alpha^0)$ and $\mathbf{D}_{\boldsymbol{\theta}}(\zeta_\alpha^0)$, respectively and denote **I** as the identity matrix. For the static case where the speed v is zero, *p₁* and *p₂* are equal to the imaginary unit i, which makes the matrices **A** and **L** singular. However, the kernels $\mathbf{L}.\mathbf{D}(\zeta_\alpha, \zeta_\alpha^0).\mathbf{L}^{-1}$, $\mathbf{A}.\mathbf{D}_{\mathbf{ln}}(\zeta_\alpha, \zeta_\alpha^0).\mathbf{L}^{-1}$, $\mathbf{L}.\mathbf{D}_{\mathbf{p}}(\zeta_\alpha, \zeta_\alpha^0).\mathbf{L}^{-1}$ and $\mathbf{L}.\mathbf{D}_{\boldsymbol{\theta}}(\zeta_\alpha^0).\mathbf{L}^{-1}$, $\alpha = 1,2$, and the matrix **B** still hold in the limiting case when the speed v approaches zero.

The limits of the above kernels were determined as follows. First, we expanded the matrices $\mathbf{D}(\zeta_\alpha, \zeta_\alpha^0)$, $\mathbf{D}_{\mathbf{ln}}(\zeta_\alpha, \zeta_\alpha^0)$, $\mathbf{D}_{\mathbf{p}}(\zeta_\alpha, \zeta_\alpha^0)$ and $\mathbf{D}_{\boldsymbol{\theta}}(\zeta_\alpha^0)$ about $p_\alpha = \mathrm{i}$ using Taylor series to the first order. Second, we calculated the limits as v approaches 0. It is necessary to note that the first order Taylor expansion is enough since the limits of the matrices products $A\langle (p_\alpha - i)^n \rangle L^{-1}$ and $L\langle (p_\alpha - i)^n \rangle L^{-1}$ are zero for $n \geq 2$. The matrices obtained for the isotropic domain are

$$\mathbf{B} = \frac{1}{\mu}\begin{bmatrix} 1-\upsilon & \frac{i(1-2\upsilon)}{2} \\ \frac{-i(1-2\upsilon)}{2} & 1-\upsilon \end{bmatrix} \tag{2.20a}$$

$$\mathbf{L.D}(\zeta_\alpha, \zeta_{\alpha,0}) \cdot \mathbf{L}^{-1} = \frac{1}{\zeta - \zeta_0}.\mathbf{I} - \frac{y - y_0}{\zeta - \zeta_0}.\begin{bmatrix} i & -1 \\ -1 & -i \end{bmatrix} \tag{2.20b}$$

$$\mathbf{A}.\mathbf{D}_{\ln}(\zeta_\alpha, \zeta_{\alpha,0}).\mathbf{L}^{-1} = \log(\zeta - \zeta_0).\mathbf{I} + \frac{y - y_0}{\zeta - \zeta_0}.\frac{1}{2\mu}\begin{bmatrix} 1 & i \\ i & -1 \end{bmatrix} \tag{2.20c}$$

$$\mathbf{L}.\mathbf{D}_p(\zeta_\alpha, \zeta_\alpha^0) \cdot \mathbf{L}^{-1} = \frac{1}{\zeta - \zeta_0}.\mathbf{I} - \frac{y - y_0}{\zeta - \zeta_0}.\begin{bmatrix} -1 & -i \\ -i & 1 \end{bmatrix} + \begin{bmatrix} 2i & -1 \\ -1 & 0 \end{bmatrix} \tag{2.20d}$$

$$\mathbf{L}.\mathbf{D}_\theta(\zeta_\alpha^0) \cdot \mathbf{L}.^{-1} = (1 + \exp(-i\theta_0)).\mathbf{I} - S_0 \exp(-i\theta_0)\begin{bmatrix} i & -1 \\ -1 & -i \end{bmatrix} \tag{2.20e}$$

$$(\mathbf{B} + \overline{\mathbf{B}})^{-1} = \frac{\mu}{(1-\upsilon)}.\begin{bmatrix} 1 & 0 \\ 0 & 1 \end{bmatrix} \tag{2.20f}$$

where θ_0 is the tangential angle at ζ^0, $\zeta = x + iy$, $\zeta^0 = x_0 + iy_0$ and S_0 is the trigonometric sine function of the angle θ_0 (see Fig. 2.1).

Hence, for isotropic materials, the boundary integral equations (Eqs. 2.14 and 2.18b) and the stress field at internal points Z = X+iY (Eqs. 2.12a and 2.12b) have the following forms,

$$\begin{aligned} &\frac{1}{\pi i}\oint_{\partial\Omega}\left\{\frac{1}{\zeta - \zeta^0}.\mathbf{I} - \frac{y - y_0}{\zeta - \zeta^0}.\begin{bmatrix} i & -1 \\ -1 & -i \end{bmatrix}\right\}\cdot[i\frac{d\mathbf{u}}{ds} - \overline{\mathbf{B}}.\mathbf{t}]\Big|_{\zeta} ds \\ &\quad = \left\{(1 + e^{-i\theta_0})\mathbf{I} - S_0 e^{-i\theta_0}\begin{bmatrix} i & -1 \\ -1 & -i \end{bmatrix}\right\}\cdot[i\frac{d\mathbf{u}}{ds} - \overline{\mathbf{B}} \cdot \mathbf{t}]\Big|_{\zeta_0} \end{aligned} \tag{2.21a}$$

$$\oint_{\partial\Omega}\left\{\ln(\zeta-\zeta_0).\mathbf{I}+\frac{y-y_0}{\zeta-\zeta_0}.\frac{1}{2\mu}\begin{bmatrix}1 & i\\ i & -1\end{bmatrix}\right\}\cdot[i\frac{d\mathbf{u}}{ds}-\overline{\mathbf{B}}\cdot\mathbf{t}]\Big|_{\zeta}\,ds=0 \tag{2.21b}$$

$$[\sigma_{21},\sigma_{22}]^T\Big|_Z=\frac{\mu}{2\pi(1-\upsilon)}\mathrm{Re}\oint_{\partial\Omega}\left\{\frac{1}{\zeta^0-Z}.\mathbf{I}-\frac{y_0-Y}{\zeta^0-Z}.\begin{bmatrix}i & -1\\ -1 & -i\end{bmatrix}\right\}.[i\frac{d\mathbf{u}}{ds}-\overline{\mathbf{B}}\cdot\mathbf{t}]\Big|_{\zeta_0}\,ds \tag{2.22a}$$

$$[\sigma_{11},\sigma_{12}]^T\Big|_Z=\frac{-\mu}{2\pi(1-\nu)}\mathrm{Re}\oint_{\partial\Omega}\left\{\frac{1}{\zeta^0-Z}\mathbf{I}-\frac{y_0-Y}{\zeta^0-Z}\begin{bmatrix}-1 & -i\\ -i & 1\end{bmatrix}+\begin{bmatrix}2i & -1\\ -1 & 0\end{bmatrix}\right\}[i\frac{d\mathbf{u}}{ds}-\overline{\mathbf{B}}.\mathbf{t}]\Big|_{\zeta}\,ds \tag{2.22b}$$

2.5. Numerical Implementation

In this section, numerical schemes for the anisotropic integral equations are developed first, and then the isotropic forms of these numerical schemes are deduced. Consider a two dimensional isotropic domain with a simple closed boundary $\partial\Omega_\alpha$ of boundary length *L* in the z_α-plane. The boundary $\partial\Omega_\alpha$ is discretized into *N* linear boundary elements interconnected with a single node, where the last node and the first node are the same. Let $\partial\Omega_\alpha^{(k)}$ denotes the kth element, which connects the node *k* to the node *k+1*. For a well defined two-dimensional isotropic problem case, there are four boundary values at each node, two of which are known and the other two are to be determined. So, in total, there are *2N* unknowns. In order to solve for these unknowns, either Eq. (2.14) or (2.18b) can be used to construct a linear system of *2N* equations by collocating at the mid points $\zeta_{\alpha,0}^{(m)}$ of the *N* elements , *m = 1…. N* (Fig. 2.2).

The values of the vectors $\partial\mathbf{u}/\partial s$ and **t** at any point along the linear element can be interpolated from the nodal values by using the Lagrange shape functions *N₁(s)* and *N₂(s)*,

$$\partial\mathbf{u}/\partial s=N_1(s)(\partial\mathbf{u}/\partial s)_1+N_2(s)(\partial\mathbf{u}/\partial s)_2 \tag{2.23a}$$

$$\mathbf{t}=N_1(s)\mathbf{t}_1+N_2(s)\mathbf{t}_2 \tag{2.23b}$$

with $N_1(s)=1-\frac{s}{L_k}$ and $N_2(s)=\frac{s}{L_k}$

where L_k is the length of the k^th^ element and s is a parameter which varies from 0 to L_k.

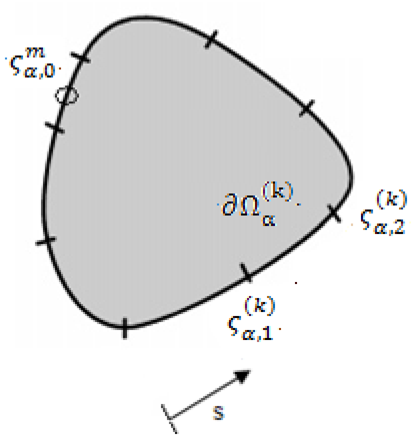

Figure 2.2. Discretized boundary of a simply connected domain in the z_α-plane.

The shape functions in the z_α plane can be written as,

$$N_1(\zeta_\alpha)=1-\frac{\zeta_\alpha-\zeta^k_{\alpha,1}}{\zeta^k_{\alpha,2}-\zeta^k_{\alpha,1}} \quad ; \quad N_2(\zeta_\alpha)=\frac{\zeta_\alpha-\zeta^k_{\alpha,1}}{\zeta^k_{\alpha,2}-\zeta^k_{\alpha,1}} \tag{2.24}$$

The integrals at the left hand sides of Eqs. (2.14) and (2.18b) are respectively rewritten in the z_α-plane as,

$$\sum_{k=1}^{N}\sum_{j=1}^{2}\frac{1}{\pi}\left\{\mathbf{L}.E_k^{(j)}.\mathbf{L}^{-1}.(\mathbf{B}+\overline{\mathbf{B}})^{-1}.[\frac{d\mathbf{u}^{(j)}}{ds}+i\overline{\mathbf{B}}.t^{(j)}\right\} \tag{2.25a}$$

$$\sum_{k=1}^{N}\sum_{j=1}^{2}\frac{1}{\pi}\left\{\mathbf{A}.F_k^{(j)}.\mathbf{L}^{-1}.(\mathbf{B}+\overline{\mathbf{B}})^{-1}.[\frac{d\mathbf{u}^{(j)}}{ds}+i\overline{\mathbf{B}}.\mathbf{t}^{(j)}]\right\} \tag{2.25b}$$

$$E_k^1=\int_{\zeta^{(k)}_{\alpha,1}}^{\zeta^{(k)}_{\alpha,2}}(1-\frac{\zeta_\alpha-\zeta^{(k)}_{\alpha,1}}{\zeta^{(k)}_{\alpha,2}-\zeta^{(k)}_{\alpha,1}}).\frac{1}{\zeta_\alpha-\zeta^{(m)}_{\alpha,0}}.\frac{d\zeta_\alpha}{C_k+p_\alpha S_k} \tag{2.25c}$$

$$E_k^2 = \int_{\zeta_{\alpha,1}^{(k)}}^{\zeta_{\alpha,2}^{(k)}} \frac{\zeta_\alpha - \zeta_{\alpha,1}^{(k)}}{\zeta_{\alpha,2}^{(k)} - \zeta_{\alpha,1}^{(k)}} \cdot \frac{1}{\zeta_\alpha - \zeta_{\alpha,0}^{(m)}} \cdot \frac{d\zeta_\alpha}{C_k + p_\alpha S_k} \tag{2.25d}$$

$$F_k^1 = \int_{\zeta_{\alpha,1}^{(k)}}^{\zeta_{\alpha,2}^{(k)}} (1 - \frac{\zeta_\alpha - \zeta_{\alpha,1}^{(k)}}{\zeta_{\alpha,2}^{(k)} - \zeta_{\alpha,1}^{(k)}}).\ln(\zeta_\alpha - \zeta_{\alpha,0}^{(m)}).\frac{d\zeta_\alpha}{C_k + p_\alpha S_k} \tag{2.25e}$$

$$F_k^2 = \int_{\zeta_{\alpha,1}^{(k)}}^{\zeta_{\alpha,2}^{(k)}} \frac{\zeta_\alpha - \zeta_{\alpha,1}^{(k)}}{\zeta_{\alpha,2}^{(k)} - \zeta_{\alpha,1}^{(k)}}.\ln(\zeta_\alpha - \zeta_{\alpha,0}^{(m)}).\frac{d\zeta_\alpha}{C_k + p_\alpha S_k} \tag{2.25f}$$

The above integrals are regular and can be evaluated analytically along all the elements except along the element to which $\zeta_{\alpha,0}^{(m)}$ belongs. The explicit solutions for the above integrals in this case are

$$E_k^1 = \frac{1}{C_k + p_\alpha S_k}[-1 + (1 + \frac{\zeta_{\alpha,1}^{(k)} - \zeta_{\alpha,0}^{(m)}}{\zeta_{\alpha,2}^{(k)} - \zeta_{\alpha,1}^{(k)}}).\log(1 + \frac{\zeta_{\alpha,2}^{(k)} - \zeta_{\alpha,1}^{(k)}}{\zeta_{\alpha,1}^{(k)} - \zeta_{\alpha,0}^{(m)}})] \tag{2.26a}$$

$$E_k^2 = \frac{1}{C_k + p_\alpha S_k}[1 - \frac{\zeta_{\alpha,1}^{(k)} - \zeta_{\alpha,0}^{(m)}}{\zeta_{\alpha,2}^{(k)} - \zeta_{\alpha,1}^{(k)}}.\log(1 + \frac{\zeta_{\alpha,2}^{(k)} - \zeta_{\alpha,1}^{(k)}}{\zeta_{\alpha,1}^{(k)} - \zeta_{\alpha,0}^{(m)}})] \tag{2.26b}$$

$$F_k^1 = \frac{1}{(C_k + p_\alpha S_k)(\zeta_{\alpha,2}^{(k)} - \zeta_{\alpha,1}^{(k)})}[g_1(\zeta_{\alpha,2}^{(k)}) - g_2(\zeta_{\alpha,1}^{(k)})] \tag{2.26c}$$

$$F_k^2 = \frac{1}{(C_k + p_\alpha S_k)(\zeta_{\alpha,2}^{(k)} - \zeta_{\alpha,1}^{(k)})}[g_2(\zeta_{\alpha,2}^{(k)}) - g_2(\zeta_{\alpha,1}^{(k)})] \tag{2.26d}$$

where,

$$g_2(\zeta_\alpha) = (\zeta_\alpha - \zeta_{\alpha,0}^{(m)})\ln(\zeta_\alpha - \zeta_{\alpha,0}^{(m)}).[\frac{1}{2}(\zeta_\alpha - \zeta_{\alpha,0}^{(m)}) - (\zeta_{\alpha,1} - \zeta_{\alpha,0}^{(m)})$$

$$+ (\zeta_\alpha - \zeta_{\alpha,0}^{(m)})[-\frac{1}{4}(\zeta_\alpha - \zeta_{\alpha,0}^{(m)}) + (\zeta_{\alpha,1} - \zeta_{\alpha,0}^{(m)})]$$

$$g_1(\zeta_\alpha) = -g_2(\zeta_\alpha) + (\zeta_\alpha - \zeta_{\alpha,0}^{(m)})[\ln(\zeta_\alpha - \zeta_{\alpha,0}^{(m)}) - 1]$$

Let us now consider the case where $\zeta_{\alpha,0}^{(m)}$ is in the middle of the kth element; that is when *m* and *k* are equal. F_k^1 and F_k^2 are weakly singular so the two integrals can still be evaluated analytically and Eqs. (2.26c) and (2.26d) are still valid. However, E_k^1 and E_k^2 are not regular and can be decomposed into a regular integral and another integral which is singular in the Cauchy principal value sense (CPV).

$$E_k^1 = \frac{1}{(\zeta_{\alpha,2}^{(k)} - \zeta_{\alpha,1}^{(k)})(C_k + p_\alpha S_k)} \left\{ (\zeta_{\alpha,2}^{(k)} - \zeta_{\alpha,0}^{(m)}) \int_{\zeta_{\alpha,1}^{(k)}}^{\zeta_{\alpha,2}^{(k)}} \frac{d\zeta_\alpha}{\zeta_\alpha - \zeta_{\alpha,0}^{(m)}} - \int_{\zeta_{\alpha,1}^{(k)}}^{\zeta_{\alpha,2}^{(k)}} d\zeta_\alpha \right\} \tag{2.27a}$$

$$E_k^2 = \frac{1}{(\zeta_{\alpha,2}^{(k)} - \zeta_{\alpha,1}^{(k)})(C_k + p_\alpha S_k)} \left\{ (\zeta_{\alpha,0}^{(m)} - \zeta_{\alpha,1}^{(k)}) \int_{\zeta_{\alpha,1}^{(k)}}^{\zeta_{\alpha,2}^{(k)}} \frac{d\zeta_\alpha}{\zeta_\alpha - \zeta_{\alpha,0}^{(m)}} + \int_{\zeta_{\alpha,1}^{(k)}}^{\zeta_{\alpha,2}^{(k)}} d\zeta_\alpha \right\} \tag{2.27b}$$

The CPV singular integral is evaluated by taking a half circle around the singular point $\zeta_{\alpha,0}^{(m)}$. It can be easily shown that the singular term vanishes. The expressions obtained for E_k^1 and E_k^2 in this case are

$$E_k^1 = \frac{-1}{C_k + p_\alpha S_k} \quad ; \quad E_k^2 = \frac{1}{C_k + p_\alpha S_k} \tag{2.28}$$

Following the same approach in Section 2.3, Eqs (2.27a), (2.27b), (2.27c) and (2.27d) are determined for the isotropic case as follows,

$$E_K^1 = H_c^1(\zeta_2^{(k)}, \zeta_1^{(k)}, \zeta_0^{(m)}) + (p_\alpha - i).H_v^1(\zeta_2^{(k)}, \zeta_1^{(k)}, \zeta_0^{(m)}) \tag{2.29a}$$

$$E_K^2 = H_c^2(\zeta_2^{(k)}, \zeta_1^{(k)}, \zeta_0^{(m)}) + (p_\alpha - i).H_v^2(\zeta_2^{(k)}, \zeta_1^{(k)}, \zeta_0^{(m)}) \tag{2.29b}$$

$$F_K^1 = G_c^1(\zeta_2^{(k)}, \zeta_1^{(k)}, \zeta_0^{(m)}) + (p_\alpha - i).G_v^1(\zeta_2^{(k)}, \zeta_1^{(k)}, \zeta_0^{(m)}) \tag{2.29c}$$

$$F_K^2 = G_c^2(\zeta_2^{(k)}, \zeta_1^{(k)}, \zeta_0^{(m)}) + (p_\alpha - i).G_v^2(\zeta_2^{(k)}, \zeta_1^{(k)}, \zeta_0^{(m)}) \tag{2.29d}$$

$$D_\theta(\zeta_\alpha^0) = M_c(\zeta_2^{(k)}, \zeta_1^{(k)}, \zeta_0^{(m)}) + (p_\alpha - i).M_v(\zeta_2^{(k)}, \zeta_1^{(k)}, \zeta_0^{(m)}) \tag{2.29e}$$

where $H_c^{(j)}, H_v^{(j)}, G_c^{(j)}, G_v^{(j)}, M_{\mathrm{c}}$ and $M_{\mathrm{v}}, (j=1,2)$, are functions in the z-plane and given in Appendix B.

Numerical schemes for Eqs. (2.14) and (2.18b) are written for isotropic materials as,

$$\begin{aligned}&\sum_{k=1}^{N}\sum_{j=1}^{2}\frac{1}{\pi i}\left[H_c^{(j)}(\varsigma_2^{(k)},\varsigma_1^{(k)},\varsigma_0^{(k)})\mathbf{I}+H_v^{(j)}(\varsigma_2^{(k)},\varsigma_1^{(k)},\varsigma_0^{(k)})\begin{bmatrix} i & -1\\ -1 & -i\end{bmatrix}\right]\cdot[i\frac{d\mathbf{u}^{(j)}}{ds}-\overline{\mathbf{B}}\cdot\mathbf{t}^{(j)}]\\ &\qquad=\left\{(1+e^{-i\theta_0})\mathbf{I}-S_0e^{-i\theta_0}\begin{bmatrix} i & -1\\ -1 & -i\end{bmatrix}\right\}\cdot[i\frac{d\mathbf{u}}{ds}-\overline{B}\cdot\mathbf{t}]\bigg|_{\zeta_0}\end{aligned} \tag{2.30a}$$

$$\sum_{k=1}^{N}\sum_{j=1}^{2}\left[-iG_c^{(j)}(\varsigma_2^{(k)},\varsigma_1^{(k)},\varsigma_0^{(k)})\mathbf{B}+G_v^{(j)}(\varsigma_2^{(k)},\varsigma_1^{(k)},\varsigma_0^{(k)})\begin{bmatrix} 1 & -i\\ i & 1\end{bmatrix}\right]\cdot[i\frac{d\mathbf{u}^{(j)}}{ds}-\overline{\mathbf{B}}\cdot\mathbf{t}^{(j)}]=0 \tag{2.30b}$$

Noting the similarity between Eqs.(2.12a) and (2.12b) and the left hand side of the Eq.(2.14), the stress fields for the isotropic domain are written as,

$$[\sigma_{21,}\sigma_{22}]^T=\frac{\mu}{2\pi(1-\nu)}\mathrm{Re}\{\sum_{k=1}^{N}\sum_{j=1}^{2}\left\{\begin{matrix}H_c^{(j)}(\varsigma_2^{(k)},\varsigma_1^{(k)},\varsigma_0^{(k)}).\mathbf{I}+\\ H_v^{(j)}(\varsigma_2^{(k)},\varsigma_1^{(k)},\varsigma_0^{(k)})\begin{bmatrix} i & -1\\ -1 & -i\end{bmatrix}\end{matrix}\right\}\cdot[\frac{d\mathbf{u}^{(j)}}{ds}+i\overline{\mathbf{B}}\cdot\mathbf{t}^{(j)}]\} \tag{2.31a}$$

$$[\sigma_{11,}\sigma_{12}]^T=\frac{-\mu}{2\pi(1-\nu)}\mathrm{Re}\{\sum_{k=1}^{N}\sum_{j=1}^{2}\left\{\begin{matrix}N_c^{(j)}(\varsigma_2^{(k)},\varsigma_1^{(k)},\varsigma_0^{(k)})\mathbf{I}+\\ N_v^{(j)}(\varsigma_2^{(k)},\varsigma_1^{(k)},\varsigma_0^{(k)})\begin{bmatrix} i & -1\\ -1 & -i\end{bmatrix}\end{matrix}\right\}\cdot[\frac{d\mathbf{u}^{(j)}}{ds}+i\overline{\mathbf{B}}\cdot\mathbf{t}^{(j)}]\} \tag{2.31b}$$

where $N_c^{(j)}$ & $N_v^{(j)}$ (j =1,2) are given in the Appendix B.

Eqs. (2.30a) and (2.30b) are in complex forms. Thus, by taking the real or the imaginary part of Eqs. (2.30a) or (2.30b), we can form a linear system of *2N* equations which can be solved using numerical techniques such as Gaussian elimination to compute the unknown boundary values. It is worth noting that the expressions E_k^1 , E_k^2 , F_k^1 and F_k^2 are bounded functions. Thus, the elements of the coefficient matrix obtained for any of the two boundary integral equations are all small numbers. Moreover, the kernels in the integral expressions of the stress field are first order singular and after integrating over each element, a weak singular expression is obtained which eliminates the boundary layer affect.

2.6. Numerical Examples

The numerical schemes developed in the previous section for isotropic materials are used to solve various elastostatic boundary value problems with different boundary value types. A comparison between the convergence rates of the results obtained using the numerical schemes developed for Eqs. (2.14) and (2.18b) and the analytical results is provided. The fact that these boundary integral equations are functions of traction and tangential derivative of displacement eliminates the problem of rigid body motion for pure traction problems. In the case where the displacements are known at the boundary, the tangential derivative of the displacements can be calculated by differentiating the displacement along each element. This approach may introduce rigid body motion. Thus, special treatment is required to eliminate this rigid body motion. The authors eliminated this effect by forcing the equilibrium of moments about any point *O* at the boundary of the domain. The equilibrium of moment equation in the z-plane is

$$M_O = \sum_{k=1}^{N} \left\{ \begin{array}{l} \dfrac{L^{(k)}}{3}[-(y_1^{(k)} - y_O) - \dfrac{1}{2}(y_2^k - y_O)]t_{1x}^{(k)} + \dfrac{L^{(k)}}{3}[(x_1^{(k)} - x_O) + \dfrac{1}{2}(x_2^k - x_O)]t_{1y}^{(k)} \\ + \dfrac{L^{(k)}}{3}[-\dfrac{1}{2}(y_1^{(k)} - y_O) - (y_2^k - y_O)]t_{2x}^{(k)} + \dfrac{L^{(k)}}{3}[\dfrac{1}{2}(x_1^{(k)} - x_O) + (x_2^k - x_O)]t_{2y}^{(k)} \end{array} \right\} \tag{2.32}$$

where $(x_1^{(k)}, y_1^{(k)})$ $(x_2^{(k)}, y_2^{(k)})$ are the coordinates of the first and end nodes of the k$^{\text{th}}$ element, x_0 and y_0 are the components of the point *O* and $t_{1x}^{(k)}, t_{1y}^{(k)}, t_{2x}^{(k)}, t_{2y}^{(k)}$ are the *x* and *y* components of the traction vector at the first and end node of the k^{th} element. Eq. (2.32) can be added to the system of linear equations or replace one of the *2N* equations. In the former case, the linear system of equations becomes over determined. Thus, The Gaussian elimination cannot be used to solve the linear system. The least squares method provided satisfactory results. However, the Householder method can be used for better results. In the latter case, to the author's knowledge, there is no effective technique to decide which equation can be dropped without affecting the results.

The problems modeled in this chapter involve geometries with sharp corners. At these corners, components of the traction and the displacement gradient are not continuous which introduces two more unknowns at each node. The linear system becomes under-determined. For the problem solved in this chapter, the corner problem is treated by shifting the corner node a very small distance inside each of the two elements connected at this node. An element of length ε is placed between these two nodes as shown in Fig. 2.3. Therefore, two more equations are obtained at each corner. This approach is called small corner element.

Five elastic problems are modeled in order to check the accuracy of the new boundary integral equations and its effectiveness. The stress field is calculated at internal points very close to the boundary in order to show the effectiveness of the new formulation in eliminating the boundary layer effect. In all of the following problems, Poisson's ratio is taken as ν = 0.3 and the stress is normalized by the shear stress.

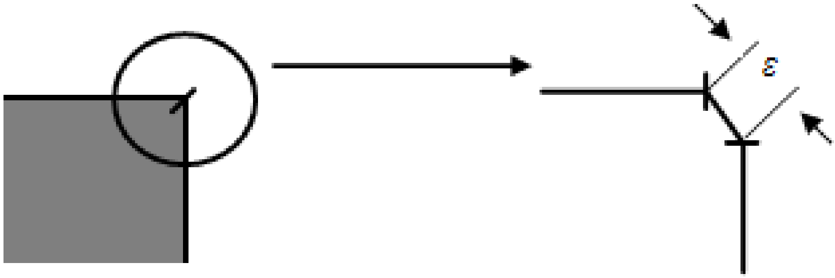

Figure 2.3. Treatment of a corner node using the small corner element approach**.**

2.6.1. Pure Traction

Consider a 1 x 1 plate subjected to a tension load of magnitude 1 in the *x* direction from both sides. The Mechanics of Material results of the stress field are $\sigma_x = 1.0$ and $\sigma_y = \sigma_{xy} = 0$. This problem is a pure tension problem. The boundary conditions are shown in Fig. 2.4 for a sample mesh size. Using the numerical schemes developed for Eqs. (2.14) and (2.18b), stresses are calculated at grid points uniformly distributed throughout the domain. Convergence rate is checked by calculating the L_2 error norm defined as,

$$E_{L2} = \sqrt{\frac{\sum_{i=1}^{N}(\sigma_{(i)}^{e} - \sigma_{(i)}^{c})^2}{\sum_{i=1}^{N}(\sigma_{(i)}^{e})^2}} \tag{2.33}$$

where σ^e is the analytical stress, σ^c is the computed stress and N is the number of grid points.

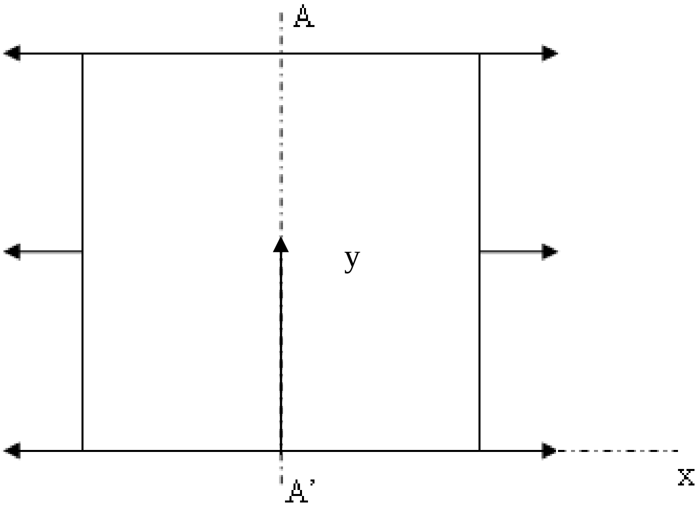

Figure 2.4. A plate under uni-axial tension**.**

Eq. (2.18b) required eight elements (2 elements along each side) for the solution to converge with an L_2 error norm of $4.3e^{-7}$. However, Eq. (2.14) required a very fine mesh around the corners and forty elements (10 along each side) in order to obtain results with an approximately L_2 error norm of $5e^{-4}$. The axial stress for the points along the vertical centerline of the plate (AA') in both mesh cases and the Mechanics of Material results are plotted in Fig. 2.5. The normalized relative errors of the two different meshes for both cases are shown in Fig. 2.6. Both equations show a great convergence of the stress fields at points close to or at the boundaries, which proves the advantage of these formulations in eliminating the boundary layer effect.

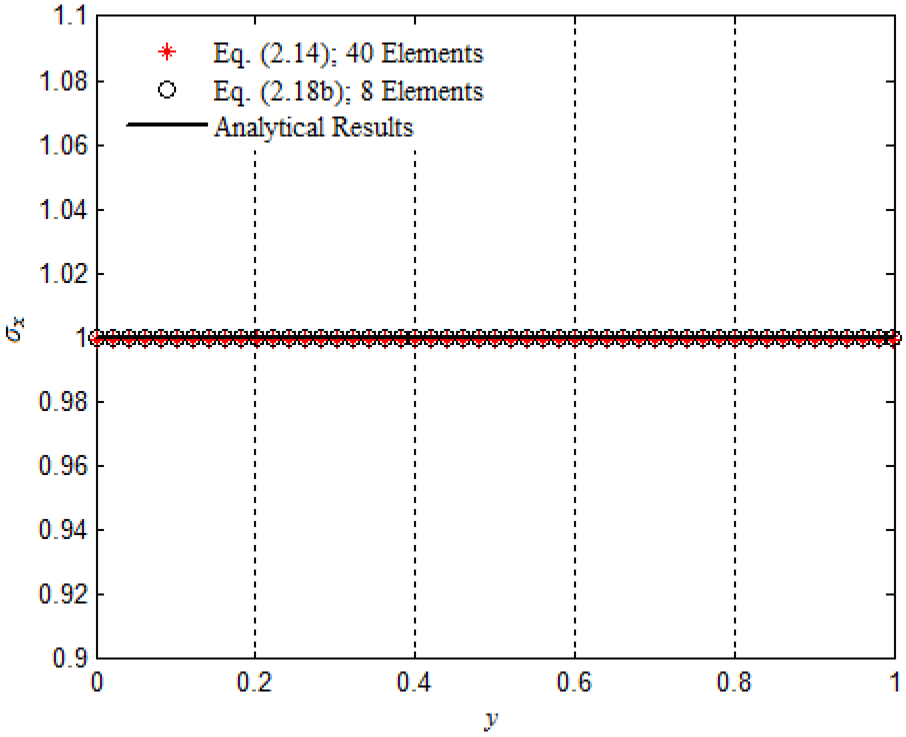

Figure 2.5. Axial normal stress, σ_x , along line AA'.

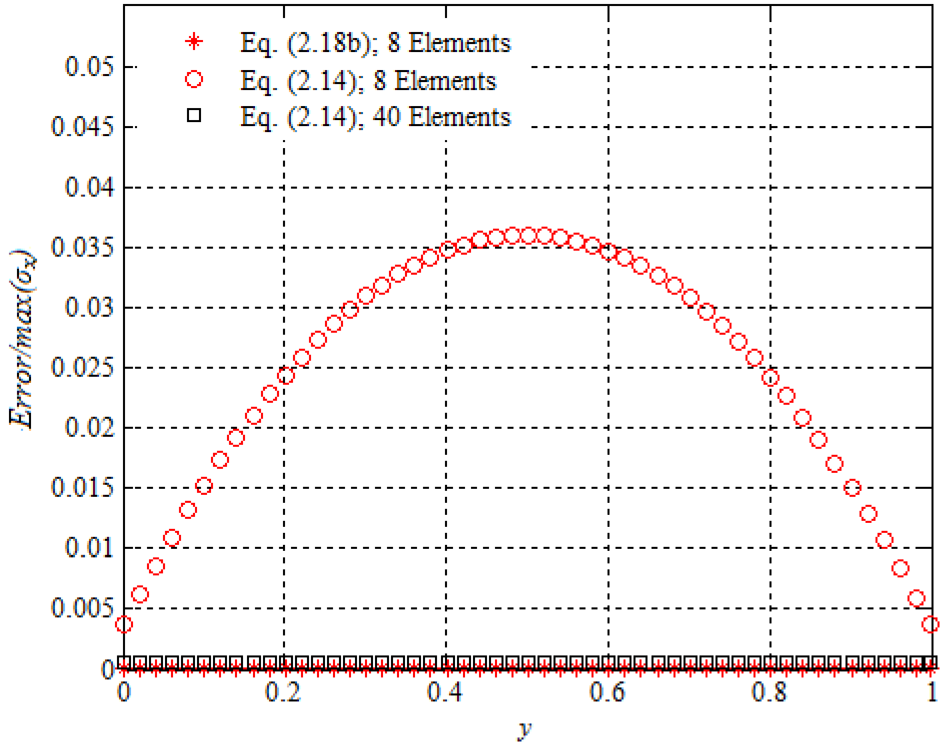

Figure 2.6. Normalized error of the computed axial stress, σ_x, along line AA'.

2.6.2. Pure Bending of a Beam

The same plate now is subjected to a bending load as shown in Fig. 2.7. This problem is also a pure traction problem. Let the normalized moment be 1/6. The analytical results are

$$\sigma_x = 2(y - 1/2), \tau_{xy} = \sigma_y = 0 \tag{2.34}$$

Stresses at grid points distributed uniformly on the plate are computed. The L_2 error norm is computed for the two types of meshes (eight elements and forty elements along the boundary) used in modeling the plate under pure traction. For the coarse mesh (8 elements), the L_2 error norm of the results obtained using Eqs. (2.14) and (2.18b) is respectively 0.165 and $4.37e^{-7}$.

Refining the mesh to 40 elements along the boundary of the plate reduced the L_2 error norm of the results obtained using Eq. (2.14) to 2.7e^{-5}.

For the axial stress, σ_x, along the centerline AA', Eq. (2.18b) provided accurate results with the eight nodes mesh. However, the error range obtained using Eq. (2.14) with eight nodes was between 0.175 at the boundary and 0.02 at the center of the plate. Eq. (2.14) required forty nodes to provide results at internal points close to the boundary with comparable errors to those obtained by using Eq. (2.18b). The converged results obtained using Eqs. (2.14) and (2.18b) are shown in Fig. 2.8. The normalized relative errors by the applied load are plotted in Fig. 2.9 for the two types of meshes (eight and forty nodes). This graph shows the fast convergence of Eq. (2.18b) and the effectiveness of the new formulations in eliminating the boundary layer effect.

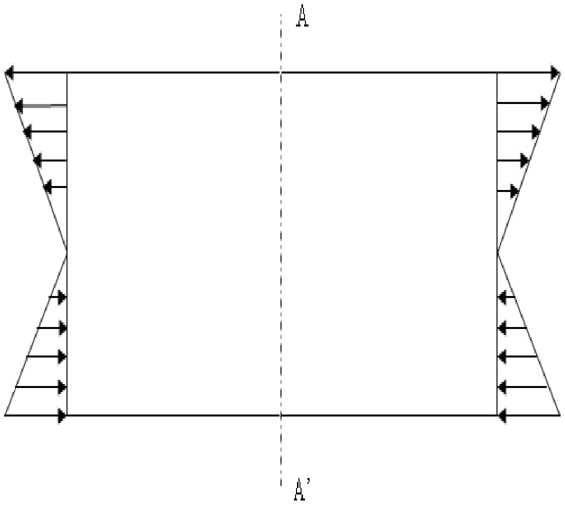

Figure 2.7. A Plate under pure bending.

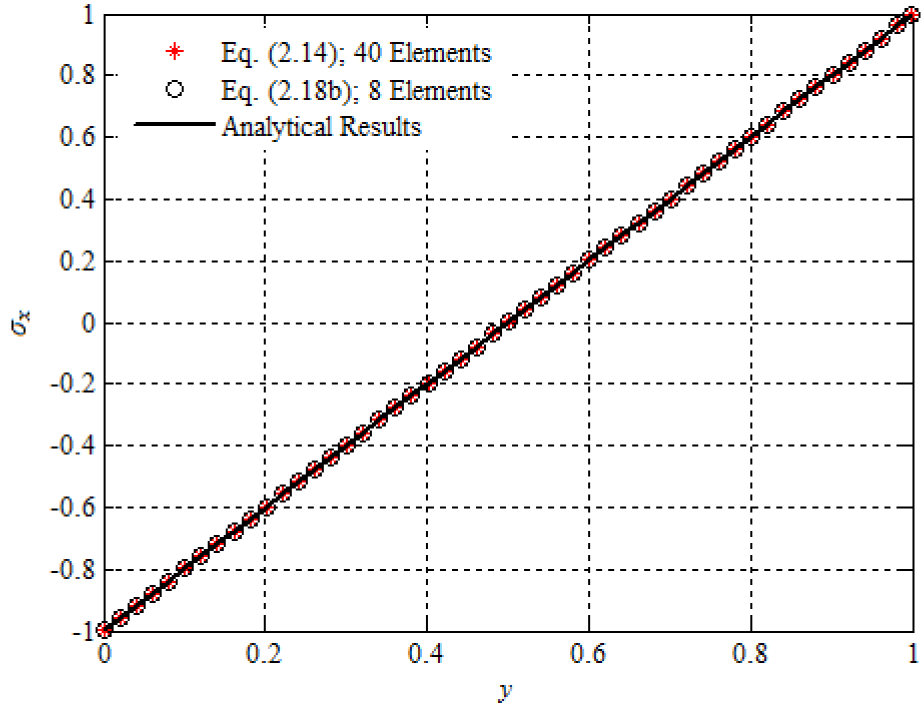

Figure 2.8. Axial stress σ_x along line *AA'*.

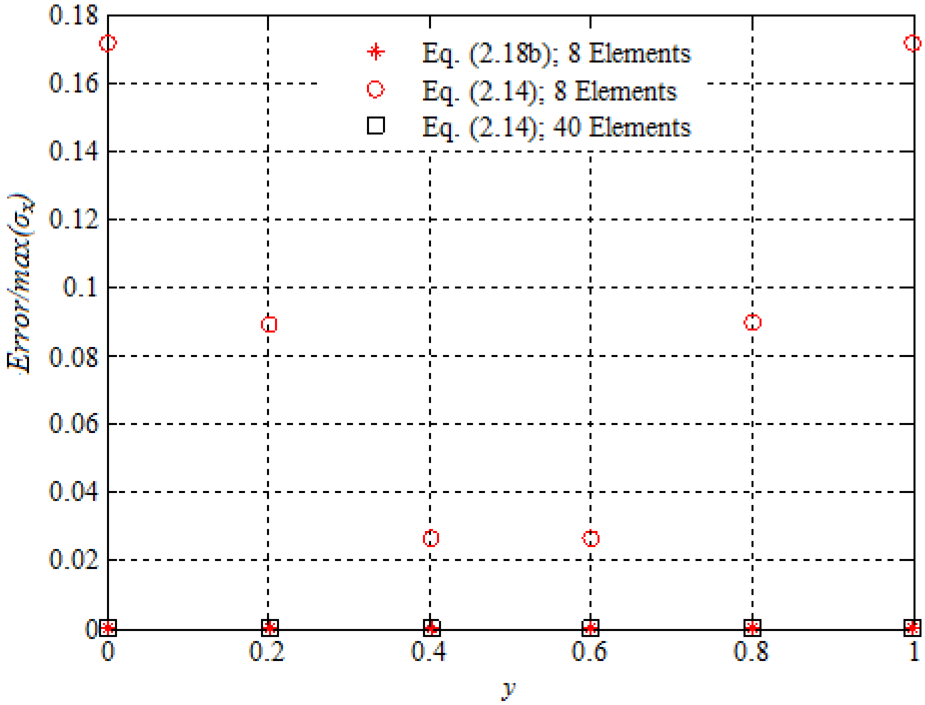

Figure 2.9. Normalized error of the computed axial stress, σ_x, along line *AA'*.

2.6.3. Bending of a Cantilever Beam

A beam of a rectangular cross section is loaded at its free end at the right and fixed at the left end (Fig. 2.10). The length and height of the beam are 10 and 1. The stress field near the two ends is very complicate and actually the analytical results are unknown. While according to the Saint-Venant’s principle, the stress along the center line AA’, which is away from the two ends, can be accurately predicted by the results from the elementary Mechanics of Materials,

$$\sigma_x = 60(y - 1/2) \text{ and } \tau_{xy} = 6(y^2 - y) \tag{2.35}$$

The fixed end of the beam is modeled by taking the local gradient of the displacements to be zero. This approach introduces a rigid body motion, which is treated by enforcing the equilibrium of moment using Eq. 2.32. The concentrated load is distributed along the right side of the edge. The boundary conditions are shown in Fig. 2.10.

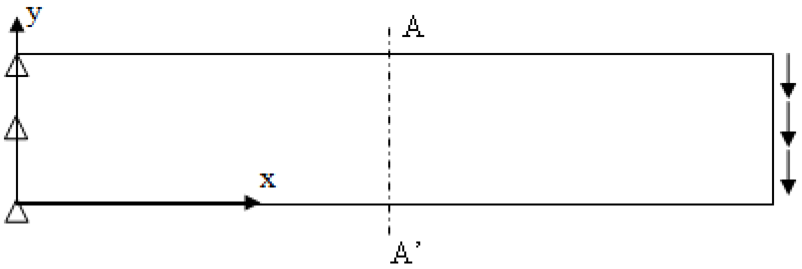

Figure 2.10. A cantilever beam under transversal loading.

The computed axial and shear stresses along the vertical centerline of the beam AA’ are shown in Figs. 2.11 and 2.12. This model required a bigger mesh size to converge than the previous two examples. This is due to the error that might be introduced by assuming the local gradient displacement to be zero along the left side of the beam. It is worth noting that the axial stress results converged faster than the shear stress results along the centerline of the beam. Again Eq. (2.18b) converged faster than Eq. (2.14). The normalized errors by the maximum axial stress of the stress field are shown in Figs. 2.13 and 2.14.

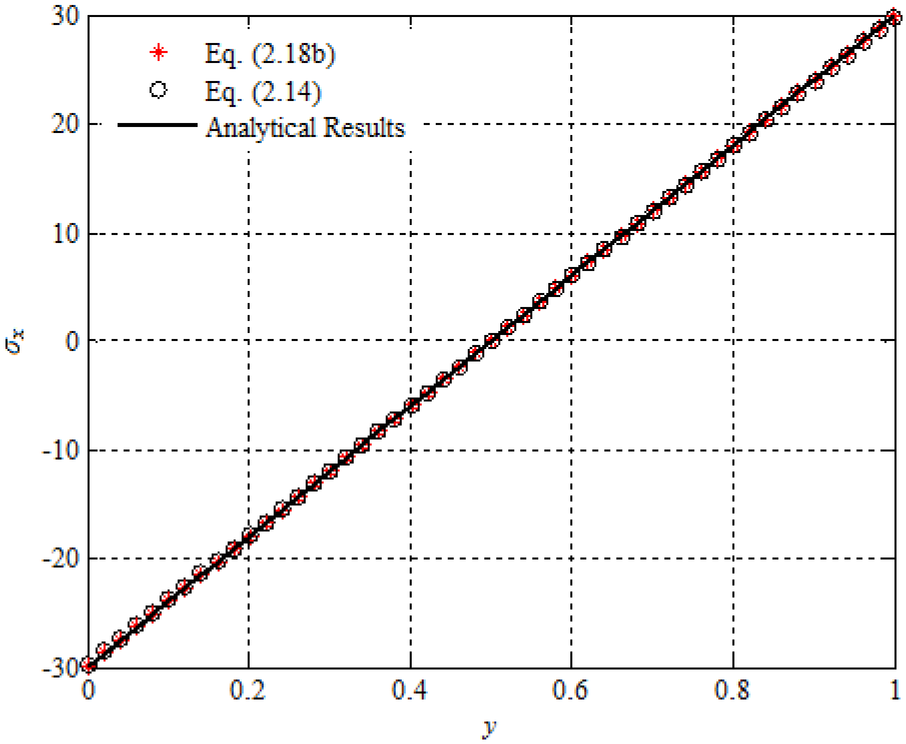

Figure 2.11. Axial Stress, σ_x, along line *AA'*.

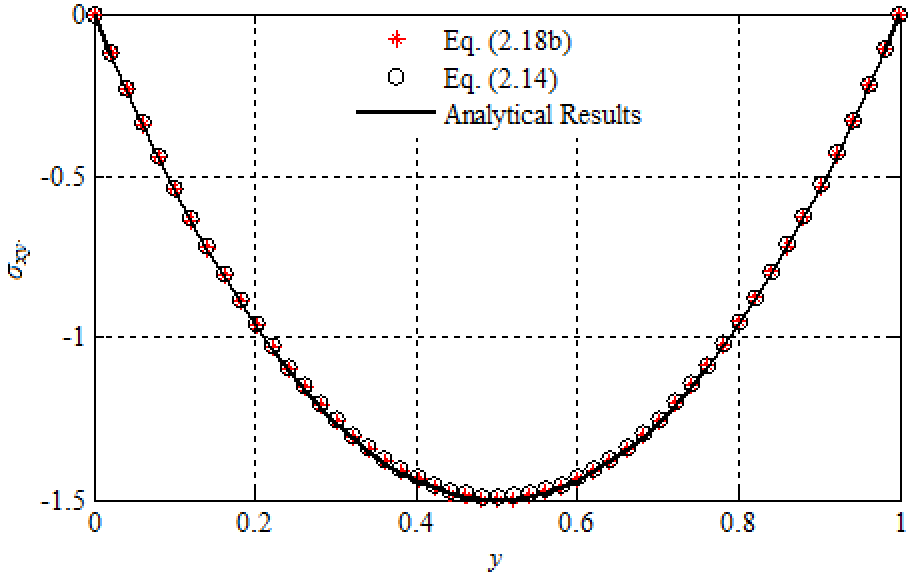

Figure 2.12. Shear Stress along line *AA'*.

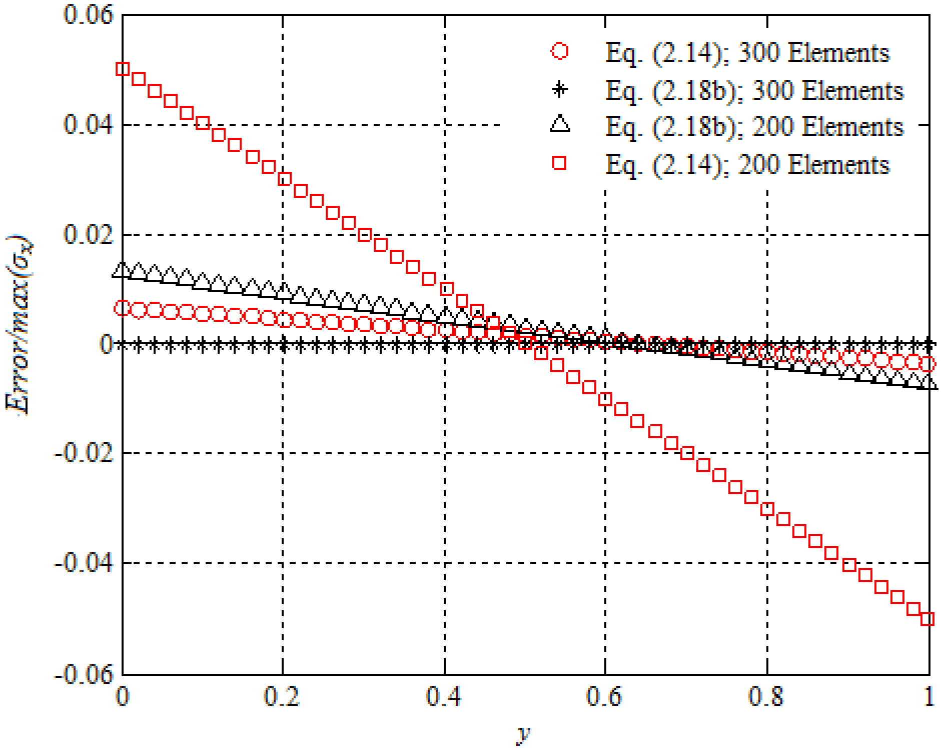

Figure 2.13. Normalized error of the computed axial stress along line *AA'*.

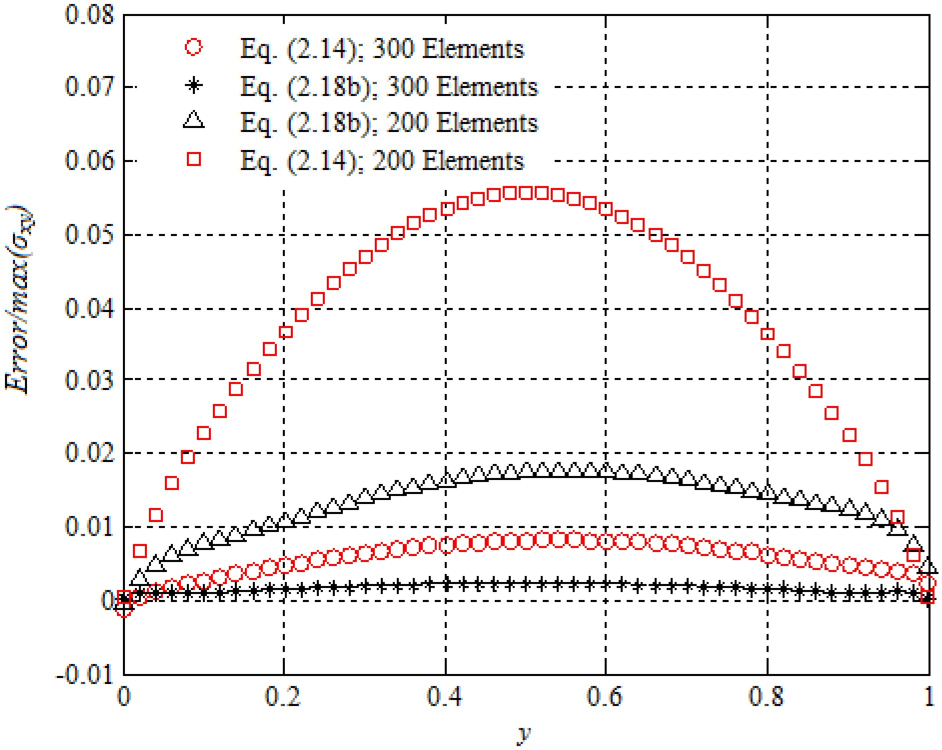

Figure 2.14. Normalized error of the computed shear stress, σ_{xy}, along *AA'*.

2.6.4. Pressurized Thick-Walled Cylinder

In order to show the efficiency of the weakly singular boundary integral equation, Eq. (18b), an internally pressurized hollow cylinder is modeled. The hollow cylinder has an inner radius r_1=1 and an outer radius $r_2 = 2$, and is subjected to an internal pressure *p* of magnitude 1. A quarter of the symmetric cylinder was modeled. The boundary conditions are shown for a sample mesh in Fig. 2.15. The plane stress analytical Lame solution for the hoop stress is

$$\sigma_\theta = \frac{p r_1^2}{r_2^2 - r_1^2}\left(\frac{b^2}{r^2} + 1\right) = \frac{1}{3}\left(\frac{4}{r^2} + 1\right) \qquad (2.36)$$

The numerical results converged to the analytical results with a mesh size of forty linear elements along the straight edges and hundred linear elements along the curved edges. The magnitude of the hoop stress along the horizontal straight edge AB, which is equal to the negative traction, was calculated and plotted in Fig. 2.16. Also, the hoop stress along a quarter circle of radius *r* =1.99 was also computed and tabulated in Table 2.1. The computed results show a great convergence even at internal points very close to the outer curved edge and to the corners.

Table 2.1. Hoop stress at r = 1.99.

Theta (º)	σ_θ (Computed results)	σ_θ (Analytical results)	Error/p
0.5729	0.6476	0.67	-0.022338
5.0156	0.6616	0.67	-0.008399
13.9010	0.6702	0.67	0.000241
18.3437	0.6710	0.67	0.000996
22.7864	0.6713	0.67	0.001364
27.2291	0.6721	0.67	0.002138
36.1145	0.6705	0.67	0.000545
53.8854	0.6708	0.67	0.000780
67.2135	0.6719	0.67	0.001900
71.6562	0.6716	0.67	0.001621
76.0989	0.6709	0.67	0.000926
84.9843	0.6623	0.67	-0.007635
89.4270	0.6531	0.67	-0.001689

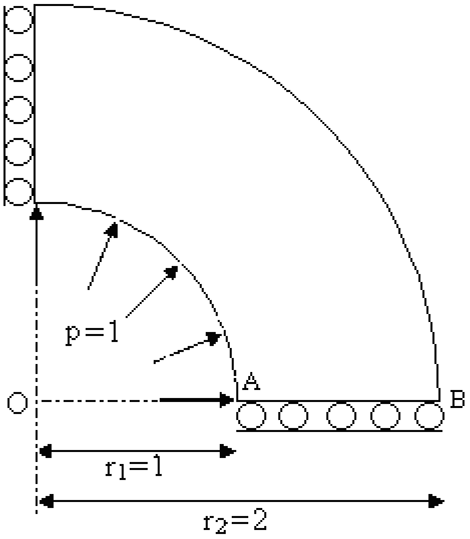

Figure 2.15. An internally pressurized cylinder.

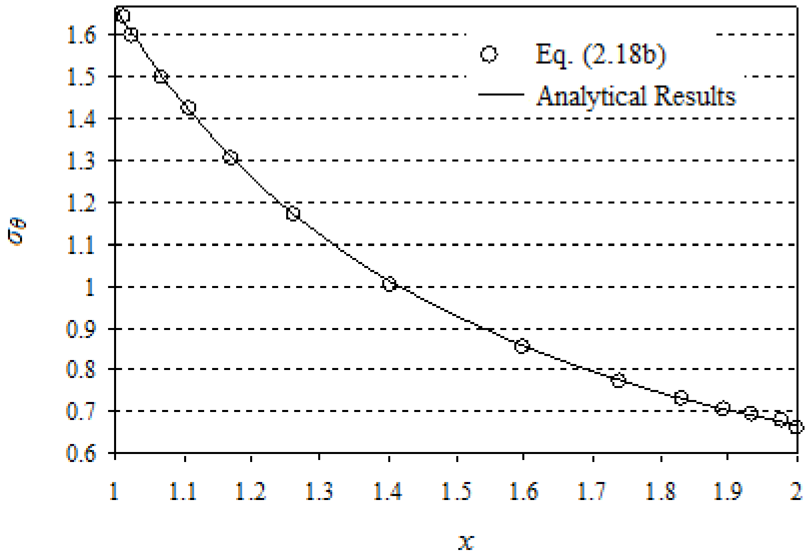

Figure 2.16. Hoop stress along the horizontal straight edge AB of the pressurized cylinder.

2.6.5. Plate with a Hole

A plate 2 x 1 with a circular hole of radius r = 0.1, and subjected to a pure traction in the horizontal direction is modeled. The plate is assumed sufficiently thin for plane stress conditions to be valid. Due to the symmetry, a quarter of the plate is modeled (Fig. 2.17). The numerical scheme developed for Eq. (2.18b) is used to solve for the stress concentration factor. The value obtained is 3.217. Compared with the analytical results, the error is 0.003. This example shows again the advantage of the new formulation in eliminating the boundary layer effect and in providing accurate results close to the corner nodes.

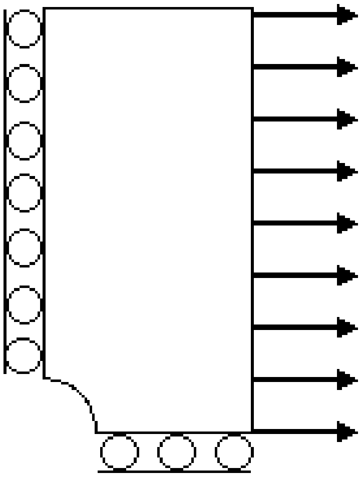

Figure 2.17. Plate with a circular hole under pure traction.

2.7. Conclusion

Using the Stroh formulations for anisotropic materials and the Cauchy theorem, a set of complex variable boundary integral equations in terms of the displacement gradient d**u**/ds and the traction

t are derived. Also, integral expressions that can be used to calculate the stress field are derived. The stress field expressions are first order singular in contrast to their counterparts in the conventional boundary element formulation that have second order singularity. Thus, the boundary layer effect is eliminated in the new formulation. The isotropic forms of the boundary integral equations based on d**u**/ds and **t** are deduced. Numerical schemes to implement these equations are proposed and explicit expressions for isotropic domains are derived. The elastic problems solved in this chapter shows that Eq. (2.14) provided better convergence and more accurate results than Eq. (2.18b) and this is due to its weak singularity. Using Eqs. (2.12a) and (2.12b), the numerical schemes allow the straight forward calculation of stresses at internal points. Though only linear interpolation shape functions are used, accurate calculation of stresses is obtained even at points very close to the boundary.

CHAPTER 3

DISCRETE DISLOCATION PLASTICITY:
A NOVEL BOUNDARY ELEMENT APPROACH

3.1. Introduction

Discrete dislocation plasticity is a method of solving boundary value problems, where plastic flow is represented in terms of the collective motion of discrete dislocations. The dislocations are treated as discrete singular entities in an otherwise elastic continuum. Not until around two decades ago that the collective behavior of discrete dislocations could be simulated, e.g. [66-69]. In these studies, investigations of dislocation pattern formation and of work-hardening relations were carried out in macroscopic solids with infinite or periodic boundary conditions. Thus, the effect of a free surface was not taken into consideration. However, in problems such as contact loading or indentation of thin film image forces due to external surfaces have to be considered so the stress fields in the finite solid bodies have to be calculated.

In 1995, Van der Giessen and Needleman [70] proposed a general approach to solve boundary value problems using discrete dislocation plasticity as in the continuum plasticity. This approach is described in the next section. The Giessen-Needleman approach is based on the formulation of Lubarda et al [71] for equilibrium dislocation arrangements. Boundary value problems are solved by writing the stress and displacement fields as superposition of two fields, $\mathbf{u} = \tilde{\mathbf{u}} + \hat{\mathbf{u}}$ and $\boldsymbol{\sigma} = \tilde{\boldsymbol{\sigma}} + \hat{\boldsymbol{\sigma}}$ .In Fig. 3.1, the (˜)-fields represent the superposition of the field quantities associated with the individual dislocations in their current configuration but in an infinite space. For example, the (˜)-stress field is obtained as $\tilde{\boldsymbol{\sigma}} = \sum_k \sigma_{ij}^{(k)}$, where $\sigma_{ij}^{(k)}$ is the stress field due to the k^{th} dislocation. The (ˆ)-field represents the image field that corrects the boundary conditions. Two sub-problems are solved simultaneously (see Fig. 3.1). In the first sub-problem, the dislocation structure is updated and the (˜)-fields are determined by using well defined analytical formulations [72,73]. In the second, the (ˆ)-fields are calculated by means of numerical techniques such as finite element methods and boundary element methods.

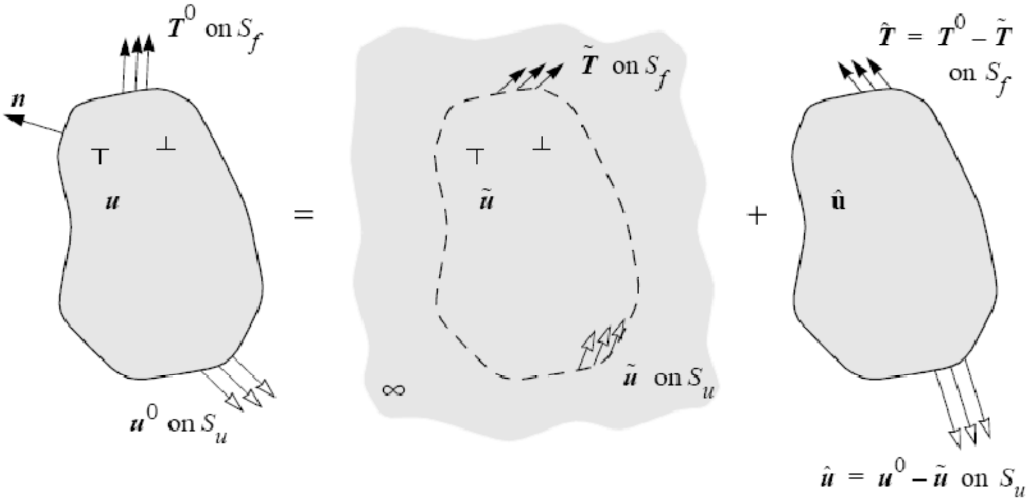

Figure 3.1. Decomposition of the dislocated problem into the two sub-problems: the sub-problem that accounts for the dislocations interactions in the infinite solid ((˜)-fields) and the complementary problem that corrects for the boundary conditions ((ˆ)-fields) [70].

The Giessen-Needleman approach is general and can be extended to solve three-dimensional discrete dislocation plasticity. However, in the case of evolving surfaces, this approach can be computationally expensive and therefore very slow. This is due to the need of re-meshing the domain when the surface evolves.

Boundary element method, due to its fewer degrees of freedom, is very attractive in solving stress field and has its own advantage of reducing calculation cost in the above mentioned cases. The mesh generation and refinement in boundary element method is much simpler than in the finite element method.

In this chapter, a new approach based on the complex variable boundary integral equation is introduced. The new boundary integral formulations developed in Chapter 2 are extended to take into consideration singular fields around dislocations in finite bodies. Thus, additional terms are introduced to the complex variable boundary integral equations developed in Chapter 2. These additional terms are derived for anisotropic materials in Section 3.2 and their forms for isotropic materials are deduced in Section 3.3. As will be shown later in this chapter, the free surface effect, i.e., the image stress, is included implicitly in the new formulations. Therefore there is no need for the superposition technique adopted in the Giessen-Needleman approach [70]. A general framework that can be used to study size dependant plasticity in finite bodies using the new formulation is devised. Two numerical examples that were solved using the Giessen-Needleman technique are adopted and solved using the new boundary element technique. A comparison of the results using the two different techniques is provided to show the robustness and the validity of the new technique.

3.2. Field around an Internal Singular Point

Let's assume that there is a singular stress field around an internal point $z_0 = x_0 + iy_0$ and stresses vanish at infinity. We can construct a contour to circumvent the singular point as shown in Fig. 3.2. Applying Cauchy's theorem Eq. (2.8) to $\mathbf{f}'$ and using Eq. (2.7), we can get the integral expression of $\mathbf{f}'$ in terms of boundary values of $\partial \mathbf{u} / \partial s$ and tractions $\mathbf{t}$, similar to the left hand side of Eq. (2.14). When the outside part of the contour Γ_{out} approaches infinity, because of vanishing $\partial\mathbf{u}/\partial s$ and tractions $\mathbf{t}$ at infinity, the integrations on Γ_{out} vanish. The integrations on Γ_- and Γ_+ cancel each other if displacements across Γ_- and Γ_+ are continuous or just differ by a constant vector. Thus, the stress field can be fully expressed by the integrations on Γ_0. Since z_α is at the outside of Γ_0, $|(\varsigma_\alpha - z_\alpha^0)/(z_\alpha - z_\alpha^0)| < 1$ and the kernel $1/(\varsigma_\alpha - z_\alpha)$ in the integral expression of $\mathbf{f}_\alpha'$ can be expanded around the singular point z_α^0, then

$$f_\alpha'(z_\alpha) = \sum_{n=1} \frac{a_\alpha^{(n)}}{(z_\alpha - z_\alpha^0)^n} \tag{3.1}$$

where $a_\alpha^{(n)}$ is the nth component of a vector $\mathbf{a}^{(n)}$, where $\mathbf{a}^{(n)}$ is given by,

$$\mathbf{a}^{(n)} = \frac{1}{2\pi i}\int_{\Gamma_0(CCW)} \left\langle (\varsigma_\alpha - z_\alpha^0)^{n-1} \right\rangle \cdot \mathbf{L}^{-1} \cdot (\mathbf{B} + \overline{\mathbf{B}})^{-1} \cdot \left(i\frac{d\mathbf{u}}{ds} - \overline{\mathbf{B}} \cdot \mathbf{t}\right)\Big|_{\zeta} ds \tag{3.2}$$

The above integration is along Γ_0, from the upper bank of the cut going counterclockwise to the lower bank.

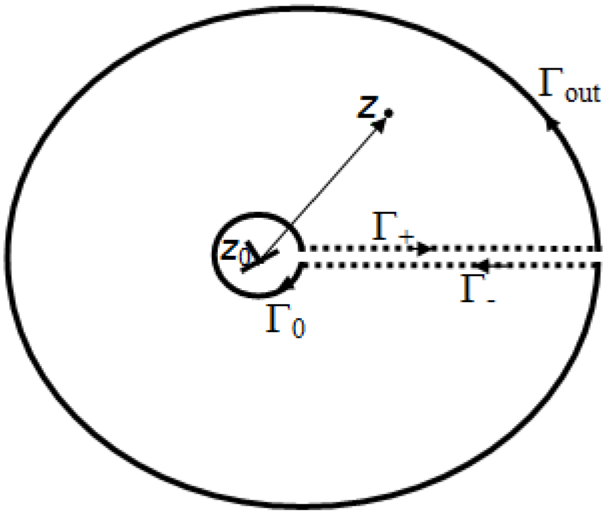

Figure 3.2. The integration contour for field with a dislocation in the z-plane.

When stress has first order singularity around a point $z_0 = x_0 + iy_0$, $d\mathbf{u}/ds$ and tractions **t** have 1/*r* singularity too, and for any $n \geq 2$, $\mathbf{a}^{(n)}$ vanishes as Γ_0 becomes infinitely small. Assume $\oint_{\Gamma_0(CCW)} \frac{\partial \mathbf{u}}{\partial s} ds = \mathbf{b}$ (Burgers vector) and $\oint_{\Gamma_0} \mathbf{t} ds = \mathbf{F}$ (concentrated force), letting **F** = 0, we have

$$\mathbf{a}^{(1)} = \frac{1}{2\pi} \mathbf{L}^{-1} \cdot (\mathbf{B} + \overline{\mathbf{B}})^{-1} \cdot \mathbf{b} \tag{3.3}$$

Thus,

$$f'_\alpha(z_\alpha) = \frac{1}{2\pi} \frac{\mathbf{L}^{-1} \cdot (\mathbf{B} + \overline{\mathbf{B}})^{-1}}{(z_\alpha - z_\alpha^0)} \mathbf{b} \tag{3.4}$$

Here we can see that the two conditions for displacement and traction can be given independently. The stress field around a dislocation is obtained as,

$$[\sigma_{21}, \sigma_{22}, \sigma_{23}]^T = \mathrm{Re}\left[\frac{1}{\pi} .\mathbf{L} \cdot \mathbf{D}(z_\alpha, z_\alpha^0) \cdot \mathbf{L}^{-1} \cdot (\mathbf{B} + \overline{\mathbf{B}})^{-1} \cdot \mathbf{b} \right] \tag{3.5a}$$

$$[\sigma_{11}, \sigma_{12}, \sigma_{13}]^T = -\mathrm{Re}\left[\frac{1}{\pi} .\mathbf{L} \cdot \mathbf{D}_{p_\alpha}(z_\alpha, z_\alpha^0) \cdot \mathbf{L}^{-1} \cdot (\mathbf{B} + \overline{\mathbf{B}})^{-1} \cdot \mathbf{b} \right] \tag{3.5b}$$

And the holomorphic function **f** around a dislocation is obtained from Eq. (3.4) as,

$$f_\alpha(z_\alpha) = \frac{1}{2\pi} \mathbf{L}^{-1} \cdot (\mathbf{B} + \overline{\mathbf{B}})^{-1} \cdot \log(z_\alpha - z_\alpha^0).\mathbf{b} \tag{3.6}$$

3.3. Discrete Dislocation Dynamics Based on the Boundary Element Technique

In this section, we apply the new formulation to a finite solid that has many discrete dislocations inside. In problems involving dislocations, the displacements are not continuous referring to a perfect crystal. The stress field is singular near the dislocations. This singularity is treated by cutting small circles around the dislocations and applying the integral equations Eqs. (2.14) and (2.18b) to the boundary enclosed by the small circles, the cuts, and external boundary. Hence, extra terms are introduced into the left hand sides of Eqs. (2.14) and (2.18b) due to multiple dislocations. For the anisotropic materials, these extra terms are respectively,

$$-\sum_{\mathrm{k}=1}^{\mathrm{n}}\mathbf{L}\cdot<\frac{1}{z_{\alpha}^{(k)}-\varsigma_{\alpha,0}^{(k)}}>\cdot\mathbf{L}^{-1}\cdot(\mathbf{B}+\overline{\mathbf{B}})^{-1}\cdot\mathbf{b}^{(k)} \tag{3.7}$$

$$-\sum_{\mathrm{k}=1}^{\mathrm{n}}\mathbf{A}\cdot<\ln(z_{\alpha}^{(k)}-\varsigma_{\alpha,0}^{(k)})>\cdot\mathbf{L}^{-1}\cdot(\mathbf{B}+\overline{\mathbf{B}})^{-1}\cdot\mathbf{b}^{(k)} \tag{3.8}$$

where n is the total number of dislocations, $z_{\alpha}^{(k)}$ and $\mathbf{b}^{(\mathrm{k})}$ are respectively the position (in z_α plane) and the Burgers vector of the k^th dislocation.

The stress field expressions, shown in Eqs. (2.12a) and (2.12b) also have their own respective additional terms,

$$\sum_{k=1}^{n}\mathbf{L}\cdot\left\langle 1/(z_{\alpha}-z_{\alpha}^{(k)})\right\rangle\cdot\mathbf{L}^{-1}\cdot(\mathbf{B}+\overline{\mathbf{B}})^{-1}\cdot\mathbf{b}^{(k)} \tag{3.9a}$$

$$\sum_{k=1}^{n}\mathbf{L}\cdot\left\langle p_{\alpha}/(z_{\alpha}-z_{\alpha}^{(k)})\right\rangle\cdot\mathbf{L}^{-1}\cdot(\mathbf{B}+\overline{\mathbf{B}})^{-1}\cdot\mathbf{b}^{(k)} \tag{3.9b}$$

Following the same limit taking process as shown in Section 2.4, we obtain the isotropic forms of the additional terms, to be added to the boundary integral equations (2.21a) and (2.21b) respectively,

$$-\sum_{k=1}^{n}\left\{\frac{1}{z^{(k)}-\zeta_{0}}\mathbf{I}-\frac{y^{(k)}-y_{0}}{z^{(k)}-\zeta_{0}}\cdot\begin{bmatrix} i & -1\\ -1 & -i\end{bmatrix}\right\}\cdot\mathbf{b}^{(k)} \tag{3.10a}$$

$$-\sum_{k=1}^{n}\left\{\ln(z^{(k)}-\zeta_{0}).\mathbf{I}+\frac{y^{(k)}-y_{0}}{z^{(k)}-\zeta_{0}}\cdot\frac{1}{2\mu}\begin{bmatrix} 1 & i\\ i & -1\end{bmatrix}\right\}\cdot\mathbf{b}^{(k)} \tag{3.10b}$$

where $z^{(k)}=x^{(k)}+iy^{(k)}$ and $\varsigma_{0}=x_{0}+iy_{0}$.

In numerical implementation, these terms only contribute to the right side force vector of the linear algebraic system, and have no effect on the matrix. When all the boundary values are solved, the internal stress field due to the external load and the dislocations can be calculated by adding the following terms respectively to Eqs. (2.22a) and (2.22b)

$$\frac{\mu}{2\pi(1-\upsilon)}\mathrm{Re}\sum_{k=1}^{n}\left\{\frac{1}{z-z^{(k)}}\mathbf{I}-\frac{y-y^{(k)}}{z-z^{(k)}}\begin{bmatrix} i & -1 \\ -1 & -i \end{bmatrix}\right\}\cdot\mathbf{b}^{(k)} \tag{3.11a}$$

$$\frac{\mu}{2\pi(1-\upsilon)}.\mathrm{Re}\sum_{k=1}^{n}\left\{\frac{1}{z-z^{(k)}}\mathbf{I}-\frac{y-y^{(k)}}{z-z^{(k)}}.\begin{bmatrix} -1 & -i \\ -i & 1 \end{bmatrix}+\begin{bmatrix} 2i & -1 \\ -1 & 0 \end{bmatrix}\right\}\cdot\mathbf{b}^{(k)} \tag{3.11b}$$

It is necessary to emphasize that writing the stress caused by dislocations in complex form saves computational work. Thus, when calculating the stress field caused by any dislocation at any internal point or at any other dislocation, there is no need to use local coordinates systems attached to the dislocation then transform back to the global coordinate system in order to collect the stress caused by all the dislocations.

3.4. Evolution of the Dislocation Structure

In discrete dislocation plasticity, dislocations are treated as discrete entities that interact with each other and with the surface of the body. Interaction among dislocations is divided into two categories: long range interactions and short range interactions. Long range interactions are calculated directly from the elasticity theory (Eqs. 3.11) which can represent accurately dislocation fields beyond 5*b*-8*b* from the core, where *b* is the magnitude of the Burgers vector.

Dislocation glide and short range interactions such as nucleation and annihilation are controlled by atomistic processes and thus cannot be resolved in discrete dislocation plasticity. Therefore, constitutive rules are needed to model these mechanisms in two-dimensional discrete dislocation plasticity.

3.4.1. Dislocation Glide

Dislocations move on slip planes driven by the so called Peach-Koehler force which acts on the dislocation per unit length. In vector form, the Peach-Koehler formula is written as,

$$\mathbf{f} = (\boldsymbol{\sigma}.\mathbf{b}) \times \boldsymbol{\xi} \qquad (3.12)$$

where $(\times)$ is the cross product, (**.**) is the dot product, $\boldsymbol{\sigma}$ is the stress state tensor at the dislocation line, **b** is the Burgers vector of the dislocation and $\boldsymbol{\xi}$ is the tangent vector to the dislocation line. In planar domains, the tangent vector $\boldsymbol{\xi}$ is perpendicular to the plane and can be taken as $\boldsymbol{\xi}$ = [0, 0, 1]. Using the superscript k to denote an edge dislocation, the resolved driving force is

$$f^{(k)} = \tau^{(k)} b^{(k)} \qquad (3.13)$$

where $\tau^{(k)}$ is the resolved shear stress in the slip plane at the dislocation line and $b^{(k)}$ is the magnitude of the Burgers vector. Neglecting the inertia effects of dislocations, the magnitude of the glide velocity $v^{(k)}$ becomes linearly related to the Peach-Koehler force through $f^{(k)} = Bv^{(k)}$ and therefore Eq. 3.13 is re-written as,

$$\tau^{(k)} b^{(k)} = Bv^{(k)} \qquad (3.14)$$

where B is the drag coefficient.

3.4.2. Dislocation Nucleation

In a crystal, dislocations nucleate from internal defects to account for the large strains that are produced. Edge dislocations can nucleate from Frank-Read sources. Under the effect of the resolved shear stress, a single segment of an edge dislocation that gets pinned at internal defects bows out by glide. A stress applied continuously to the pinned dislocation segment will cause the radius of curvature of the dislocation line to increase and the dislocation line becomes unstable. Two sections of the curved line annihilate each other and form a closed outer dislocation loop that can freely propagate on the glide plan leaving a dislocation segment anchored between the internal defects.

The Frank-Read mechanism has been used widely in discrete dislocation plasticity [70,74,75]. In two-dimensional discrete dislocation plasticity, this phenomenon is approximated as follows. A Frank-Read source is represented by a point source on a slip plane. If the resolved shear stress acting on the source exceeds a critical value τ_{nu} during a period of time t_{nu}, two edge dislocations of opposite Burgers vectors are nucleated at a distance L_{nu} as shown in Fig. 3.3. The polarity of the nucleated dipole is determined by the sign of τ_{nu}. The values of these three variables τ_{nu}, t_{nu} and L_{nu} depend on the length of the initial Frank-Read segment, the elastic properties and the drag coefficient. The distance between the nucleated dislocations is related to the critical shear stress τ_{nu} by,

$$L_{nu} = \frac{\mu}{2\pi(1-\upsilon)} \frac{b}{\tau_{nuc}} \tag{3.15}$$

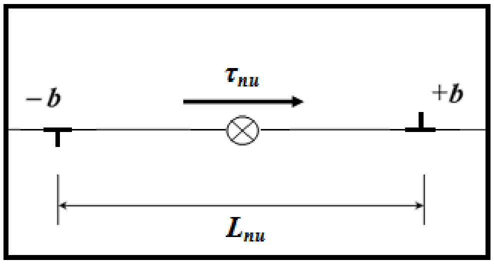

Figure 3.3. A Schematic diagram of dislocation nucleation from a Frank–Read source.

3.4.3. Dislocation Annihilation

In two-dimensional discrete dislocation plasticity, dislocation annihilation is modeled as follow. When two dislocations of opposite Burgers vectors glide closer than 6*b* to each other, they annihilate each other. The annihilated dislocations are taken out of the simulations.

3.4.4 Dislocation Pinning

Gliding motions of dislocations may get hindered by other defects. We model these defects as point defects that are distributed randomly along predefined slip planes. A dislocation that meets a point defect is pinned and is allowed to overcome this obstacle only if its resolved shear stress is larger than a threshold stress called τ_{obs}.

3.5. Numerical Implementation

In discrete dislocation plasticity, quasi-static boundary value problems are solved in an incremental manner. At each time step, the fields are determined inside the dislocated body and the evolution of the dislocation structure is updated in accordance with the current fields. In discrete dislocation plasticity, if the boundary does not move, the stiffness matrix is fixed and dislocation motion only changes the generalized force vector. The numerical schemes developed in Chapter 2 for the integral Eqs. (2.14) and (2.18b) and their corresponding isotropic forms are still valid to form the stiffness matrix. However, the additional terms introduced in this chapter due to dislocation fields have to be added to the generalized force vector. Isotropic expressions of the dislocation terms are given respectively by Eqs. (3.10a) and Eq. (3.10b). The stress field can be calculated using the numerical expressions developed for Eqs. (2.22) in addition to the isotropic forms of the dislocations terms that are given in Eqs. (3.11).

Isotropic forms of the numerical schemes developed for the weakly singular boundary integral equations, Eq. (2.18b) with extra terms from Eq. (3.10b), are used in the following two examples to study the plastic deformation of a crystal under pure bending and of a polycrystal under pure shearing. These two examples are picked because they had been respectively simulated by Cleveringa et al. [74] and Balint et al. [75] using the superposition technique and the finite element method. In these simulations, dislocations are constrained to glide along slip planes where they were originally nucleated.

We adopt the same material modeling and parameters in Cleveringa et al. [74] and Balint et al. [75] so that direct comparison can be made. Materials are originally free of dislocations. Bulk sources are distributed randomly following a Gaussian distribution with mean nucleation strength of 50 MPa and a standard deviation of 10 MPa. The time step is fixed as Δt = 0.5 ns and the nucleation time as t_{nu} = 10 ns. The distance between adjacent slip planes is taken to be 100b.

Materials properties are taken to be those of Aluminum where Young's modulus E = 70 GPa, Poisson ratio ν = 0.33, drag coefficient $B = 10^{-4}$ Pa.s and the Burgers vector length b = 0.25 nm. The so called Peierls stress that resists dislocation gliding is taken to be zero.

3.5.1. Bending of a Single Crystal

The bending of a single crystal of length L = 12 μm and height h = 4 μm is simulated using the developed boundary element approach. The bending load is modeled by prescribing the slope of the left and right edges of the single crystal (Fig. 3.4). In terms of the displacement gradient, this is defined as $\partial u/\partial s = \theta$, where u is the displacement in the x direction. The bending rate is taken to be $\dot{\theta} = 0.5 \times 10^3\ \mathrm{s}^{-1}$. In this example, the material is considered to be free of obstacles.

Geometric configuration of slip systems is similar to that in Cleveringa et al. [74]. The crystal has three slip systems inclined at angles $\varphi = \pm \pi/6$ and $\varphi = \pi/2$ from the x axis as shown in Fig. 3.5. The $\pi/2$ slip planes are confined to a central region of size $\mathrm{L} - \mathrm{h}/\tan(\frac{\pi}{6})$. The $\pm \pi/6$ slip planes are confined geometrically to a region such that intersection with the vertical edges where the rotation is prescribed does not occur. Therefore, dislocations can only exit the crystal from the top or bottom edges. Dislocations are divided evenly between the three slip systems. In total there are 404 slip planes and 808 bulk sources.

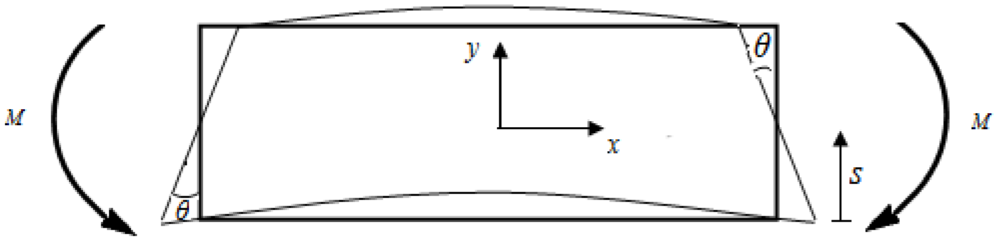

Figure 3.4. A Single crystal under pure bending.

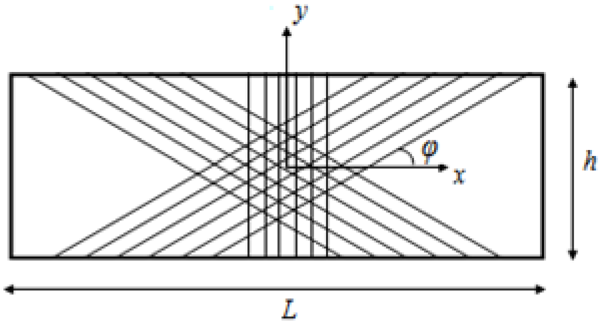

Figure 3.5. Sketch of the boundary value problem.

To show mesh independence of the results, three simulations with different mesh sizes (mesh1, mesh2 and mesh3) are conducted. Mesh1, mesh2 and mesh3 have respectively 200 nodes, 400 nodes and 800 nodes distributed evenly along the four edges of the crystal. The resultant bending moment normalized with a reference moment $\mathrm{M_{ref}} = \frac{2}{3}\bar{\tau}_{\mathrm{nu}}(\frac{\mathrm{h}}{2})^2$, is plotted versus the prescribed slop θ. As shown in Fig. 3.6, for the three different meshes, the crystal has yielded at approximately the same bending moment with less than 10 % difference between the coarse mesh, mesh1, and the other finer meshes, mesh2 and mesh3. This is due to the fact that the linear shape functions used do not model bending problems accurately and usually require fine meshes.

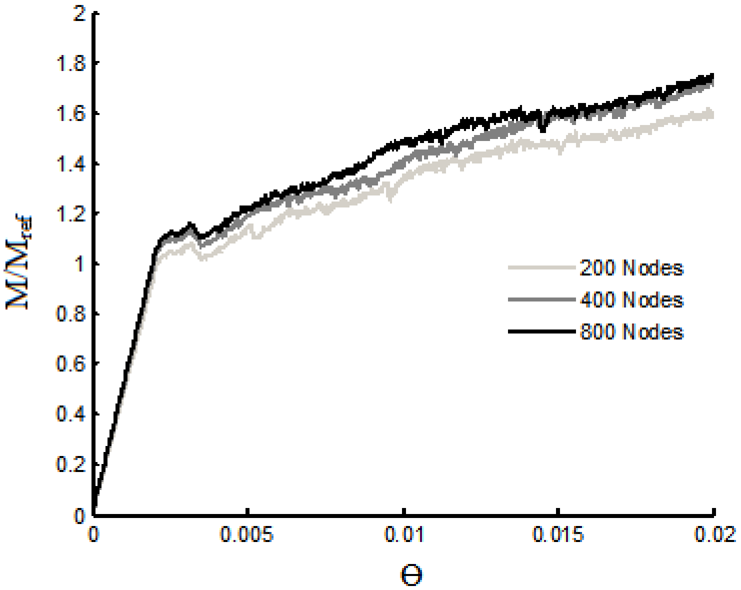

Figure 3.6. Convergence of the boundary element results.

In Fig. 3.7, the boundary element results are compared with the finite element results obtained in [74]. Both methods have showed similar behavior of the crystal under bending. The first nucleation incidence occurred in our simulations at a lower moment than in Cleveringa et al.[74]. This may explains the quantitative difference between the two methods from the yielding point up to θ = 0.08. However, for θ > 0.08, both methods have surprisingly provided close results. A comparison of dislocation distribution at θ = 0.002 obtained from the two methods is plotted in Figs 3.8(a) and 3.8(b). It is worth noting that although similar slip planes in both methods are active, dislocations are more uniformly distributed in the boundary element results. The possible reason for this is that the internal stress and its variation in the field calculated from the boundary element method are much smoother than the stress field calculated by the finite element method, which is greatly affected by the mesh geometry, shape function and integral points.

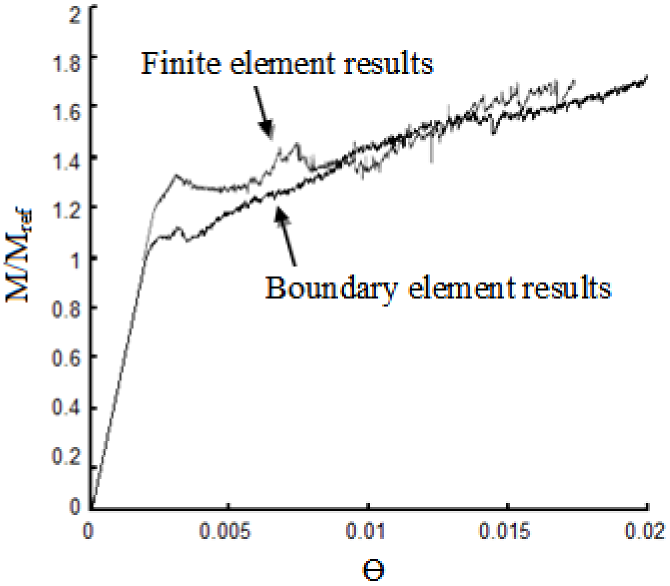

Figure 3.7. Comparison of the boundary element results with the finite element results in Cleveringa et al. [74] for the single crystal under bending.

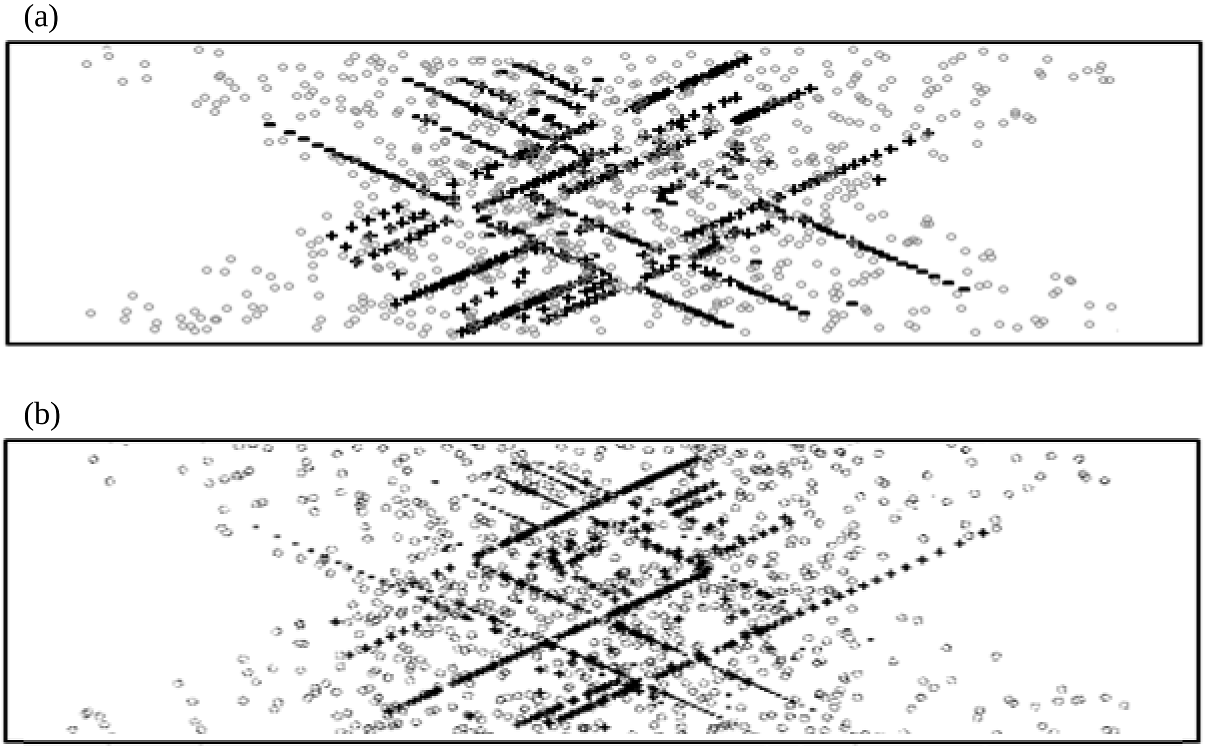

Figure 3.8. Dislocation distribution results at θ = 0.0175. (a) Boundary element results.(b) Finite element results [74]. The gray circles are Frank-Read sources, (+) are positive dislocations and (-) are negative dislocations.

3.5.2. Polycrystal under Pure Shearing

The model used in this paper is similar to the one studied in Balint et al. [75]. A square polycrystal of size 10x10 μm^2 is composed of *n* square grains in each direction. The grains are arranged analogously to a checkerboard; the adjacent grains have slip systems with different orientations (Fig. 3.9). Each grain has only one slip system with slip planes oriented either horizontally or vertically. Density of the Frank-Read sources is taken to be $\rho_{src} = 20\ \mu m^{-2}$. In order to prevent separation of a new born dipole between two adjacent grains, the distance between sources and the grain boundaries is set to be larger than the radius of the nucleation zone, $0.5L_{nu}$. Transmission of dislocations through the grain boundaries is not allowed. Obstacles with a prefixed density $\rho_{obs} = 40\ \mu m^{-2}$ are randomly distributed along the different slip planes. These obstacles are treated as fixed points. A dislocation cannot surpass the point obstacle unless the Peach-Koehler force on the dislocation exceeds the obstacle strength which is taken to be 150 MPa.

The polycrystal is subjected to pure shearing, prescribed through the gradient displacement boundary conditions (Fig. 3.9). The prescribed shear strain is increased at the rate $\dot{\gamma} = 2000\ \mathrm{s}^{-1}$. Polycrystals with two different grain sizes, d = 2.5 μm and d = 0.5 μm, are simulated. The work conjugate shear stress defined as $\tau = \frac{1}{L^2} \oint t_i\, u_i\, ds$, is plotted against the shear strain for the two simulated cases and compared with the finite element results obtained in Balint et al. [74] (Fig. 3.10). For the grain size d = 2.5 μm, the boundary element results have shown softer response of the polycrystal than the finite element results. However, the results from both methods are qualitatively very similar to a big extent. For the grain size d = 0.5 μm, the two methods have provided very close results.

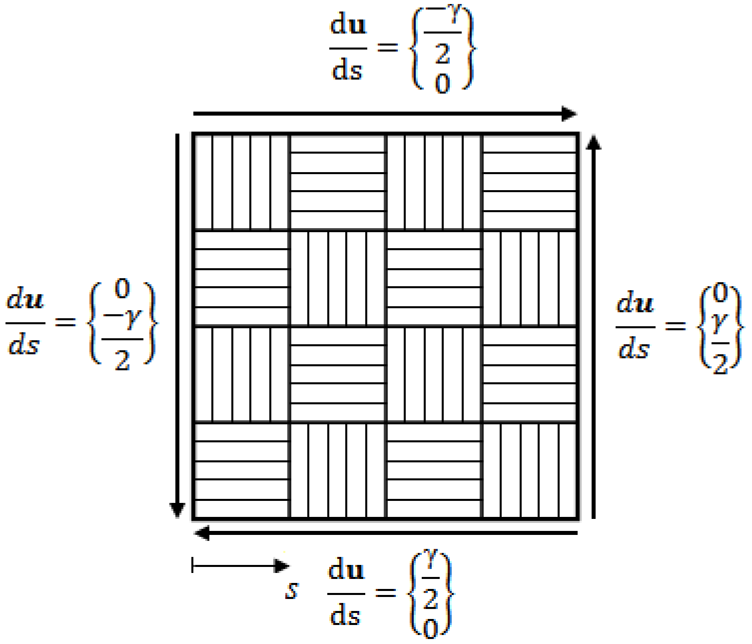

Figure 3.9. Sketch of the checkerboard like polycrystal under pure shearing.

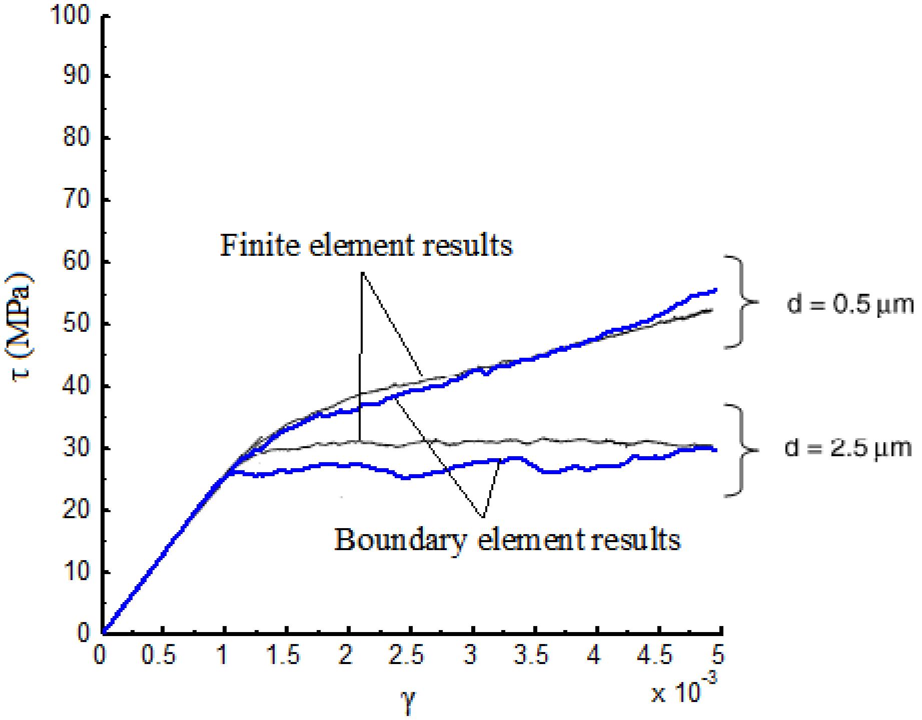

Figure 3.10. Comparison of the boundary element results with the finite element results in Balint et al. [75] for the polycrystal under pure shearing.

3.6. Conclusion

The boundary integral equations derived in Chapter 2 are extended to take into consideration singular fields due to dislocations in finite bodies. Combined with discrete dislocation dynamics, the formulation provides a direct approach to solve mesoscopic plasticity problems in a finite body with many discrete dislocations, without the use of superposition method proposed by Van der Giessen and Needleman [70]. Two such examples are simulated: the plastic behavior of a crystal under pure bending and that of a polycrystal under pure shearing. The results are very close to the finite element results in Cleveringa et al. [74] and Balint et al. [75]. Due to the inherent mathematical structure of the boundary element method, it provides a smoother internal stress field than the one calculated by the finite element method, which usually generates artificial non-smooth stress field at the boundaries of neighboring elements. It is worth mentioning that the calculation cost in these simulations is low. For example, the first problem about the bending of single crystal can be solved in a time period that ranges from two hours for the coarse mesh up to 6 hours for the fine mesh, in a regular Dell Precision Computer without any upgrade.

CHAPTER 4

MULTI-ASPERITIES CONTACT WITHOUT BULK SOURCES

4.1. Introduction

A main interest of this dissertation is the micro-structural deformation of rough surfaces. We do not consider only the contact of single asperities but the contact of many asperities focusing on how the different parts of the surface interact with each other and the factors that drive the pattern formation. We propose a Multi-Asperities model to capture the complexity of the multi-scale nature of rough surfaces under contact. In this chapter, the proposed Multi-Asperities model is described and the boundary value problem is solved using the discrete dislocation approach described in Chapter 3. Only nucleation of dislocations from surface-steps is considered in this chapter. Effect of bulk sources on the microstructure deformation and pattern formation underneath the surface is presented in Chapter 5. The results obtained are presented and discussed. Finally, further improvements of the model are proposed.

In the proposed Multi-Asperities model, the rough surface of a material is idealized by a periodic array of asperities of rectangular shapes. The model is illustrated in Fig. 4.1, where δ is the height of the asperity, AS is the width of the asperity and w is the period of the rough surface. The main difference between the proposed Multi-Asperities model and the Unit-Step model described in Chapter 1 is that the interaction between adjacent asperities is considered. The collective effect of an array of contacts when considered has important consequences such as neighboring hardening, i.e., when dislocations generated under different asperities interact.

Another important feature that differentiates our model from the theoretical Unit-Step model is that our model is capable of dealing with a large number of dislocations.

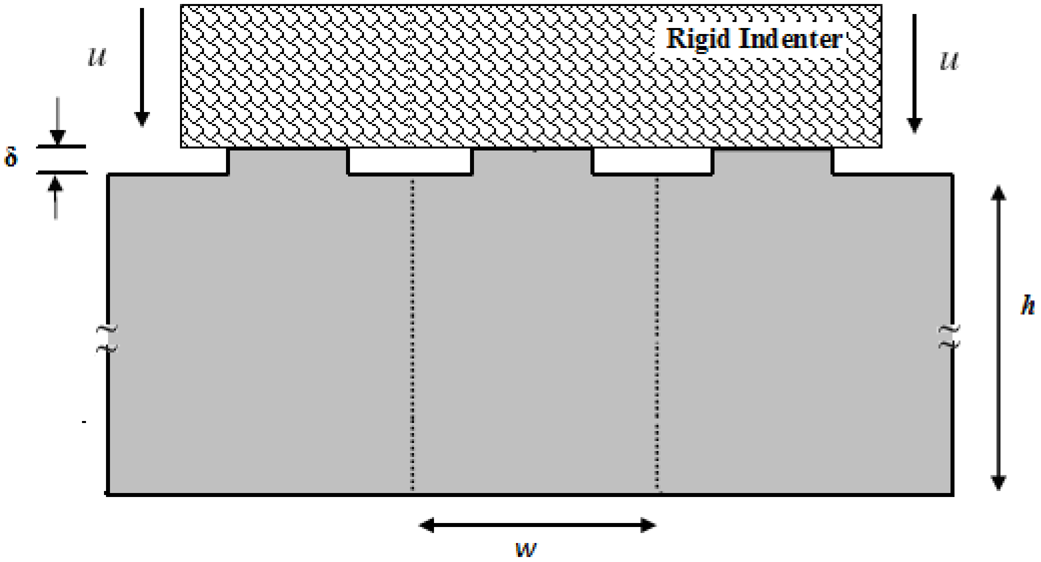

Figure 4.1. A Semi infinite crystal with a rough surface indented by a rigid flat indenter.

4.2. Description of the Boundary Value Problem

The problem to be studied is a semi-infinite single crystal in the horizontal direction with a rough surface under indentation. The problem can be reduced to a finite one by considering the domain as a set of an infinite number of unit cells of sizes $w \times h$, where periodic boundary conditions are imposed on the two opposite sides of the unit cell. Thus, a dislocation that leaves the unit cell from a side is inserted back from the opposite side. The material is assumed to be initially free of defects of any kind. Plastic flow occurs in the crystal as a result of the nucleation of edge dislocations from the surface-steps and their motions along slip planes that emanate from the surface-steps as illustrated in Fig. 4.2. Each edge dislocation is associated with a Burgers vector of fixed magnitude and of direction parallel to the slip plane along which it can glide. The dislocation line direction is perpendicular to the plane of deformation.

4.2.1. Boundary Conditions

The contact conditions considered are those of a frictionless contact; thus, the indenter is free to slide along the surface of contact where the shear stress vanishes. There is no contact between the indenter and the gap between adjacent asperities. The bottom surface of the unit cell is assumed to be free to move in the lateral direction but is fixed in the longitudinal direction. No lateral displacement is assumed along the two sides of the simulation cell. Also, there is no shear stress along the two sides. The governing integral equation used to solve the boundary value problem is given in terms of the displacement gradient vector $\partial \mathbf{u}/\partial s$ and the traction vector **t**. Thus, the boundary conditions are

$$t_x = 0,\ \partial u_y / \partial s = 0;\ 0 \le x \le w \text{ and } y = 0. \tag{4.1}$$

$$t_x = t_y = 0;\ x = (w \pm AS)/2 \text{ and } h \le y \le h + \delta \tag{4.2}$$

$$t_y = 0,\ \partial u_x / \partial s = 0;\ x = 0 \text{ or } x = w \text{ and } 0 \le y \le h \tag{4.3}$$

$$t_x = t_y = 0;\ 0 \le x \le w \text{ and } y = h \tag{4.4}$$

The loading condition along the contact surface is imposed by prescribing the normal displacement under the contact in an incremental manner. This can be achieved by satisfying the following equation,

$$\int_A^C \frac{\partial u_y}{\partial s} ds = -\int \dot{u} dt \tag{4.5}$$

where the prescribed displacement rate, $\dot{u}$, is taken to be $\dot{u} = 4 \times 10^4\ \mu m/s$.

The unit cell is free to move horizontally. Therefore, the periodic boundary conditions on the sides of the unit are imposed with the following equations,

$$\int_{B}^{D} \frac{\partial u_x}{\partial s} ds + V = 0 \tag{4.6a}$$

$$\int_{B}^{D} \frac{\partial u_y}{\partial s} ds = 0 \tag{4.6b}$$

The constant *V* is determined by assuming that the resultant horizontal forces acting on any of the two sides of the cell vanish. This is satisfied by requiring that,

$$\frac{1}{h}\int_{A}^{B} t_x(w, y)dy = 0 \tag{4.7}$$

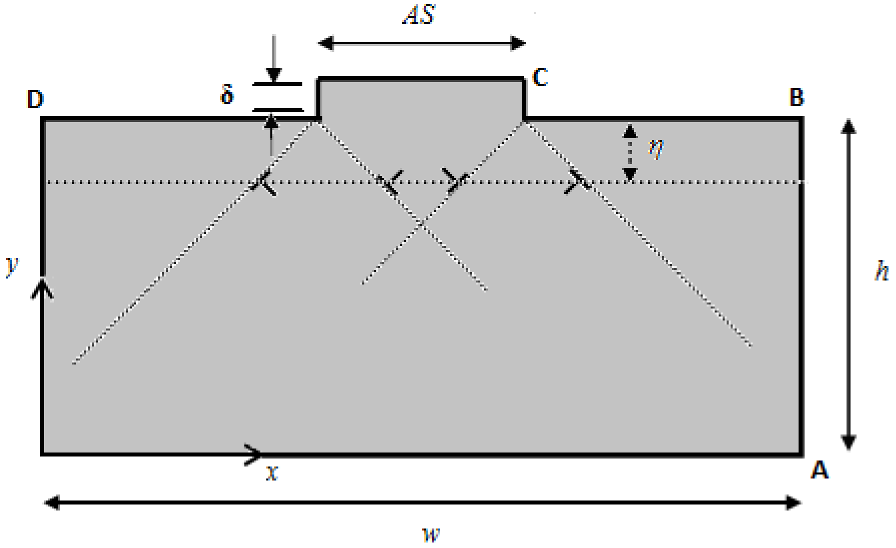

*Figure 4.2***.** Simulated unit cell including dislocations gliding along different slip planes where *w* is the width of the unit cell, *AS* is the width of the asperity.

4.2.2. Governing Equations and Constitutive Rules

The calculations are carried out using the plane strain two-dimensional discrete dislocation plasticity method developed in Chapter 3. The boundary value problem is solved using the isotropic forms of the numerical schemes developed for the weakly singular boundary integral equation (Eq. (2.18b)) with the corresponding extra term (Eq. (3.10b)). Similarly, the internal stress field is calculated using the isotropic forms of the numerical schemes developed for Eqs. (2.12) with their associated extra terms given by Eqs. (3.11).

Nucleation of dislocation from bulk sources is not allowed. The Rice-Thomson criterion [52] is used to model dislocation nucleation from surface-steps. If the driving force on a dislocation at a distance η from the surface step is greater than the Peierls force, the dislocation is emitted. The distance η and its corresponding Peierls force f_p are determined by atomistic simulations in Yu et al. [47]. The parameter η characterizes the size of the dislocation emission process zone near the step. The dislocation glides only if the driving force overcomes the Peierls force. Once a dislocation is nucleated from a surface step, the Burgers vector is accommodated by the surface step, which is accounted for by means of an appropriate image dislocation above the surface. Thus, the strength of a surface step dislocation source depends on the number of dislocations it has generated. This step-height dependency is not accounted for in our calculations. Dislocation glide is controlled by the Peach-Koehler force. In a two dimensional domain, the glide component of the kth dislocation is written explicitly as,

$$f_k = \frac{b_k}{2}\left[(\sigma_{xx} - \sigma_{yy})\sin 2\theta_k - 2\sigma_{xy}\cos 2\theta_k\right] \tag{4.8}$$

where θ_k is the slip plane angle and b_k is the magnitude of the Burgers vector. Given that the glide component is bigger than the Peierls force, the glide velocity v_k is calculated as,

$$v_k = (f_k - b_k \tau_p sign(f_k))/B \tag{4.9}$$

where τ_p is the Peierls stress and B is the drag coefficient. Displacement of the dislocation along the slip plane is determined through the explicit Euler integration technique, $u_k = v_k \Delta t$. The time step is taken to be $\Delta t = 0.005$ ns.

4.2.3. Geometry and Material Properties

The height h of the unit cell and the step height δ are fixed, respectively, as $h = 50$ µm and $\delta = 0.02$ µm. The simulations are carried out for various widths of the unit cell and various ratios of the asperity width to the unit cell width, *AS/w*. The material is elastically isotropic where the shear's modulus $\mu = 183e3$ MPa and the Poisson's ratio $\nu = 0.43$. The magnitude of the Burgers vector is equal to the lattice constant of Gold $b = 4.08$ A°. The size of the nucleation process zone and the corresponding Peierls force are taken respectively as $\eta = 5b$ and $f_p/\mu b = 0.001$. The drag coefficient is taken as $B = 10^{-4}$ Pa.s.

4.3. Simulation Results

Let us note first that a quantitative comparison between the results discussed in this chapter and the results obtained in [47,54] is not possible. This is due to the following reasons. They have used continuum formulations; adhesion energy was considered and finally the contact conditions they simulated are those of a perfectly sticking contact. However, a qualitative comparison is provided in the rest of this chapter in addition to the new phenomenon revealed by our simulations. The surface-steps are differentiated by their locations at the right corner or the left corner of the asperity and the slip planes emanated from the surface-steps are differentiated by their inclination angle θ with respect to the x axis.

4.3.1. Isolated Single Steps

We start our analysis by studying the dislocation behavior underneath the contact area in the case of an isolated single step (see Fig. 4.3). To eliminate the effect of the periodic boundary conditions, the width of the unit cell is taken to be large enough, w = 50 µm. Also, the size of the asperity is set to be AS = 10 µm so the interaction between dislocations nucleated form opposite steps is negligible. Only nucleation from the left surface step is allowed and hence the nucleation source at the right corner is suppressed. Three different cases are considered: (1) only the slip plane at $\theta = -3\pi/4$ is activated, (2) only the slip plane at $\theta = -\pi/4$ is activated, (3) both of these slip planes are activated. For the first two cases, the equilibrium positions, l/b, of the first few nucleated dislocations are plotted against the mean pressure, P_m, in Figs. 4.4(a) and (b), where

$$P_m = -\frac{1}{AS}\int_{(w-AS)/2}^{(w+AS)/2} \frac{\sigma_{yy}(x, h+\delta)}{\mu}\, dx \tag{4.10}$$

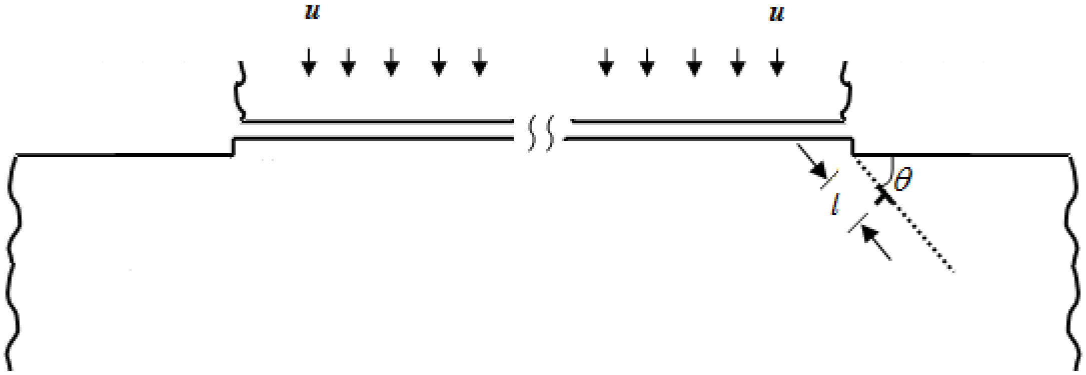

Figure 4.3. A schematic illustration of a rough surface with isolated surface-steps.

A comparison between the curves in Fig. 4.4(a) and the curves in Fig. 4.4(b) show that the slip plane at θ = -3π/4 yields at a lower mean contact pressure than the slip plane at θ = -π/4. However, as the mean contact pressure increases, dislocations nucleated along the right slip plane (θ = -π/4) moves easily towards the bulk while dislocations nucleated along the left slip plane (θ = -*3π/4*) stay close to the surface step from which they were nucleated. This different behavior of dislocations nucleated from surface-steps is called dislocation segregation into pro-load and anti-load types. This is due to the applied remote load. Dislocation segregation was observed in the Unit-Step model developed by Yu et al. [47].

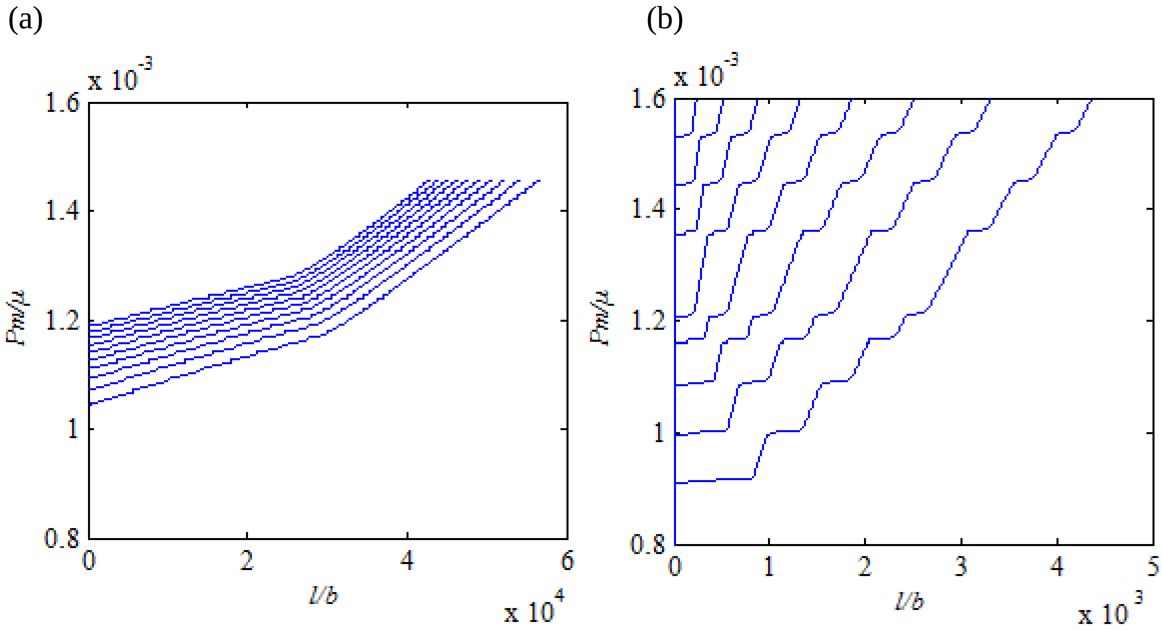

Figure 4.4. Normalized mean contact pressure, P_m/μ, versus dislocation distance to the surface step *l/b*. (a) for dislocations moving along the slip plane at θ = -π/4, (b) for dislocations moving along the slip plane at θ = -3π/4.

In Fig. 4.5, the number of dislocations nucleated along the slip planes at θ = -3π/4 and θ = -π/4 is plotted against the mean contact pressure, P_m, for the cases when each slip plane is activated separately and when the two slip planes are activated at the same time. As shown in Fig. 4.5, for the cases when each slip plane is activated separately, it is easier to nucleate the first few dislocation along the slip plane at θ = -3π/4 than along the slip plane at θ = -π/4. However as the number of nucleated dislocations increases, it becomes a lot easier to nucleate dislocations along the slip plane at θ = -π/4. This is due to the fact that the dislocations nucleated along the slip plane at θ = -3π/4 are of the anti-load type and thus they pile up underneath the surface making it difficult for subsequent anti-load dislocations to nucleate from the surface-steps. When the two slip planes are active at the same time, the mean pressure required to nucleate subsequent dislocations along either of the two slip planes is dropped. This phenomenon is called latent softening. The same phenomenon was observed in Gao et al. [55].

Furthermore, while the drop in the mean pressure for the plane at θ = -3π/4 is constant, the drop in the mean pressure for the slip plane at θ = -π/4 increases with the number of dislocations. It is worth noting that the number of pro-load dislocations is still larger than the number of anti-load dislocations and this due to the fact that anti-load dislocations pile up close to the surface and thus generate a large back stress that suppresses the anti-load source. Therefore, dislocation segregation observed in the case of individual slip planes still hold when the two slip planes are activated together.

A final note is that there is no change in the mean contact pressure required for the nucleation of the first dislocation along the slip left plane. This is because the Rice-Thomson model does not take into consideration the instability along the slip planes before a dislocation is nucleated.

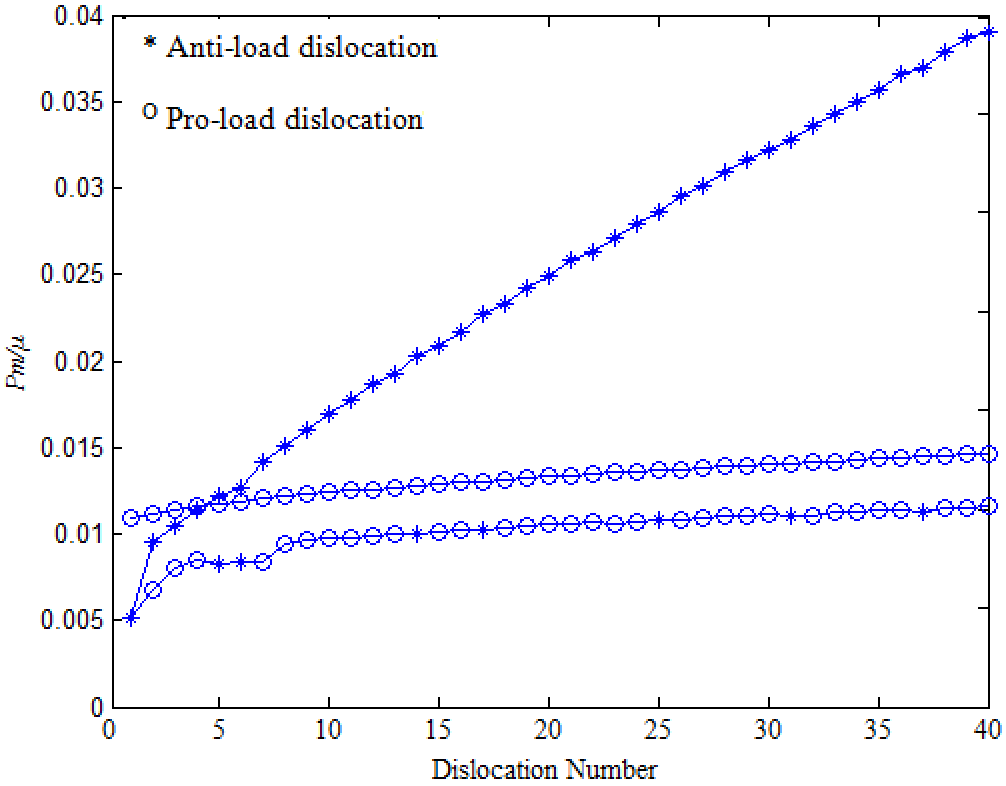

Figure 4.5. Effect of the mutual interactions between the two slip planes at $\Theta = -\pi/4$ and $\Theta = -3\pi/4$ on each of them separately.

4.3.2. Effect of Dislocations Pile-up near the Surface

The dislocation structure underneath the surface and the distribution of the lateral stress σ_{xx} are plotted respectively in Figs. 4.6(a) and (b) for the case when the two slip planes are activated at the left corner of the asperity. Obviously, while the pro-load dislocations move away towards the bulk, anti-load dislocations dominate a thin layer underneath the free surface. This leads to the formation of a tensile layer underneath the surface as shown in Fig. 4.6(b). This tensile layer can cause surface cracking and sub-surface crack growth of thin-layer delamination [76].

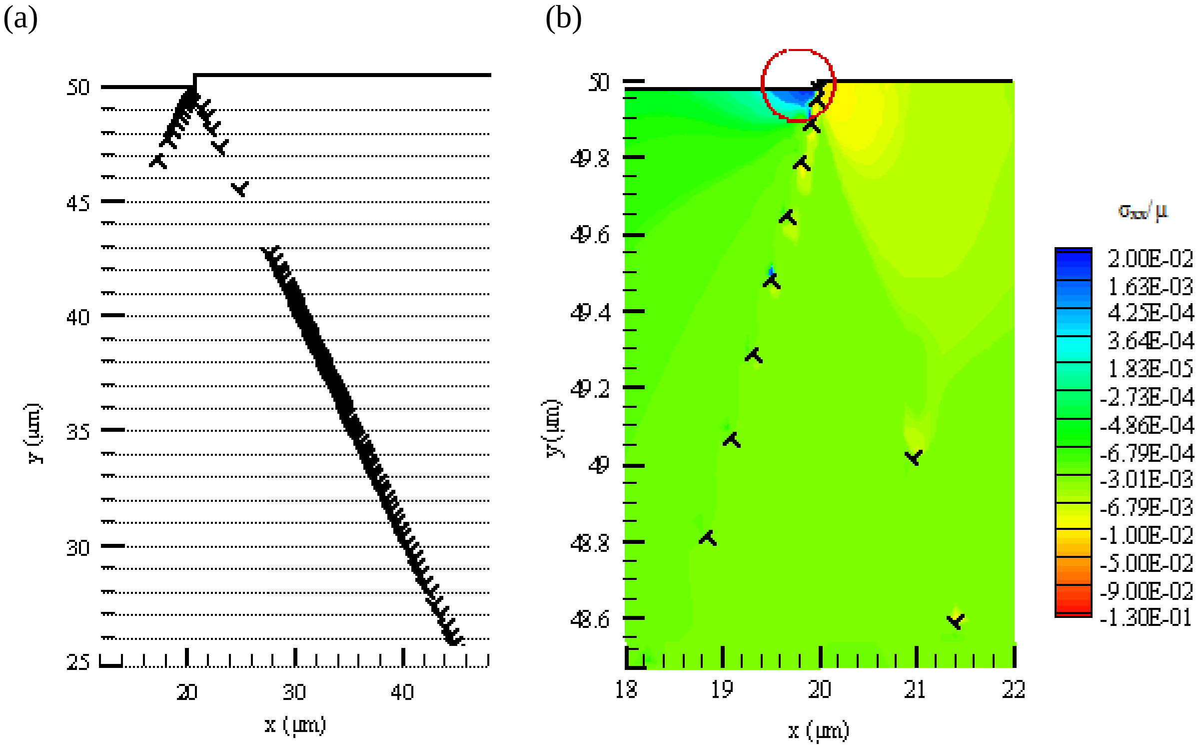

Figure 4.6. Simulation results for the isolated surface-step. (a) Dislocation structure; the height of the surface-step is magnified, (b) distribution of the lateral stress σ_{xx}.

4.3.3. Asperity Size Effect

The size effect on dislocation nucleation from surface-steps is checked by changing the width of the asperity *AS* and the width of the unit cell *w* while fixing the ratio of the asperity width to the unit cell width at *AS/w* = 1/9. As shown in Fig. 4.7, the mean contact pressure P_m required to nucleate dislocations from the surface-steps decreases as the size increases. Thus, it is difficult to flatten asperities as the size decreases. This confirms previous results obtained using discrete dislocation plasticity [40] and continuum plasticity [22,23] that nano-size asperities deform elastically.

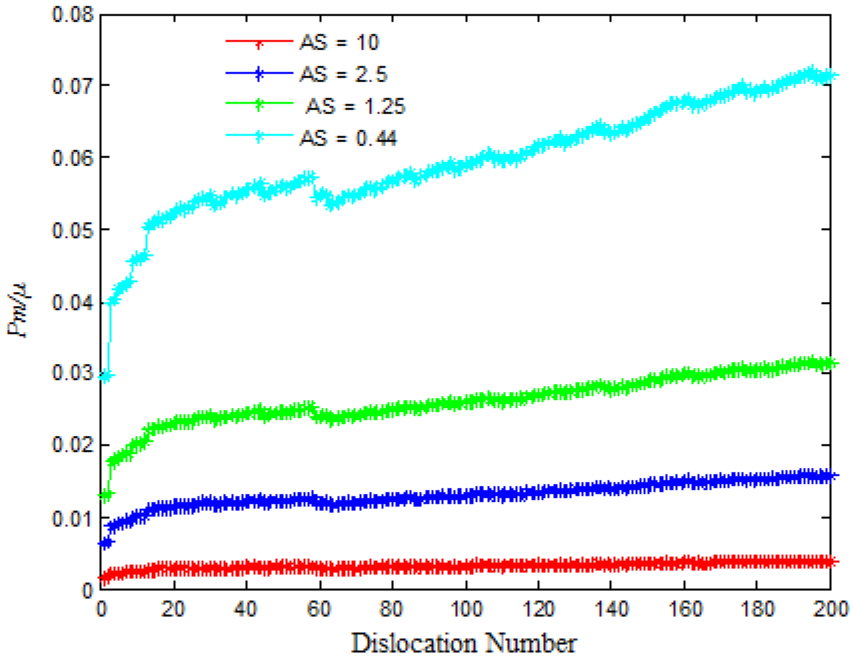

Figure 4.7. Effect of the asperity size on dislocation nucleation from surface-steps.

The dislocation segregation phenomenon observed in the case of isolated steps is investigated further for the case of asperities of finite sizes, i.e., a case where the surface-steps are close to each other. A unit cell model of width *w* = 50 µm and an asperity of size *AS* = 10 µm is considered. Dislocations network and distribution of the lateral stress σ_{xx} underneath the asperity are plotted respectively in Figs. 4.8(a) and (b). As shown in Fig. 4.8(a), anti-load dislocations pile up close to the asperity while pro-load dislocations move away towards the bulk of the material. The contour plot in Fig. 4.8(b) shows the development of high tensile spots at both corners of the asperity. Therefore, for asperities of large sizes, dislocations exhibit similar behavior as in the case of isolated surface-steps, that is, dislocations segregate into pro-load dislocations and anti-load dislocations.

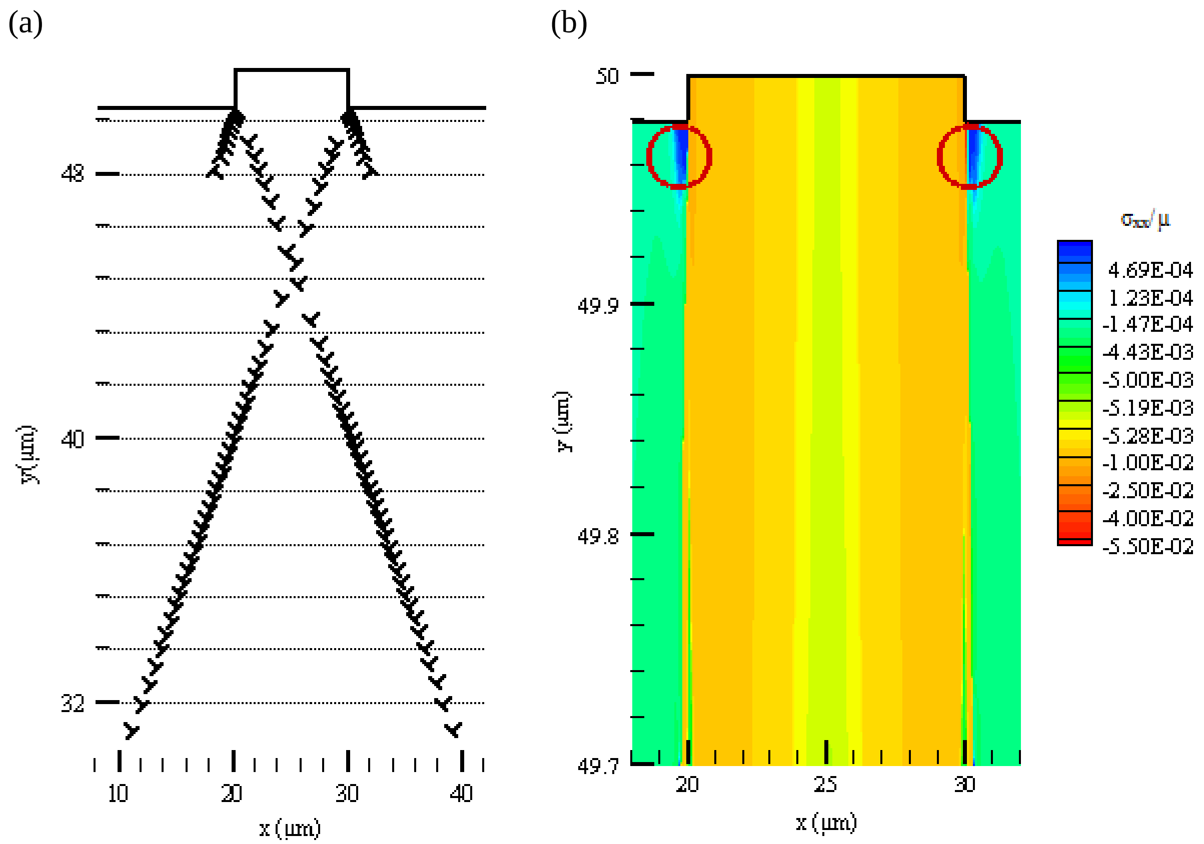

Figure 4.8. Simulation results for a unit cell of width *w* = 50 µm with an asperity of width *AS* = 10 µm. (a) Dislocation structure; the height of the asperity is magnified, (b) distribution of the lateral stress σ_{xx}.

To study the effect of the width of the asperity on the dislocation behavior, the width of the asperity is changed form 5 µm down to 0.44 µm. Snapshots of dislocation structure underneath the surface are plotted in Figs. 4.9(a-d) at the instant when 100 dislocations have been generated. As the size of the asperity decreases, the number of anti-load dislocations increases and the leading anti-load dislocation tailgate the leading pro-load dislocation. This can be explained as follows. The distance between the parallel slip planes emanated from the opposite corners of the asperity is proportional to the width of the asperity. Therefore, as the size of the asperity decreases, the back stress due to the pile-up of the anti-load dislocations underneath the surface is reduced by the compressive stresses generated by the pro-load dislocations nucleated at the opposite corner and; thus, nucleation of anti-load dislocations is facilitated. This is similar to the latent softening phenomenon discussed in Section 4.3.1, where slip planes emanated from isolated surface-steps facilitate nucleation of subsequent dislocations when both slip planes are activated. Furthermore, these pro-load dislocations form dipoles with anti-load dislocations nucleated from the opposite corner and move together towards the bulk. Therefore, we can differentiate between two phenomena: for asperities of large sizes, dislocations segregate into pro-load dislocations and anti-load dislocations, but as the size of the asperity decreases, dislocations generated along parallel slip planes form dislocation dipoles that glide away of the surface.

In Figs. 4.10(a-d), distribution of the lateral stress σ_{xx} underneath the asperity is plotted for the asperities of different widths. As shown, in Figs 4.10(a) and (b), asperities of large sizes develop high tensile spots at the corners of the asperities while the stresses under the free surface are compressive. This is due to the pile-up of the anti-load dislocations under the free surface as shown in Figs. 4.9(a) and (b). However, as the size of the asperity decreases, these tensile spots vanish and the stress in the vicinity of the asperities is compressive (Figs. 4.10(c) and (d)). Furthermore, for the asperities of small sizes, high compressive stresses are developed inside shear bands that emanate from the surface. These shear bands are due to the dipolar bands that are formed by the anti-load and pro-load dislocations nucleated from the opposite corners of the asperity. Thus, materials are pushed from the surface towards the bulk within those shear bands leading to the high compressive stresses.

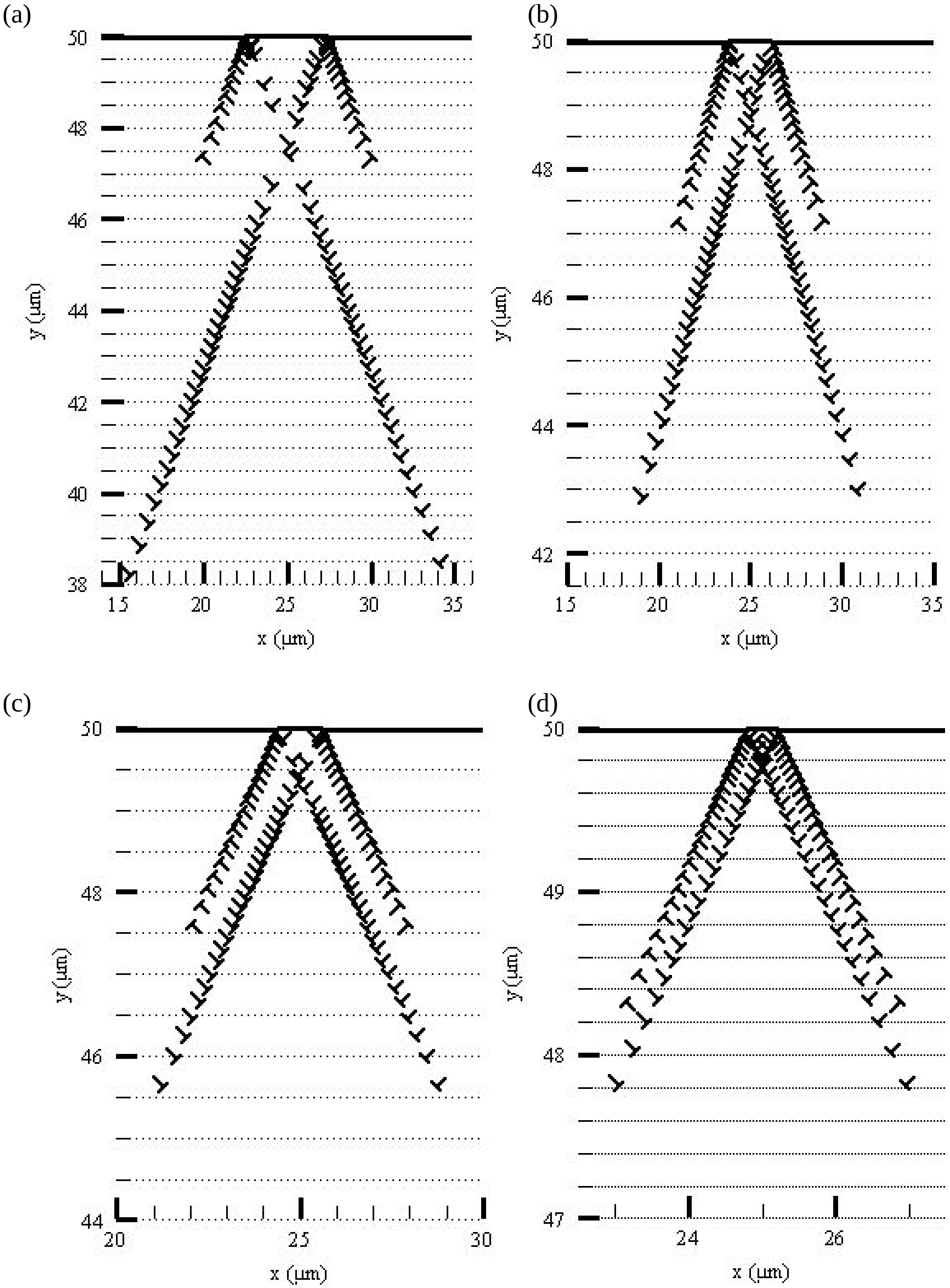

Figure 4.9. Dislocation structure under the indented surface for asperities of different widths: (a) *AS* = 10 µm, (b) *AS* = 5 µm, (c) *AS* = 2.5 µm and (d) *AS* = 0.44 µm. The heights of the asperities are magnified.

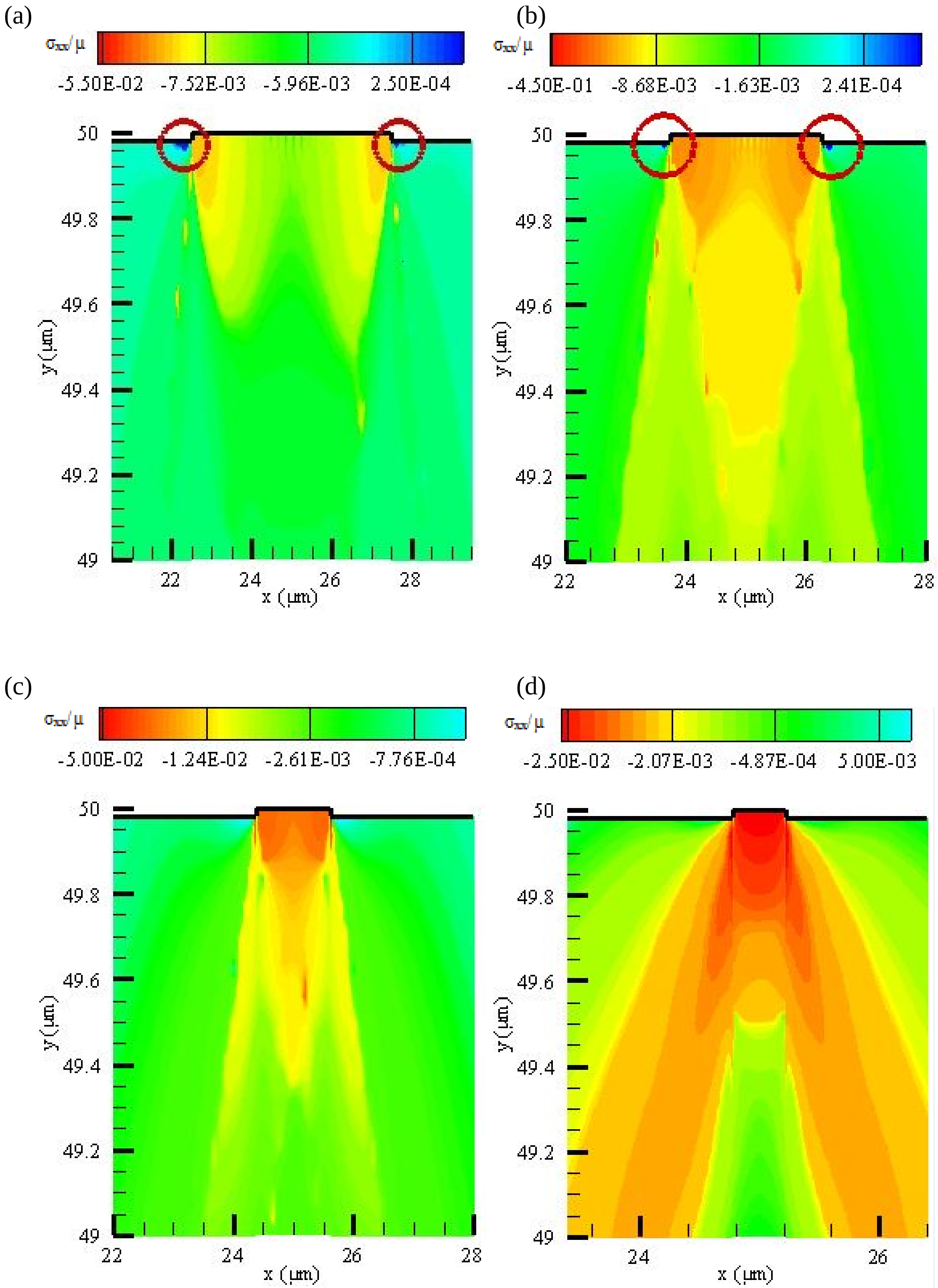

Figure 4.10. Distribution of the lateral stress σ_{xx} underneath the contact area for: (a) *AS* = 5 μm, (b) *AS* = 2.5 μm, (c) *AS* = 1.25 μm and (d) *AS* = 0.44 μm.

4.3.4. Asperity Spacing Effect

The mean contact pressure, P_m, required to nucleate the first dislocation from the surface step is plotted against the unit cell width in Fig. 4.11. Two effects have been observed. First, for widely spaced asperities, the slip planes at $\theta = -3\pi/4$ yield before the slip planes at $\theta = -\pi/4$ but as the asperities become closer, the yielding order flips. Second, the mean pressure required to yield the slip plane at $\theta = -3\pi/4$ is inversely proportional to the asperity spacing while the mean pressure required to yield the slip plane at $\theta = -\pi/4$ is proportional to the asperity spacing. In Fig. 4.12, the mean contact pressure is plotted against the number of dislocations for several unit cells with widths that vary from $w = 6$ µm to $w = 2$ µm. For the unit cells of width: $w = 2$ µm, $w = 3$ µm and $w = 4$ µm, it is easier to nucleate the first few pro-load dislocations than the anti-load dislocations. However, nucleation of subsequent pro-load dislocations requires considerable increase in the mean contact pressure and this is presented by the jumps in the mean contact pressure curves that correspond to the cases $w = 2$ µm, $w = 3$ µm and $w = 4$ µm. This hardening behavior is due to the interaction among the pro-load dislocations nucleated from adjacent asperities. In contrast, for the widely spaced asperities case, $w = 6$ µm, where it is easier to nucleate the first anti-load dislocation, subsequent dislocations are nucleated without a significant increase in the mean pressure. This is due to the latent softening phenomenon discussed above. We conclude that when the asperities become closer to each other, it becomes easier to flatten asperities of moderate heights but very difficult to flatten asperities of large heights.

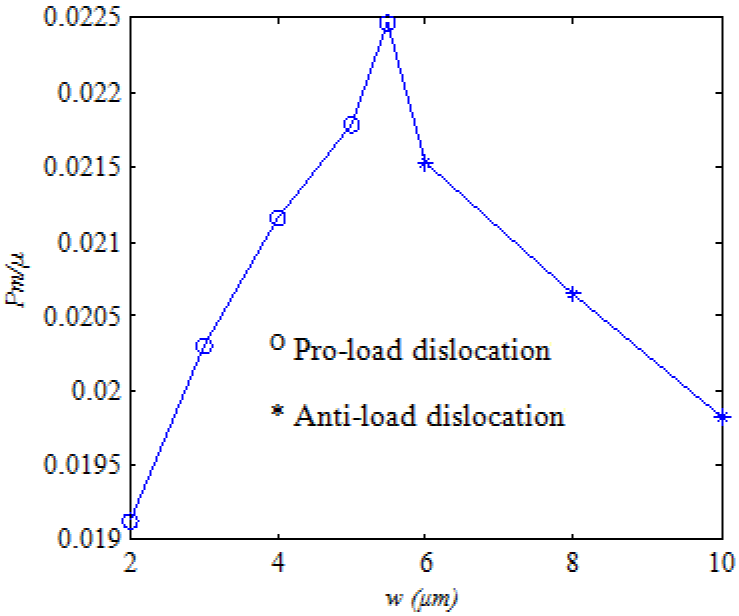

Figure 4.11. Mean contact pressure required to nucleate the first dislocation from the asperity corner versus the width of the unit cell, *w*.

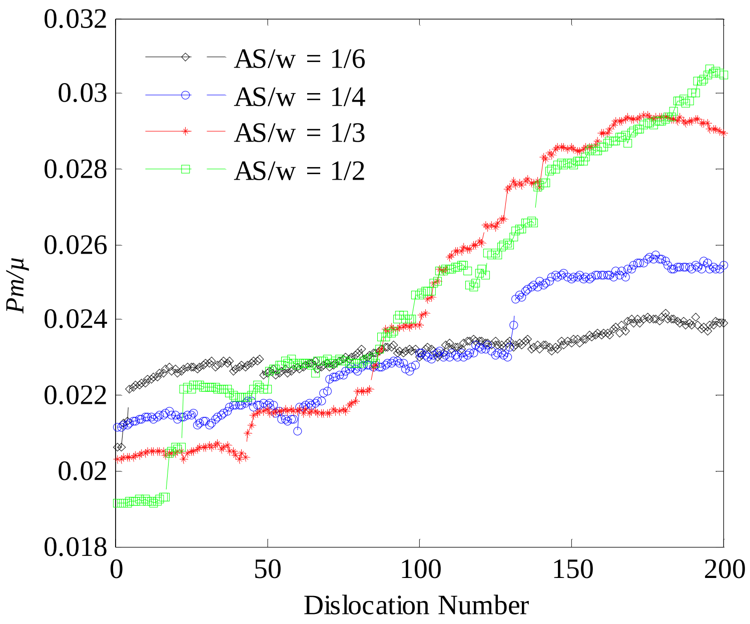

Figure 4.12. Mean contact pressure versus the number of dislocations for cases of same asperity size AS = 1μm and several unit cell widths.

4.3.5. Ratio Effect

As discussed above, dislocation nucleation from surface-steps and dislocation behavior underneath the contact area are controlled by two phenomena. These phenomena are latent softening and neighboring hardening, where the former depends on the size of the asperity and the latter depends on the asperity spacing. In this section, we investigate the competition between the two phenomena.

Consider an asperity of size *AS* = 0.44 µm and two unit cell of widths *w* = 4 µm (*AS/w* = 1/9) and *w* = 2 µm (*AS/w* = 2/9). Dislocation structures are plotted respectively in Figs. 4.13(a) and 4.13(b). Dipolar bands are observed in both figures. This is because the asperity spacing I slarge enough and the asperity width is small so the latent softening phenomenon prevails.

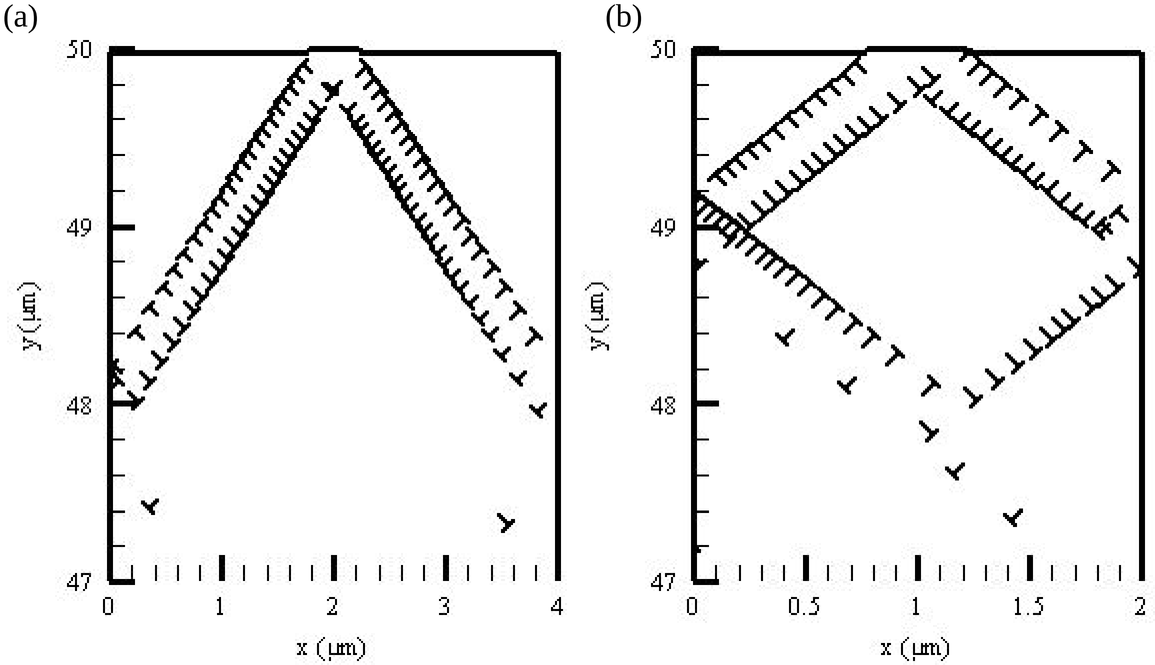

Figure 4.13. Dislocation structure underneath the surface for an asperity of size *AS* = 0.44 µm and width to spacing ratio: (a) *AS/w* = 1/9, (b) *AS/w* = 2/9.

Now, let's change the size of the asperity to AS = 1 µm. Dislocation structures are plotted respectively in Fig. 4.14(a) and (b) for the two unit cells of widths w = 4 µm and w = 2 µm. Dipolar bands are observed only for the unit cell of width w = 4 µm and AS/w =1/4. This is because the dipole strength is inversely proportional to the distance between the slip planes and as the size of the asperity increases, this distance increases and therefore dipoles become weaker and cannot overcome the neighboring hardening effect. Thus, the neighboring hardening phenomenon prevails when the asperity spacing approaches the width of the asperity.

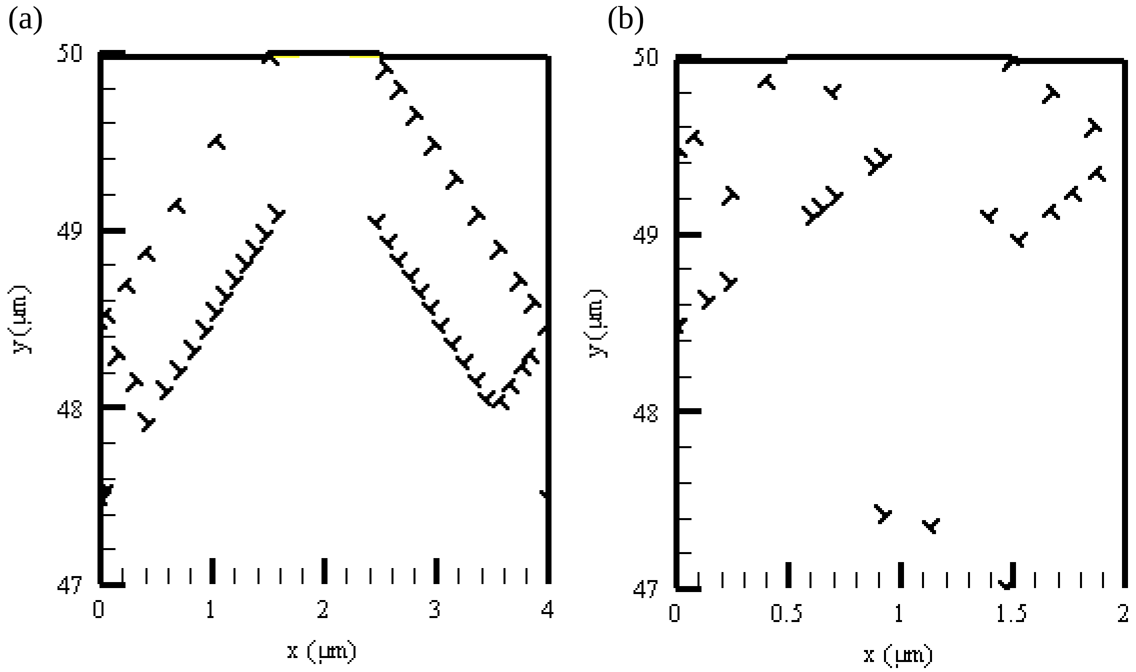

Figure 4.14. Dislocation structure underneath the surface for an asperity of size AS = 1 µm and width to spacing ratio: (a) AS/w = 1, (b) AS/w = 1/2.

Therefore, the ratio of the size of the asperity to the distance between adjacent asperities is very crucial in determining the dislocation behavior underneath the surface. Thus, we conclude that dislocation behavior is determined by two out of the following three factors: width of the asperity (*AS*), width of the unit cell (*w*), and ratio of the width of the unit cell to the width of the asperity (*AS/w*).

4.4. Further Remarks on the Model

First, dislocation nucleation from surface-steps is assessed by the Rice-Thomson criterion which is based on the stress state at the stress concentration. Once the Peach-Koehler force on a fictional dislocation at a distance η from the surface step exceeds the Peierls stress, the dislocation is nucleated. Thus, the model critically depends on the stress state at the surface-steps which can suddenly change once a new dislocation is born. Thus, slip plane instability is not taken into consideration before the dislocation is nucleated. Furthermore, the Rice-Thomson model does not consider the three-dimensional nature of embryo dislocation [52]. The observed latent softening phenomenon critically depends on the nucleation model adopted and therefore this scenario may change if a different nucleation criterion is adopted .To the knowledge of the authors, there is no consensus on the dislocation nucleation from the surface in the literature. However, a continuum cohesive zone model can be employed to capture more details of the dislocation nucleation process [77].

Second, dislocations segregation is due to the remote applied load. Therefore, changing the dislocation nucleation criterion is not expected to change this scenario. However, in this chapter only nucleation from surface-steps is allowed and thus by considering bulk yield some of the phenomena discussed in this chapter may not hold.

4.5. Conclusion

A Multi-Asperities model has been introduced to study dislocation behavior near rough surfaces under contact loading. Periodic boundary conditions are adopted to take into consideration the effect of adjacent asperities. Simulations were carried out using the new boundary element approach presented in Chapter 3.

The main conclusions are:

- The size effect is clear in the simulation results; the smaller being the harder. Moreover, dislocations nucleated under the indented asperities spread out to reach neighboring asperities and interact with the dislocations nucleated from neighboring asperities. This observation contradicts the continuum plasticity results that plastic deformation is confined to the area under the asperities that have yielded.
- For the case of asperities of large sizes, dislocations segregate into pro-load type and anti-load type near the surface. Pile-up of the anti-load dislocations underneath the contact area results in the development of high tensile spots at the asperities edges.
- For the case of widely spaced and relatively small asperities, dislocations nucleated from opposite corners of an asperity form dipolar bands that propagate towards the material bulk. These dipolar bands accommodate high compressive stresses. Surface Materials are squeezed within these shear bands.

CHAPTER 5

EFFECT OF BULK YIELD ON SURFACE MICROPLATICITY

5.1. Introduction

In Chapter 4, discrete dislocation analysis of rough surfaces under contact loading is conducted. We assumed that the material bulk is free of defects where plastic deformation is due to the homogenous nucleation of dislocations from surface-steps. Given that the size of the asperity is big enough, high tensile spots were observed at the edges of the asperity; this is due mainly to the pile up of the anti-load dislocations underneath the free surface. These tensile high spots may lead to surface crack nucleation associated with delamination wear. Rough surfaces with asperities of small widths and that are spaced widely enough exhibit shear band deformation that emanates from the asperity and propagates toward the bulk. Similar deformation pattern was observed in an impact experiment on an MgO single crystal (see Fig. 5.1) [48].

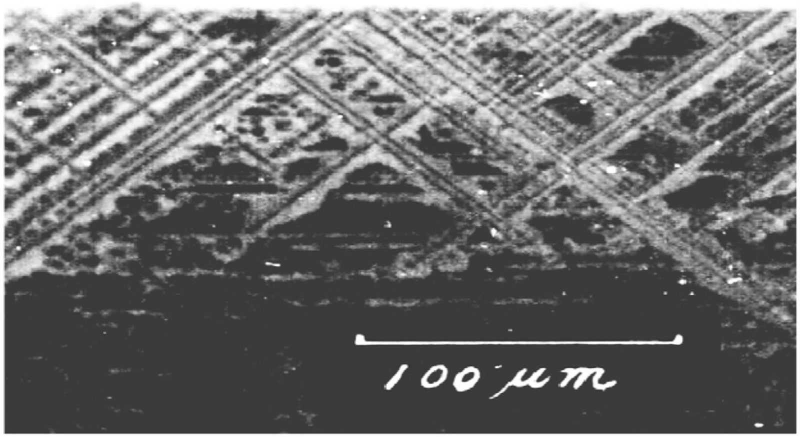

Figure 5.1. Dislocation etch pits of bands emanating from surface asperities of an MgO single crystal under contact [48].

5.2. Boundary Value Problem

In this chapter, discrete dislocation calculations are carried out for the Multi-Asperities model under contact loading taking into consideration the yield of bulk material. Thus bulk sources such as Frank-Read sources are introduced. Here, we study the effect of dislocations nucleated from bulk sources on dislocation structure and stress distribution underneath the contact area for asperities of different sizes and different spacing. Frank-Read sources are distributed randomly along predefined slip planes with orientations: $\theta = -\pi/4$, $-3\pi/4$ and 0 rad (Fig. 5.2). Dislocation nucleation from Frank-Read sources is modeled through the constitutive rule discussed in Section 3.4. If two dislocations of opposite Burgers vectors get closer than $6b$ to each other, they are annihilated and taken out of the simulations. Unless noted otherwise, the density of the Frank-Read sources is fixed to be $\rho_{src} = 30\ \mu\text{m}^{-2}$. The strength of Frank-Read sources and the nucleation time are fixed to be respectively $\tau_{nu} = 183$ MPa and $t_{nu} = 10$ ns. Distance between slip planes is fixed to be $200b$. The time step is fixed as $\Delta t = 0.05$ ns, which is small enough compared to the nucleation time to make sure that nucleation events are not missed. Similar to Chapter 4, the Rice-Thomson model is used to assess nucleation of dislocations from surface-steps, i.e., from opposite corners of an asperity. The formulations derived in Chapters 2 and 3 assume small strain deformations; therefore, evolution of the surface roughness due to dislocation annihilation at the surface or dislocation nucleation from surface-steps is not considered. Moreover, surface evolution requires re-meshing of the boundary where very small elements have to be structured around the newly created surface-steps that are of small heights which make the problem computationally very expensive. Therefore, dislocations nucleated from bulk sources that glide towards the free surface are annihilated and taken out of the simulations. However, bulk dislocations that reach the contact area are pinned at a distance of $5b$ from the area under contact. The single crystal is taken to be elastically isotropic, with a shear modulus μ = 183 GPa and a Poisson ratio v = 0.43. A Burgers vector of magnitude b = 0.4 nm is used in the calculations.

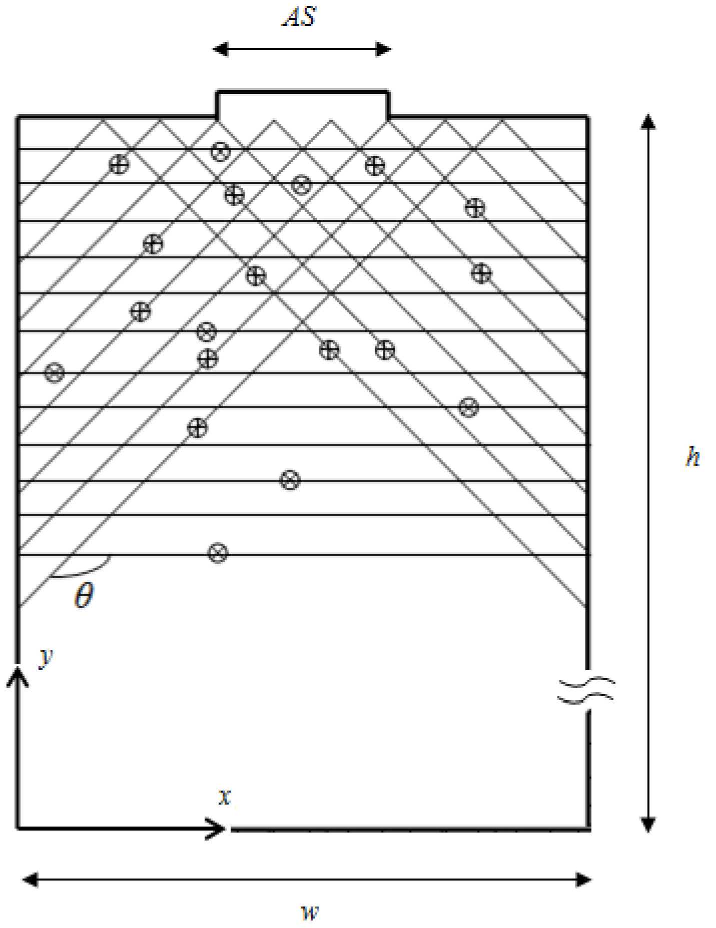

Figure 5.2. Unit cell model with Frank-Read sources distributed along slip planes inclined at an angle θ form the x axis.

As in Chapter 4, a displacement controlled loading with an indentation rate $\dot{u} = 4 \times 10^4\ \mu m/s$ is applied along the width of the asperity, *AS*, where frictionless conditions are assumed. The effect of neighboring asperities is taken into consideration by applying periodic boundary conditions along the opposite sides of the unit cell. See Eqs. (4.1-7) for a detailed description of the boundary conditions.

5.3. Simulation Results

Discrete dislocation simulations are carried out first for a planar-symmetric single crystal with slip systems oriented at angles $\theta = -\pi/4$ and $\theta = -3\pi/4$ from the x axis. Then a slip system parallel to the x axis is added.

5.3.1. A Crystal with Two Slip Systems

In this section, deformation pattern is investigated for the case when bulk sources are present. To establish a connection with the results in Chapter 4, a unit cell with geometric properties ($w = 4$ µm and $AS = 0.44$ µm) is simulated with and without bulk sources. For the case where bulk sources are present, Frank-Read sources are distributed randomly along the slip planes at $\theta = -\pi/4$ and $\theta = -3\pi/4$. In Fig. 5.3, contour plots of the lateral stress σ_{xx} is plotted along with the dislocation structure for the two cases at an indentation depth $u = 0.062$ µm. For the case where nucleation is allowed only from surface-steps (Fig. 5.3(a)), two dipolar bands that accommodate high compressive stresses emanate from the asperity corners. Similarly, for the case where bulk sources are activated (Fig. 5.3(b)), two shear bands still emanate from the asperity. These shear bands are populated with dislocations that are nucleated from bulk sources and glide on slip planes perpendicular to the shear bands. These dislocations glide towards the free surface and change the surface profile. It is worth noting that when bulk sources are activated, there are tensile layers under the free surface which are partially due to the elastic deformation. However, when only surface sources are activated, stresses under the free surface are predominately compressive.

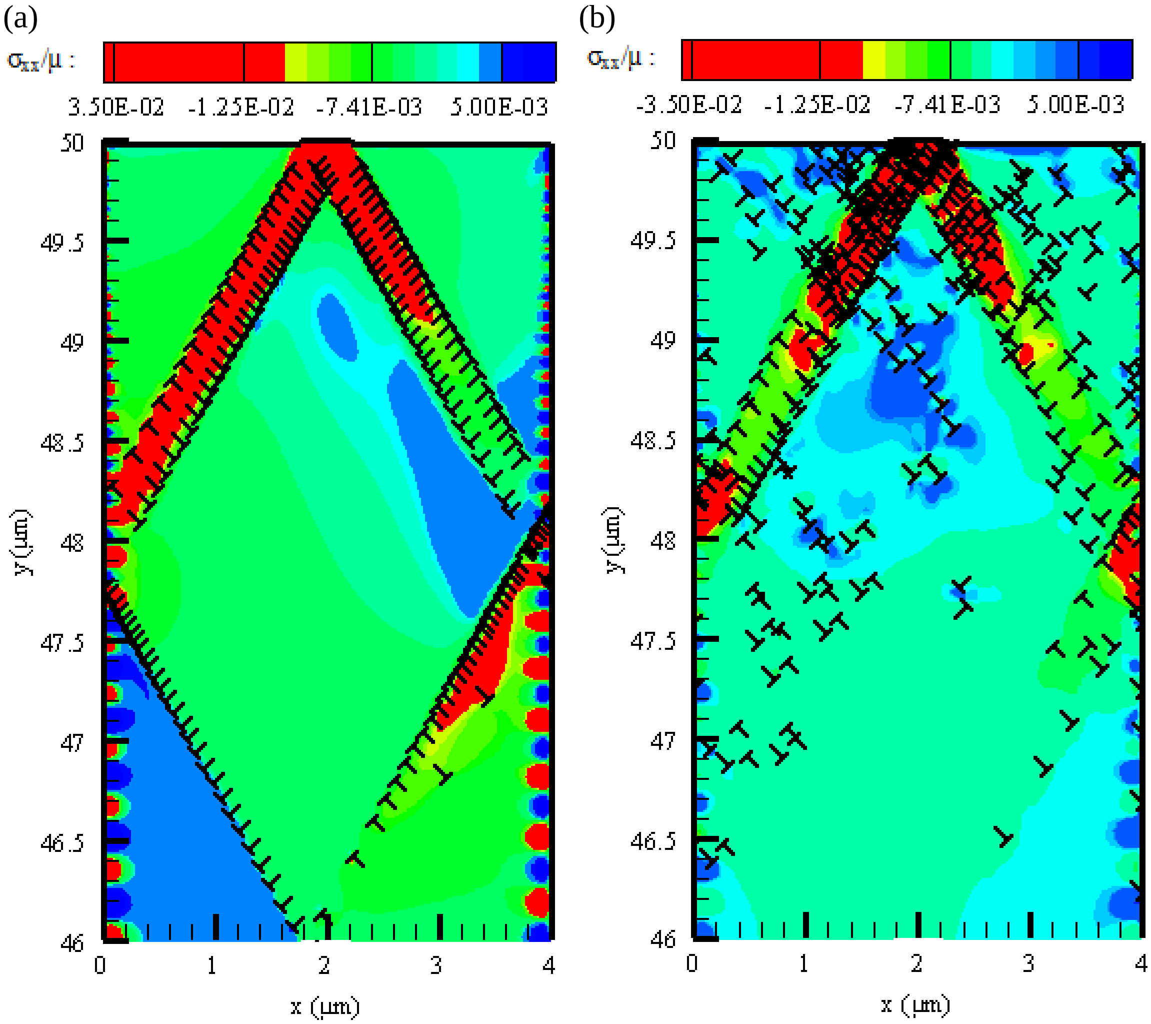

Figure 5.3. Distribution of the lateral stress σ_{xx} and dislocation structure at the indentation depth (u = 0.062 µm) for the case (w = 4 µm and AS = 0.44 µm) where nucleation is allowed from: (a) only corners of the asperity, (b) both Frank-Read sources and corners of the asperity.

Let's now look at the case of closely spaced asperities (w = 2 µm and AS = 0.44 µm). Simulation results at u = 0.1 µm in Figs. 5.4(a) and (b) reveal two shear bands emanated from the surface, whether bulk sources are activated or not. However, in the case where bulk sources are activated, well structured dipolar bands are not observed. This is again due to dislocations nucleated from Frand-Read sources that glide towards the free surface in the vicinity of the asperity and block the dislocations nucleated from the corners of the asperity.

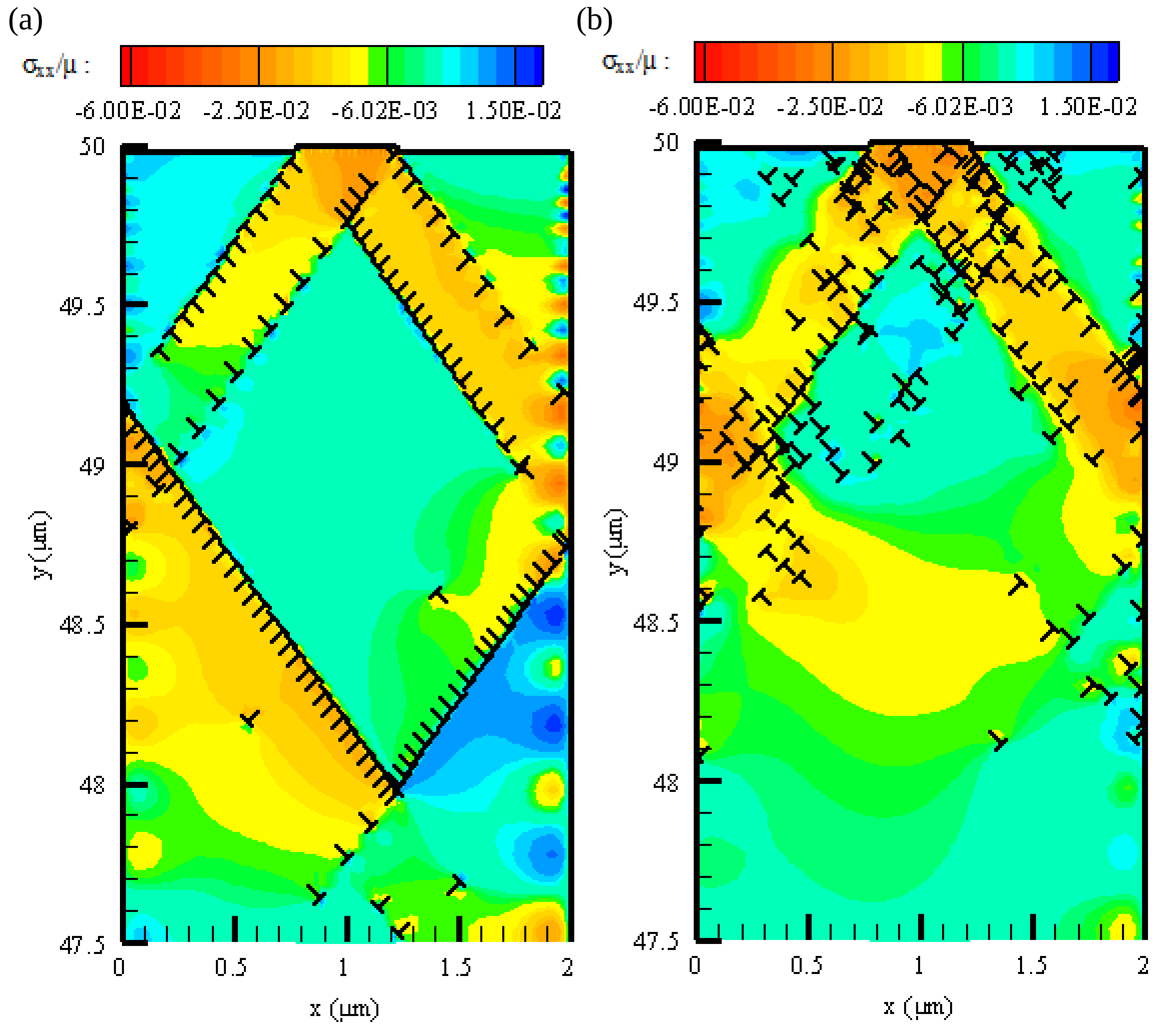

Figure 5.4. Distribution of the lateral stress σ_{xx} and dislocation structure at the indentation depth (u = 0.1 µm) for the case (w = 2 µm and AS = 0.44 µm) where nucleation is allowed from, (a) only corners of the asperity, (b) both Frank-Read sources and corners of the asperity.

One common observation between the widely closed asperities and the closely spaced asperities is that the zone under the contact area is populated by both anti-load and pro-load dislocations, which explains why tensile spots at the edges of the asperities are not observed whether dipolar bands are formed or not. It is important to mention that the compressive stresses in the shear bands are more significant in the case when only surface sources are activated.

The results presented above are at a moderate indentation depth where only very few Frank-Read sources near the contact area are activated. In the rest of this section, results are presented at the indentation depth u = 0.16 µm, which is large enough so that Frank-Read sources away from the surface are activated and therefore bulk yield occurs. Contour plots of the lateral stresses σ_{xx} for the two unit cells (AS/w = 0.44/2) and (AS/w = 0.44/4) at an indentation depth u = 0.16 µm are plotted in Fig. 5.5. At this indentation depth, the shear bands are still observed for both of the unit cells. However, the shear bands in the case of widely spaced asperity (w = 4 µm) are more considerable and propagate deep in the bulk in contrast to the closely spaced asperity (w = 2 µm) where the shear bands stay closer to the surface. This is because for closely spaced asperities, shear bands emanated from the surface asperity are blocked by the shear bands emanated from neighboring asperities.

We also looked at the effect of the ratio of the asperity width to the unit cell width AS/w. For the unit cell of width w = 4 µm, the ratio is varied from 1/9 to 1/3. Contour plot of the lateral stress in Fig. 5.5(c) shows that for the high ratio, 1/3, two shear bands still emanate from the surface asperity and propagate towards the bulk. However, compressive stresses within the band-like regions are less significant than in the case of the small contact to space ratio, AS/w = 1/9.

We conclude that for a crystal with two symmetric slip planes at $\theta = -\pi/4$ and $-3\pi/4$, shear bands emanate from the asperity under contact loading and propagate towards the material bulk regardless of the yield condition of the bulk material. These shear bands accommodate large compressive stresses due to the material insertions in these band-like regions. However, as the size of the asperity approaches the distance between neighboring asperities, these shear bands become less prominent and deformation is more like that of plain strain compression. Similar behavior was observed in Chapter 4 when only surface sources are activated.

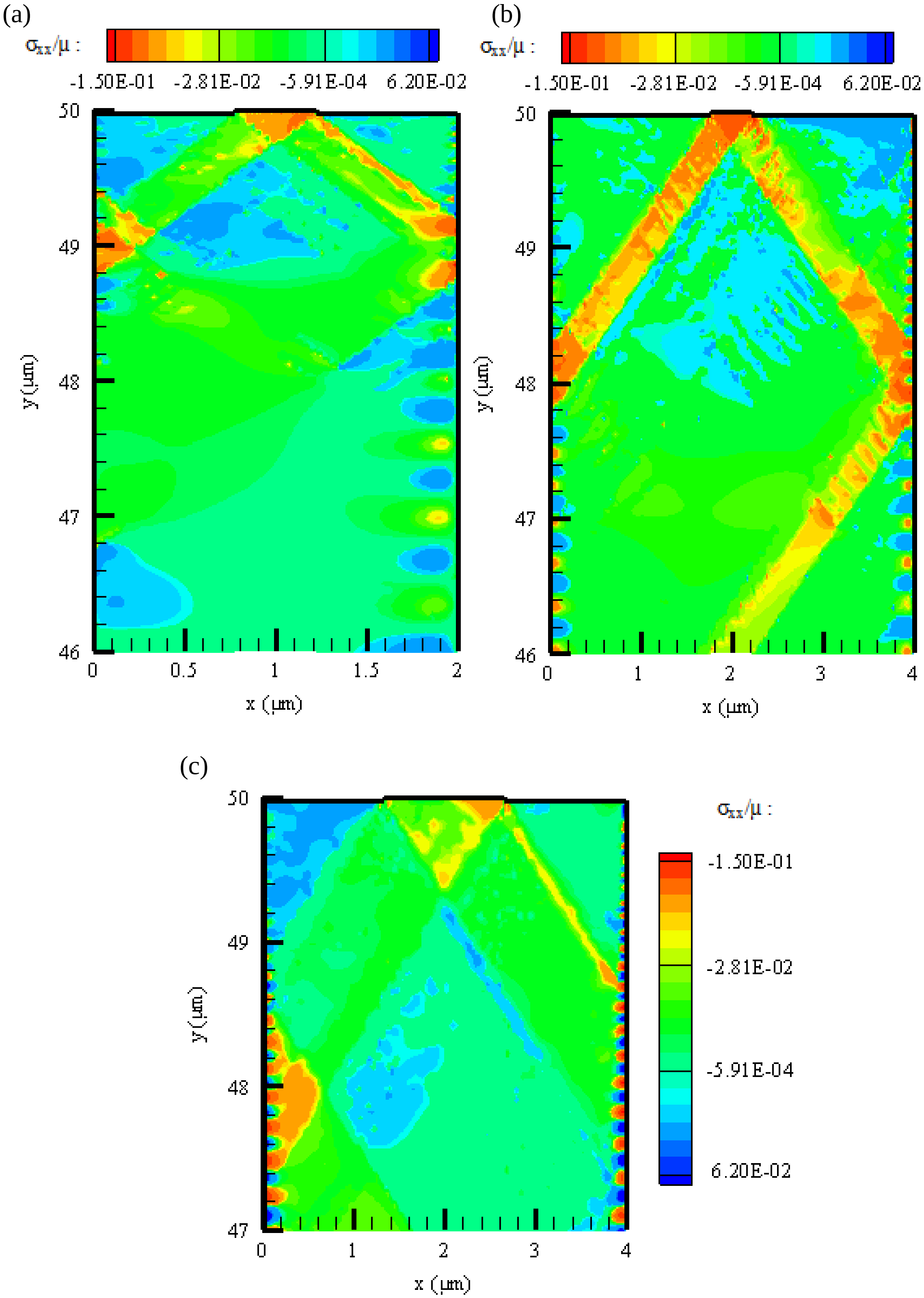

Figure 5.5. Distribution of the lateral stress σ_{xx} at the indentation depth (u = 0.16 μm) for the cases: (a) *AS/w* = 0.44/2, (b) *AS/w* = 0.44/4, and (c) *AS/w* = 1.33/4.

5.3.2. A Crystal with Three Slip Systems

5.3.2.1. Deformation Pattern

Here, we study dislocation interaction and deformation pattern when all of the three slip systems are active. Frank-Read sources are now distributed along the three slip systems: $\theta = -\pi/4$, $-3\pi/4$ and 0 rad. We conduct a series of simulations for a unit cell of width $w = 8$ µm with a surface asperity of different sizes. The size of the asperity is ranging from $AS = 0.44$ µm to $AS = 4$ µm.

Let's look first at the case of an asperity of size $AS = 0.44$ µm, $AS/w = 1/18$. In Fig. 5.6(a), dislocation structure down to a distance of 3 µm from the surface is shown. Arrays of dislocations with negative Burgers vector pile up in the central region on parallel slip planes down to a distance of 1 µm from the surface. The lengths of these arrays range from 0.44 µm to 1.2 µm. On both sides of these arrays, there are arrays of dislocations with positive Burgers vector. These arrays of dislocations play the role of obstacles to the dislocations nucleated in the bulk and glide towards the surface, which may explain why the zone underneath the surface is not densely populated with dislocations.

From the above observations, we conclude that just under the asperity, materials are pushed downward, i.e., sink in, while at the opposite sides of the asperity, materials pile up. If we define the amount of material pile-up as the difference between the indentation depth and the maximum displacement along the surface, we find that the amount of pile up is 0.118 µm. Dislocations nucleated along the inclined slip planes either move towards the bulk or form slip bands that propagate towards the surface and can change the surface roughness. A close snapshot of the dislocation structure within a zone of size 0.1 µm underneath the asperity (Fig. 5,6(b)) shows the existence of both anti-load and pro-load dislocations underneath the asperity. However, the number of anti-load dislocations is almost double the number of pro-load dislocations.

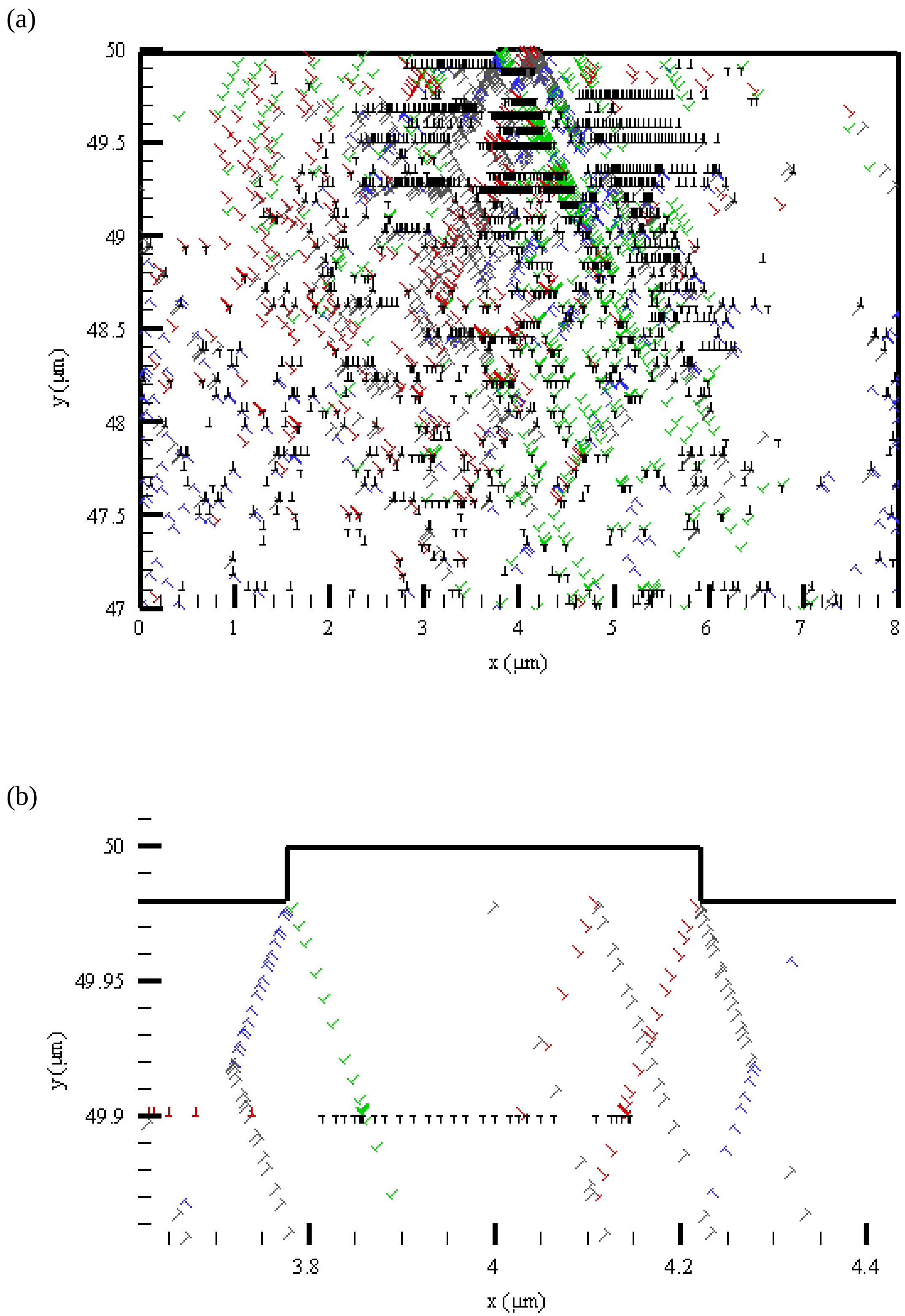

Figure 5.6. (a) Dislocation structure underneath the indented surface for the case *AS/w* = 0.44/8. (b) Snapshot of the dislocation structure underneath the asperity.

The size of the asperity is changed to *AS* = 0.88 µm while the unit cell width is kept fixed to *w* = 8 µm. Dislocation structure to a distance of 3 µm from the surface is plotted in Fig. 5.7(a). Similar to the case above (*AS/w* = 0.44/8), we still observe arrays of dislocations with horizontal Burgers vector along parallel slip planes. However, these arrays are less populated with dislocations and more spread out than in the previous case (*AS/w* = 0.44/8). Moreover, there are on both sides of the asperity slip bands that intersect the free surface. This leads to the formation of surface-steps and therefore changes the morphology of the surface. The number and length of these slip bands are more significant than in the case where *AS/w* = 1/18. A close inspection of the dislocation structure underneath the asperity (Fig. 5.7(b)) shows that the so called anti-load and pro-load dislocations nucleated from the asperity corners exhibit similar behavior as in the case discussed above (*AS/w* = 0.44/8). However, the area between the corners of the asperity is populated with parallel arrays of dislocations propagating from the bulk material and piling up underneath the contact which may cause some hardening behavior.

Now let’s look at the case where the distance between adjacent asperities is equal to the size of the asperity, i.e., *AS/w* = 4/8. From Fig. 5.8, we observe that dislocations are more spread out throughout the width of the unit cell. Compared to the widely spaced case (*AS/w* = 0.44/8), we notice two main differences. First, we do not observe parallel arrays of pile-up dislocations in the central zone and this can be due to the big size of the loaded zone which makes it easier for dislocations along parallel slip planes to form dipoles and move together. The height of the pile-up material is equal to 0.0568 µm, almost half of the height of the material pile-up for the case of *AS/w* = 0.44/8. Second, the zone under the asperity is densely populated with dislocations gliding form the bulk towards the contact area. This contributes partially to the difference between the size of the pile-up of widely spaced asperity and closely spaced asperity.

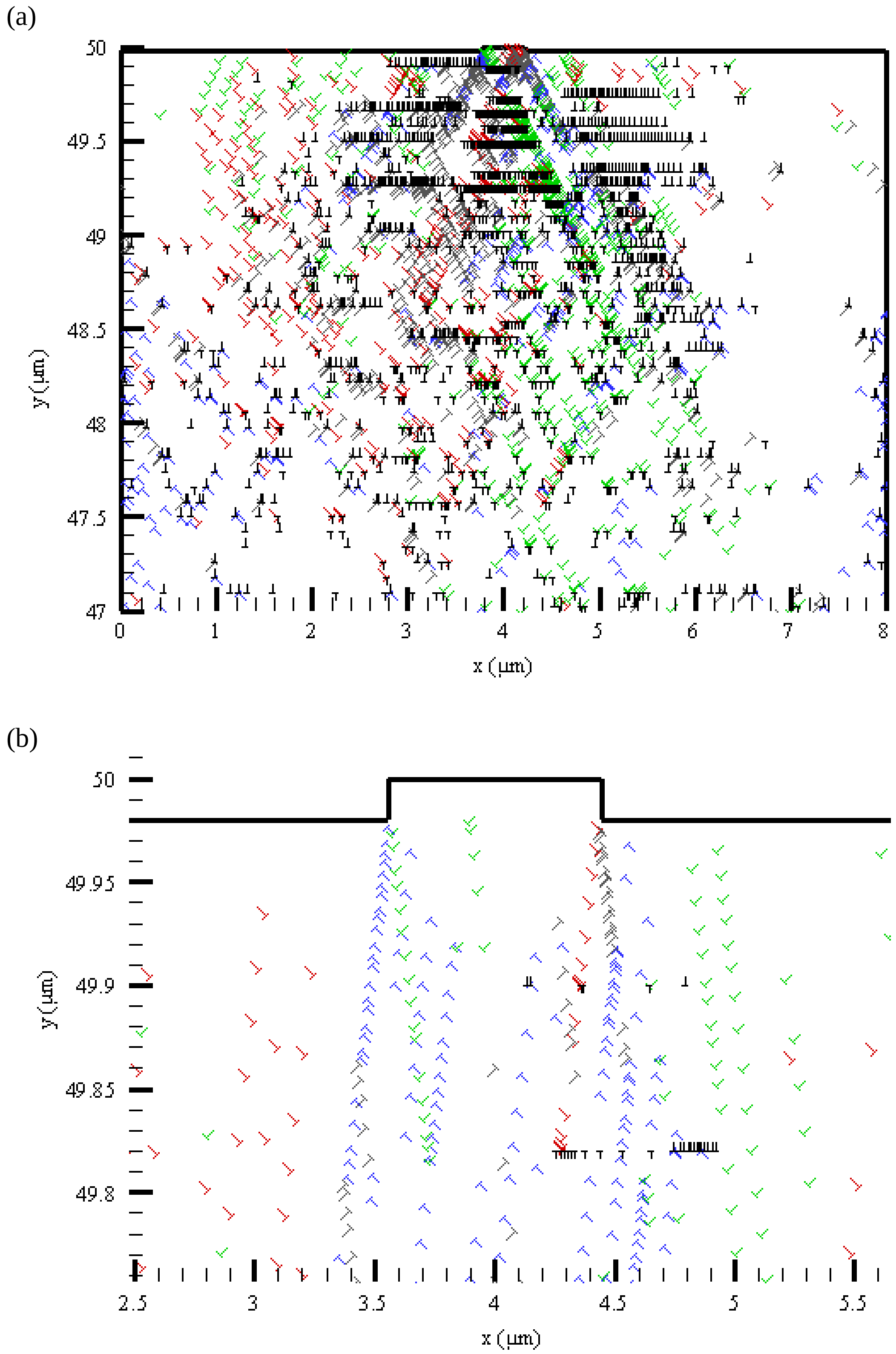

Figure 5.7. (a) Dislocation structure underneath the indented surface for the case *AS*/*w* = 0.88/8. (b) Snapshot of the dislocation structure underneath the asperity.

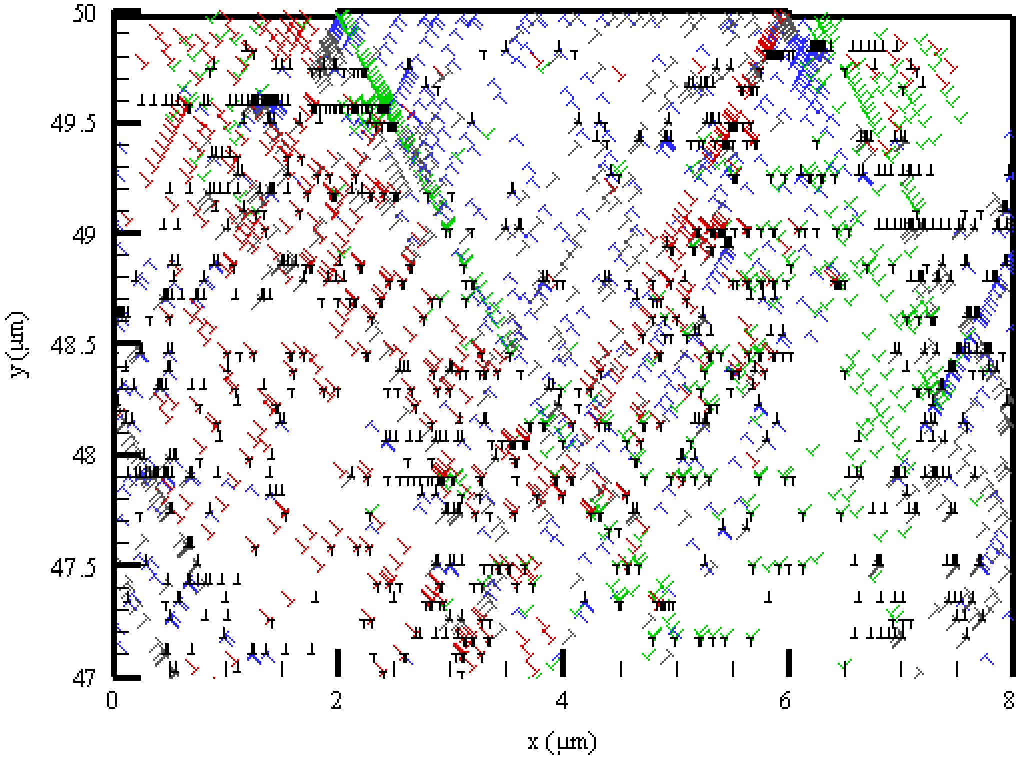

Figure 5.8. Dislocation structure underneath the indented surface for the case *AS/w* = 4/8.

5.3.2.2. Internal Stress

In this section, distribution of the lateral stresses σ_{xx} is analyzed and its connection to the asperity size and spacing is investigated. To establish a connection between dislocation structure and stress distribution, contour plots of the lateral stress is plotted for the unit cell of width *w* = 8 µm with an asperity of size *AS* = 0.44 µm. Fig. 5.9(a) shows a compressive zone that spans the width of the unit cell; however, in the central zone underneath the asperity there are high compressive stresses followed by tensile spots. These tensile spots correspond to the arrays of dislocations that pile-up in the central zone underneath the contact. The period of the surface roughness is changed now to *w* = 4 µm. In Fig. 5.9(b), a contour plot of the lateral stress σ_{xx} under the indented surface is shown. In contrast to the previous case (*w* = 8, *AS* = 0.44), compressive shear stresses are more concentrated in a shear band that emanates from the surface while the tensile spots are distributed throughout the width of the cell down to a distance of 2 µm from the surface.

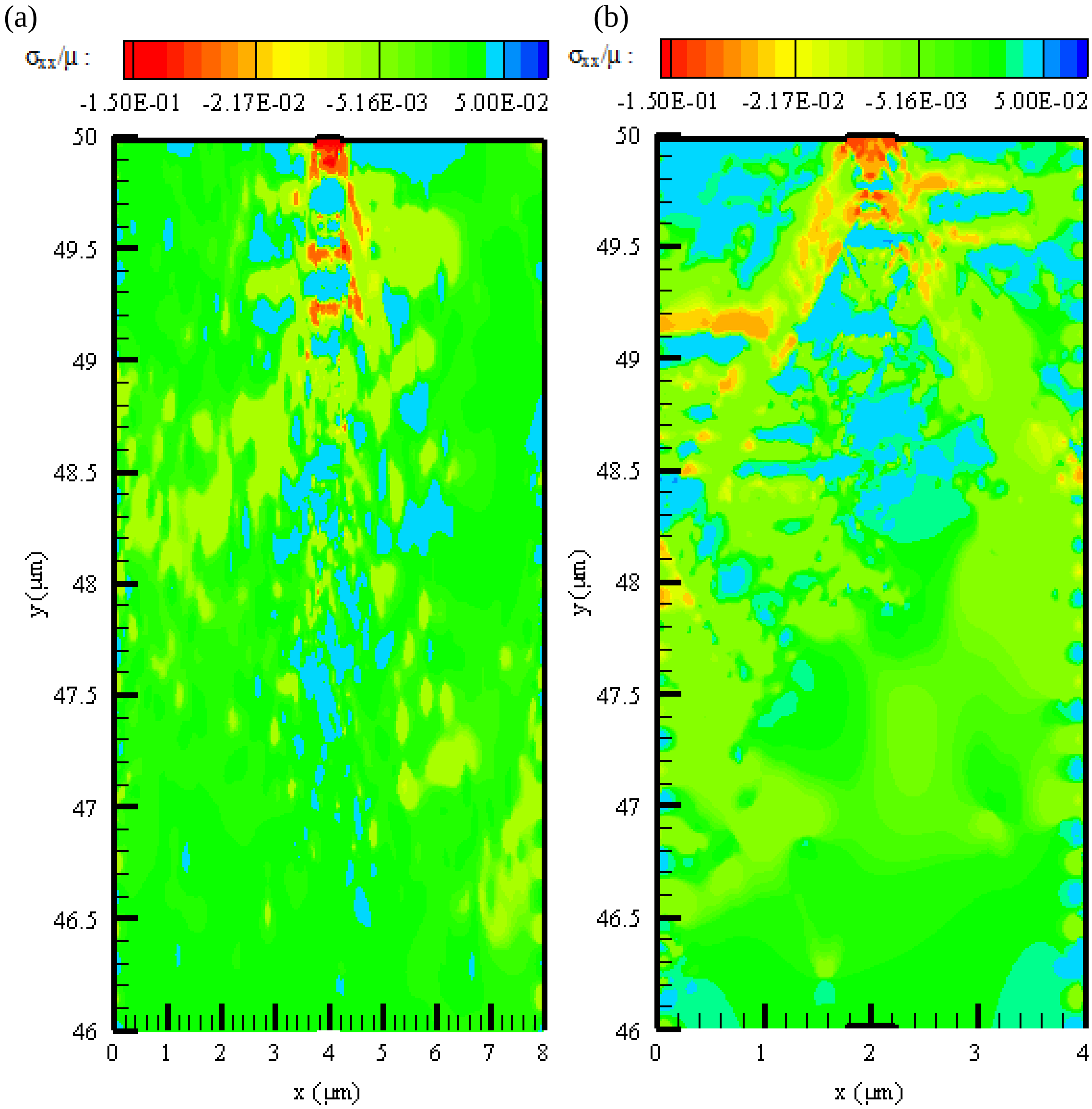

Figure 5.9. Distribution of the lateral stress at the indentation depth (u = 0.16 µm) for the cases: (a) AS/w = 0.44/8, and (b) AS/w = 0.44/4.

The unit cell width is changed now to $w = 2$ µm while the asperity size is still set to $AS = 0.44$ µm. Contour plot of the lateral stress, plotted in Fig. 5.10, shows islands of compressive and tensile stresses down to a distance of 1 µm from the surface below which the stresses are predominately compressive. It is worth noting that in all of the cases presented, there are no tensile spots in the vicinity of the asperity corners.

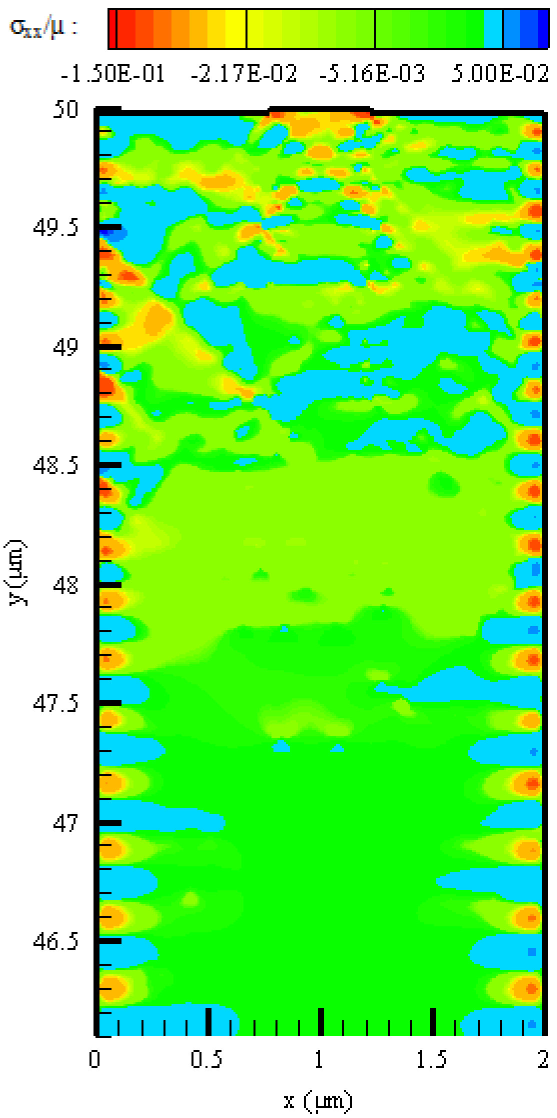

Figure 5.10. Distribution of the lateral stress at the indentation depth ($u = 0.16$ µm) for the case: $AS/w = 0.44/2$.

Now let's check the case when the distance between adjacent asperities is equal to the size of the asperity, *AS/w* = 1/2. Two unit cells are considered, *w* = 8 µm and *w* = 4 µm. High tensile stresses are developed under the free surface for both cases. Here, the bulk material has undergone a much larger bulk compressions than in the cases where the ratio of the contact to the unit cell width is small, e.g. *AS/w* =1/9.

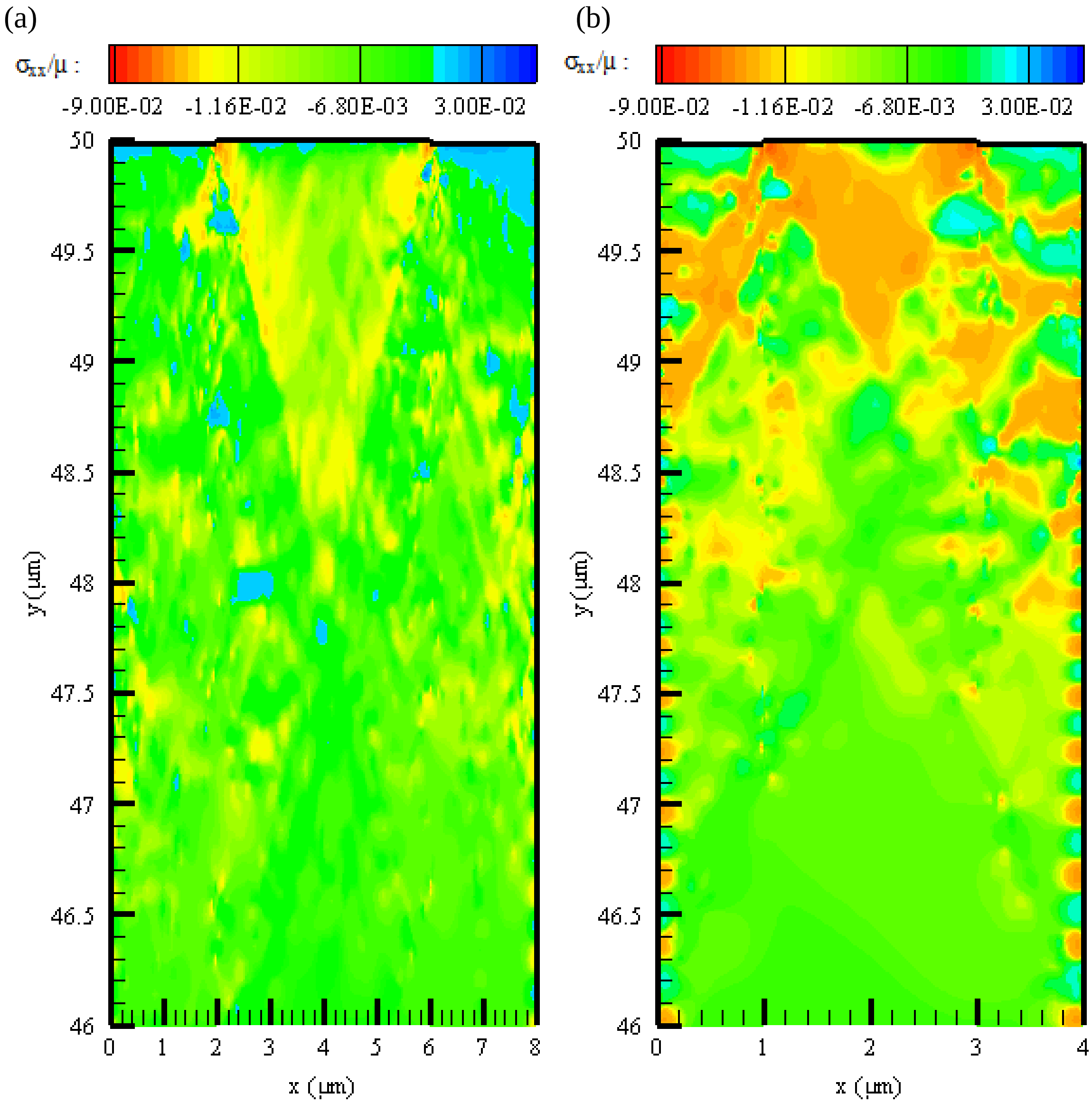

Figure 5.11. Distribution of the lateral stress at the indentation depth (*u* = 0.16 µm) for the cases: (a) *AS/w* = 4/8, and (b) *AS/w* = 2/4.

In terms of internal stresses, we can differentiate between two modes. For cases of small asperity width to unit cell width ratio, *AS/w*, there are tensile spots distributed within the compressive zone under the indented surface. These tensile spots become more localized at the center of the cell as the ratio decreases, e.g *AS/w* =0.44/8. However, when the ratio of the asperity width to the unit cell width is large, e.g. *AS/w* = 1/2, the stresses are predominately compressive under the indented surface. In Fig. 5.12, surface profiles for the two cases that represent small and large ratios are illustrated. For the case of widely spaced asperities (AS/w = 1/18), materials are pushed from underneath the asperity to pile up on the sides which cause the formation of the tensile spots underneath the asperity. However, for the case of closely spaced asperities *AS/w* = 1/2), materials are squeezed down throughout the unit cell which lead to the predominately compressive zone under the indented surface.

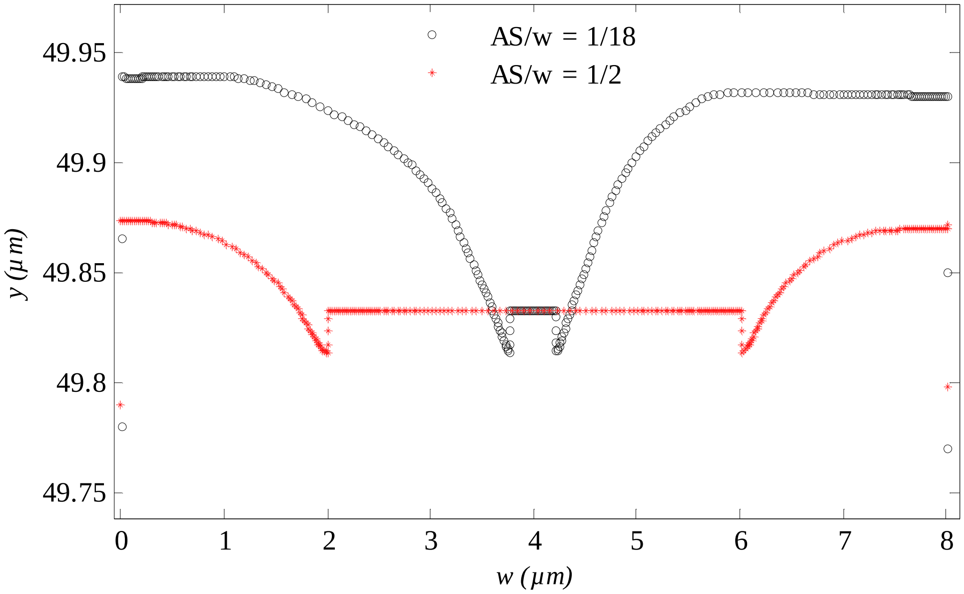

Figure 5.12. Profile of the indented surface at an indentation depth *u* = 0.16 µm for a unit cell of width *w* = 8 µm and two ratios of the asperity width to the unit cell width.

5.3.2.3. Effect of Size and Spacing on the Mean Contact Pressure

In this section, the size effect is analyzed. It is important to note first that in discrete dislocation plasticity, plastic flow is a result of nucleation and motion of dislocations. Let's first fix the ratio of the asperity width to the unit cell width as $AS/w = 1/9$. In Fig. 5.13, the mean contact pressure P_m *is* plotted versus the indentation depth u for several values of AS and w. As shown in Fig. 5.13, as the size decreases, a larger mean contact pressure is required in order for the material to yield. Thus, the Multi-Asperities model exhibits size dependency, where smaller is harder. Similar size effect was observed in Chapter 4 where only nucleation from surface-steps is allowed. That is rough surfaces under contact loading do exhibit size effect, i.e., smaller is harder, regardless of the yielding condition of the bulk material. This is in contrast to conventional plasticity that predicts a size independent response.

Another observation from Fig. 5.13 is that for the case of a relatively larger size ($AS/w = 0.88/8$), the mean contact pressure reaches a plateau at an indentation depth much smaller than the unit cell of width $w = 4$ µm, while for the smallest unit cell (w = 2 µm) the corresponding mean contact pressure did not reach a plateau for the indentation depth simulated. This is due to the fact that the mean contact pressure reaches a plateau when the material bulk yields. Thus, we conclude that for the indentation depth simulated, bulk materials of the two unit cells with widths $w = 2$ µm and $w = 4$ µm haven't yielded yet and the plastic zone is still confined to the zone underneath the surface.

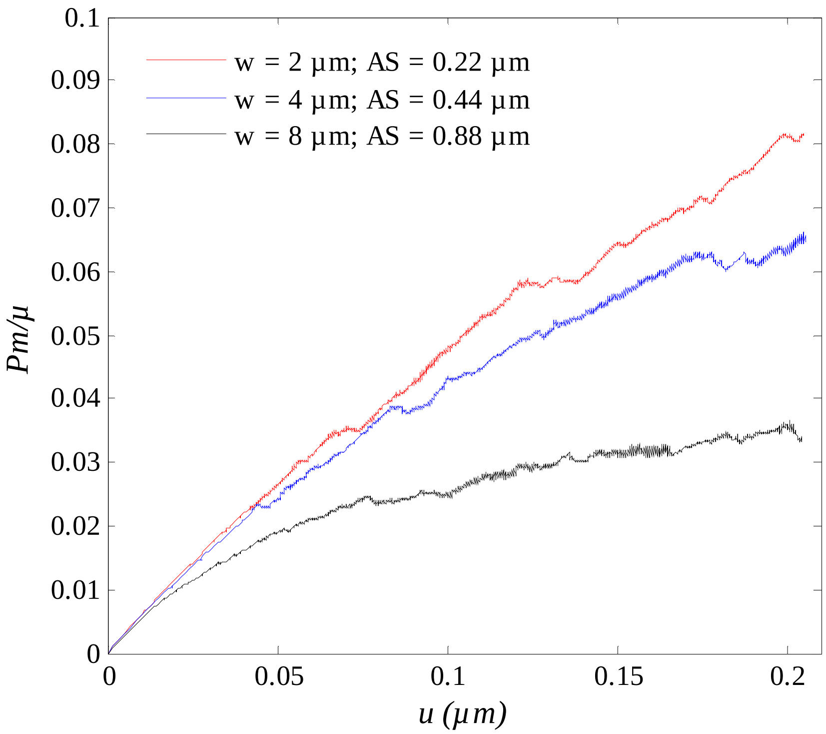

Figure 5.13. Effect of the size of the Multi-Asperities model on the mean contact pressure, P_m.

To check the effect of the ratio of the asperity width to the unit cell width, the size of the unit cell is fixed as w = 8 μm while the asperity size ranges from 1.33 μm to 0.44 μm. Simulation results in Fig. 5.14 reveal that the mean contact pressure is inversely proportional to the size of the asperity. This is due to the following. First, as the size of asperity decreases less bulk sources are in the vicinity of the asperity where the stresses are high and; therefore, fewer dislocations are nucleated. Second, for the case of closely spaced asperity dislocations move throughout the unit cell as shown in Fig. 5.8 leading to the activation of more Bulk sources.

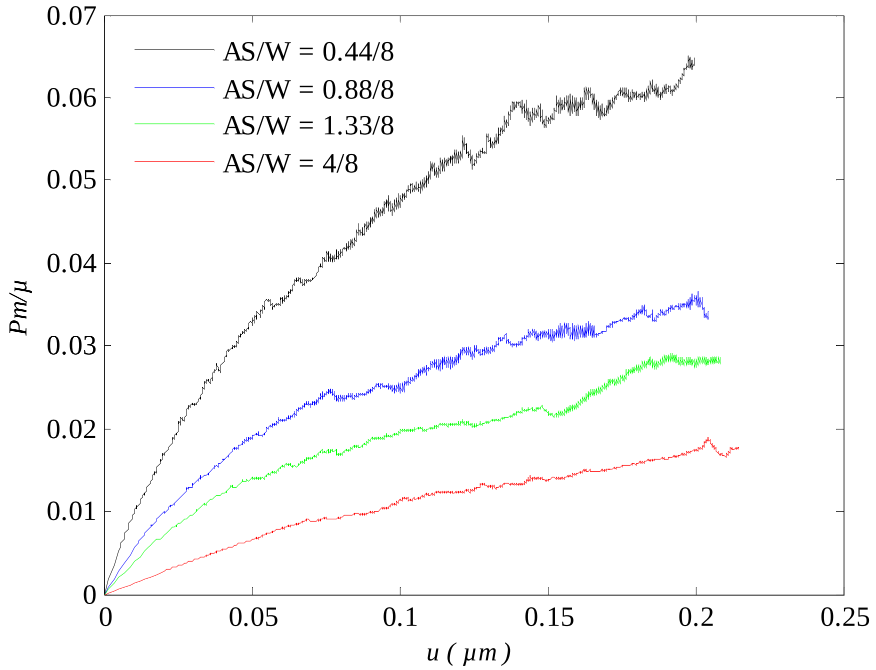

Figure 5.14. Effect of the ratio *AS/w* on the mean contact pressure P_m.

To gain further insights into the size effect, we check the effect of the spacing between adjacent asperities *w*. The size of the asperity is taken to be *AS* = 0.44 μm while *w* is ranging from 8 μm to 2 μm. As shown in Fig. 5.15, the mean contact pressure required for the material to yield increases with the spacing between adjacent asperities. However, closely spaced asperity (*w* = 2 μm) shows hardening effect, which is due to the interaction between neighboring asperities that hinders the plastic flow. It is worth noting that for the cases of widely spaced asperities (*w* = 4 μm and *w* = 8 μm), the mean contact pressure reaches the same plateau at an indentation depth *u* = 0.16 μm. We conclude that the mechanical behavior of the rough surface is controlled not only by the size of the asperity but also by the distance between neighboring asperities.

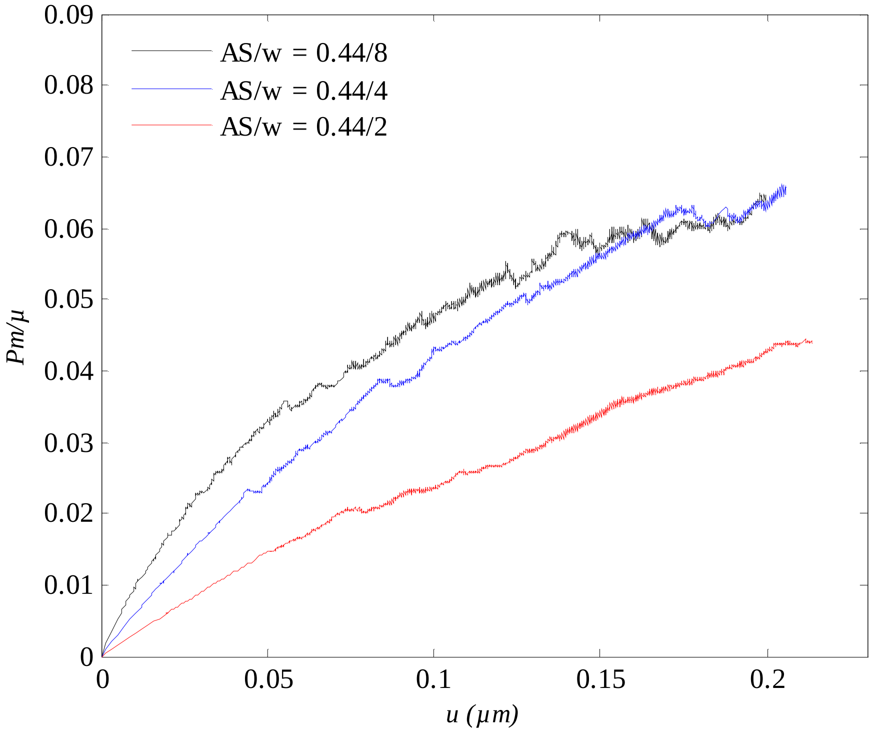

Figure 5.15. Effect of the unit cell width *w*, i.e., asperity spacing on the mean contact pressure P_m.

5.3.2.4. Effect of Bulk Sources on Flattening of Asperities

In this section, the effect of the yield of the material bulk on the flattening of the asperity is discussed. We consider an asperity of fixed size *AS* = 0.44 and a unit cell of width that ranges from 8 µm to 2 µm. Mean contact pressure required to nucleate a dislocation from the surface-steps is computed when only surface sources are activated and then when both surface and bulk sources are activated. As shown in Fig. 5.16, for the case when only surface sources are activated, once the asperity yields there is no need for a significant increase in the mean contact pressure to nucleate subsequent dislocation. This is due to the latent softening phenomenon discussed in Chapter 4. However, when bulk sources are activated, mean contact pressure required to nucleate dislocation from the asperity corners show hardening behavior. This is due to the dislocation nucleated from the bulk sources that glide towards the contact area and block the motion of the dislocation nucleated from the surface sources which prevent nucleation of subsequent dislocations. This hardening behavior becomes more significant in the case of widely spaced asperities. This is due to the arrays of dislocations that pile up beneath the surface.

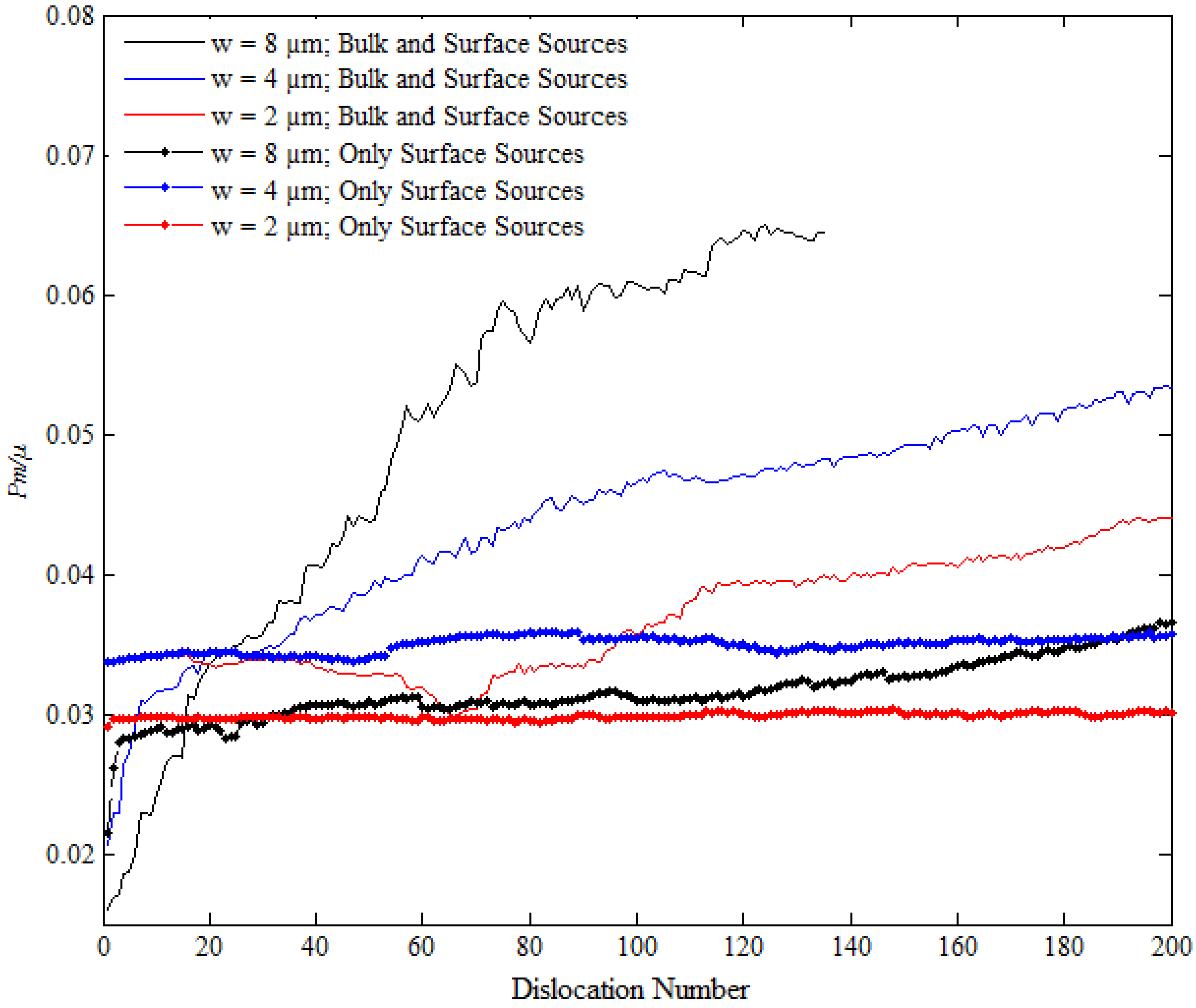

Figure 5.16. Mean Pressure, P_m, required to nucleate dislocations from surface-steps versus number of dislocations for an asperity of size *AS* = 0.44 µm.

5.4. Conclusion

In this chapter, discrete dislocation studies are carried out for the Multi-Asperities model under contact loading taking into consideration the yield of both material bulk and material surface. Deformation patterns were analyzed for two single crystals: one with two symmetric slip systems and another with three slip systems. The following conclusions are drawn:

- For the single crystal with symmetric slip systems inclined at angles $\theta = -\pi/4$ and $\theta = -3\pi/4$ from the x axis, materials are inserted within shear bands that emanate from the surface asperity and propagate towards the bulk. This is similar to the case when only surface sources are activated. However, the magnitude of compressive stresses within the shear bands is higher in the latter case.
- For the single crystal with symmetric slip systems inclined at angles $\theta = -\pi/4$, $\theta = -3\pi/4$ and $\theta = 0$ from the x axis, two deformation modes are identified depending on the ratio of the asperity width to the asperity spacing. For small ratios, plastic deformation is localized in the central zone of the unit cell where materials are squeezed vertically while on the opposite sides of the asperities, materials pile up. Tensile spots develop within the compressive zone underneath the asperity. These tensile spots become more prominent with the asperity spacing. For large ratios, material bulk experiences plain strain compression throughout the width of the unit cell, where the amount of the material pile-up is much smaller than in the cases of large ratios.
- In contrast to the case when only surface sources are activated, no high tensile spots at the corners of the asperity were observed. However, our model does not take into consideration creation of surface-steps due to dislocation annihilation at the surface. These surface-steps may become sources for dislocation nucleation and if the distance between the neighboring steps is

large enough, dislocation may segregate into pro-load and anti-load dislocations leading to the formation of the high tensile spots.

- In contrast to the continuum plasticity that is size independent, our discrete dislocation analysis predicts size dependency where smaller is harder.

CHAPTER 6

CONCLUSION

6.1. Research Summary

Almost all mechanical components fail first at their surfaces. Understanding mechanical behavior of material surfaces is very crucial in devising surface treatment techniques that can be used to enhance the mechanical properties of the surface and; therefore, of the overall material. Surface treatment via severe plastic deformation is one of these techniques that have been used recently to enhance the properties of material surfaces. Materials treated via severe plastic deformation have developed nanolayers underneath the surface. The driving mechanism behind this phenomenon is dislocation interaction and pattern formation underneath the surface.

The main objective of this dissertation is to shed some light on dislocation behavior and dislocation pattern formation underneath rough surfaces. For this purpose, we have developed a boundary element technique that takes into consideration image forces due to dislocations in finite bodies. We have developed a set of complex variable boundary integral equations that can be used to solve discrete dislocation boundary value problems in a direct manner. We developed numerical schemes that can be used to construct a linear system of equations. The linear system of equations is solved for the unknown boundary values. We also developed boundary integral equations that can be used to calculate stresses at internal domain points. The kernels of these integral equations have ($1/r$) singularity in contrast to the kernels of the integrals in the conventional boundary element formulation that have ($1/r^2$) singularity. Thus, the new formulation eliminates the so called boundary layer effect.

We have devised a simple geometrical model that idealizes rough surfaces as an infinite periodic array of asperities of rectangular shapes (see Fig. 4.1). In conjunction with the boundary element technique, a unit cell model is constructed. The unit cell model takes into consideration effect of neighboring asperities via periodic boundary conditions that are applied to the opposite sides of the unit cell.

We have adopted two approaches. In the first approach, we only considered nucleation from surface-steps. Simulations results revealed two phenomena depending on the asperity width and spacing.

- If the width of the asperity is small enough, dislocations nucleated from opposite corners form dipolar bands and move together towards the bulk. Thus, material experiences shear band-like deformation. These shear bands accommodate high compressive stresses.
- If the size of the asperity is large enough, dislocations segregate into pro-load and anti load types. The anti-load dislocations pile up underneath the surface causing high tensile spots in the vicinity of the asperity under the free surface. These tensile spots are much localized and may cause wear of the material surface.

In the second approach, yield of both material bulk and material surface is considered. Dislocations nucleated from bulk sources that glide towards the surface play a dual role. First, they form slip bands that change the morphology of the surface. Second, they accommodate the contact loading and relieve the compressive stresses that develop in form of shear bands when only surface sources are activated. This is more significant for the case of large ratio of the asperity width to the asperity spacing, where we observed materials pile up to the sides of the asperity and materials sink in beneath the asperity (Fig. 5.12). Also, we did not observe tensile spots underneath the surface when bulk sources are activated.

In terms of dislocation nucleation from surface-steps, the bulk dislocations block the motion of the surface dislocations. Thus, dislocations nucleated from surface asperities pile up underneath the surface which prevents nucleation of subsequent dislocations from the surface sources. Hence, surface asperities show hardening behavior in the case when bulk sources are activated. Moreover, when the asperities are widely spaced, plastic zone is more localized beneath the surface and where dislocation density is high. This may be very important for the severe plastic deformation technique that favors high dislocation density.

6.2. Concluding Remarks

- As discussed in Chapter 4, the latent softening phenomenon observed in our simulations depends mainly on the nucleation criterion. The Rice-Thomson criterion [52] adopted in this dissertation to model dislocation nucleation from surface-steps depends mainly on the driving force at a distance η from the surface-step. However, there is no consensus that the Peach-Koehler force is the driving force for dislocation nucleation from surfaces [78]. However, more details of the dislocation nucleation process may be captured by adopting the Peierls-Nabarro model [79,80]. In the framework of the Peierls-Nabarro model, the solid is divided by the slip plane of the dislocation into two half-space linear elastic continua, which have a disregistry relative to each other and are connected by a nonlinear potential force. Thus, it incorporates atomic level processes into a continuum framework. Rice [53] has proposed a more rigorous model in which the displacement discontinuity along the slip plane is defined as the inelastic displacement rather than the total displacement between the two adjacent atomic layers long the slip plane. In this model, the embryonic dislocation profile is characterized as a distribution of interplanar inelastic displacements. Thus, in order to study dislocation nucleation, the inelastic relative displacements have to be calculated.

- Dislocations nucleated from bulk sources form slip bands that may change the morphology of the free surface and thus leading to the creation of new surface-steps that may become sources for nucleation of dislocations. Also, taking into consideration the change in heights of the surface-steps due to nucleation of dislocation may be important to study flattening of asperities at very small scales. An adaptive mesh technique is needed to refine the mesh in the vicinity of the newly created surface-steps and to account for the change in heights of surface-steps.
- It is worth looking more into the formation of tensile spots that develop when only surface sources are activated. In severe plastic deformation, e.g. shot peening, repetitive loading is applied randomly but statistically uniform. So the question is, will these hot spots smear out and form a tensile layer under the free surface or disappear in the compressive zone.
- Two-dimensional discrete dislocation studies have focused on the collective behavior of dislocations where the long range interactions of dislocations play the major role in determining the mechanical behavior of materials. However, at very small scales, where materials such as micron-sized pillars and thin film are relatively free of dislocations and the size of a dislocation loop becomes comparable to the size of the material, accurate modeling of dislocation mobility, dislocation nucleation and mutual interactions of dislocation cores become of a great importance to study the onset of the plastic deformation. Thus, if two-dimensional discrete dislocation plasticity is the method of choice, constitutive rules are needed in order to get better understanding of plastic

deformation in small volumes. Benzerga and his collaborators [81] have proposed semi-physical constitutive rules that have been used in the so called 2.5D discrete dislocation plasticity.

APPENDIX

A. Boundary Integral Equations Based on u and t

In Chapter 2, boundary integral equations are derived in terms of d**u**/ds and **t** along the boundary. In this Appendix, boundary integral equations are derived in terms of **u** and **t**.

In Eq. (2.9), the resultant forces **T** can be replaced by tractions $\mathbf{t} = (t_x, t_y, t_z)^{\mathrm{T}} = d\mathbf{T}/ds$, by integrating by part,

$$\begin{aligned}\mathbf{f}\big|_z = \frac{1}{2\pi}\oint_{\partial\Omega} &\left\langle (C + p_\alpha S)/(\varsigma_\alpha - z_\alpha)\right\rangle \cdot \mathbf{L}^{-1} \cdot (\mathbf{B} + \overline{\mathbf{B}})^{-1} \cdot \mathbf{u}\big|_\varsigma \, ds + \\ &\frac{1}{2\pi i}\oint_{\partial\Omega} \left\langle \ln(\varsigma_\alpha - z_\alpha)\right\rangle \cdot \mathbf{L}^{-1} \cdot (\mathbf{B} + \overline{\mathbf{B}})^{-1} \cdot \overline{\mathbf{B}} \cdot \mathbf{t}\big|_\varsigma \, ds\end{aligned} \tag{A.1}$$

where the single-valued branch-cut of $\ln(\varsigma_\alpha - z_\alpha)$ in z_α-plane is a line from z_α and passing a point on the boundary ς_α^r, so that the argument of $(\varsigma_\alpha - z_\alpha)$ is from $\arg(\varsigma_\alpha^{(r)} - z_\alpha)$ to $\arg(\varsigma_\alpha^{(r)} - z_\alpha) + 2\pi$. In deriving the last term of Eq. (A.1), we assume **T** is calculated from the reference point ς^r and the external loads on the boundary are self-equilibrated ($\oint_{\partial\Omega} \mathbf{t} ds = 0$) so that **T** is periodic around the boundary.

Correspondingly, we can express the internal displacement field and stress field by the boundary displacements and tractions, and derive the boundary integral equations that relates **u** and **t** along the boundary.

$$
\begin{aligned}
\mathbf{u}\big|_{z} = \frac{1}{\pi}\mathrm{Re}\Bigg\{ & \oint_{\partial\Omega} \mathbf{A}\cdot\Big\langle (C+p_\alpha S)\big/(\varsigma_\alpha - z_\alpha)\Big\rangle\cdot\mathbf{L}^{-1}\cdot(\mathbf{B}+\overline{\mathbf{B}})^{-1}\cdot\mathbf{u}\big|_{\zeta}\, ds \\
& - i\oint_{\partial\Omega} \mathbf{A}\cdot\big\langle \ln(\varsigma_\alpha - z_\alpha)\big\rangle\cdot\mathbf{L}^{-1}\cdot(\mathbf{B}+\overline{\mathbf{B}})^{-1}\cdot\overline{\mathbf{B}}\cdot\mathbf{t}\big|_{\zeta}\, ds
\end{aligned}
\tag{A.2}
$$

$$
\begin{aligned}
[\sigma_{21},\sigma_{22},\sigma_{23}]^{\mathrm{T}} = \frac{1}{\pi}\mathrm{Re} & \oint_{\partial\Omega} \mathbf{L}\cdot\Big\langle (C+p_\alpha S)\big/(\zeta_\alpha - z_\alpha)^2\Big\rangle\cdot\mathbf{L}^{-1}\cdot(\mathbf{B}+\overline{\mathbf{B}})^{-1}\cdot\mathbf{u}\big|_{\zeta} \\
& + i\mathbf{L}\cdot\big\langle 1\big/(\varsigma_\alpha - z_\alpha)\big\rangle\cdot\mathbf{L}^{-1}\cdot(\mathbf{B}+\overline{\mathbf{B}})^{-1}\cdot\overline{\mathbf{B}}\cdot\mathbf{t}\big|_{\zeta}\Big]ds
\end{aligned}
\tag{A.3a}
$$

$$
\begin{aligned}
[\sigma_{11},\sigma_{12},\sigma_{13}]^{\mathrm{T}} = \frac{1}{\pi}\mathrm{Re} & \oint_{\partial\Omega} \mathbf{L}\cdot\Big\langle (C+p_\alpha S)p_\alpha\big/(\zeta_\alpha - z_\alpha)^2\Big\rangle\cdot\mathbf{L}^{-1}\cdot(\mathbf{B}+\overline{\mathbf{B}})^{-1}\cdot\mathbf{u}\big|_{\zeta} \\
& + i\mathbf{L}\cdot\big\langle p_\alpha\big/(\varsigma_\alpha - z_\alpha)\big\rangle\cdot\mathbf{L}^{-1}\cdot(\mathbf{B}+\overline{\mathbf{B}})^{-1}\cdot\overline{\mathbf{B}}\cdot\mathbf{t}\big|_{\zeta}\Big]ds
\end{aligned}
\tag{A.3b}
$$

The corresponding boundary integral equations that could be used to solve the un-given **u** or **t** along the boundary are

$$
\begin{aligned}
\mathbf{u}\big|_{\varsigma_0} = \frac{2}{\pi}\mathrm{Re}\Bigg\{ & \oint_{\partial\Omega} [\mathbf{A}\cdot\Big\langle (C+p_\alpha S)\big/(\varsigma_\alpha - \varsigma_\alpha^0)\Big\rangle\cdot\mathbf{L}^{-1}\cdot(\mathbf{B}+\overline{\mathbf{B}})^{-1}\cdot\mathbf{u}\big|_{\zeta} \\
& - i\mathbf{A}\cdot\Big\langle \ln(\varsigma_\alpha - \varsigma_\alpha^0)\Big\rangle\cdot\mathbf{L}^{-1}\cdot(\mathbf{B}+\overline{\mathbf{B}})^{-1}\cdot\overline{\mathbf{B}}\cdot\mathbf{t}\big|_{\zeta}\,]ds\Bigg\}
\end{aligned}
\tag{A.4}
$$

The branch cut for each logarithm function is from ς_α^0 and pointing outward, (Fig. A.1b), not intersecting the other part of the boundary. Using the limiting technique in Section 4.4, the integral expressions can be deduced for the isotropic materials. It is important to note that by extracting the real parts of the right hand side of Eqs. (A.3) and (A.4), we can obtain the boundary integral equations for the displacement and stresses used in the conventional boundary element method.

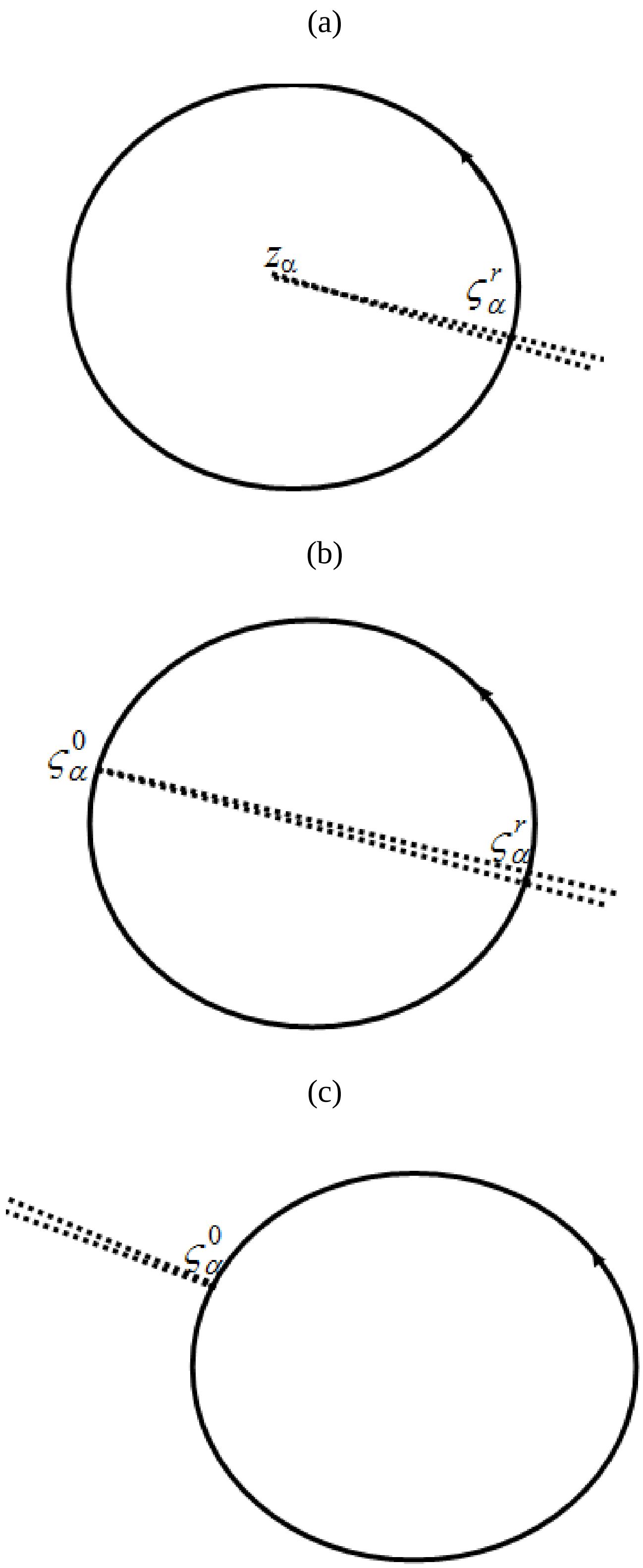

Figure A.1. The branch cuts of logarithmic functions.

B. Explicit Expressions for the Numerical Schemes in Chapter 2

Denote by $r_{21}^{(k)}$ the length of the boundary element $(\zeta_2\zeta_1)^{(k)}$.

$$H_c^2(\zeta_2^{(k)},\zeta_1^{(k)},\zeta_0^{(m)}) = \frac{r_{21}^{(k)}}{(\zeta_2^{(k)}-\zeta_1^{(k)})}\{1-\frac{(\zeta_1^{(k)}-\zeta_0^{(m)})}{(\zeta_2^{(k)}-\zeta_1^{(k)})}\ln(\frac{\zeta_2^{(k)}-\zeta_0^{(m)}}{\zeta_1^{(k)}-\zeta_0^{(m)})}\}$$

$$\begin{aligned}H_v^2(\zeta_2^{(k)},\zeta_1^{(k)},\zeta_0^{(m)}) &= \frac{r_{21}^{(k)}}{(\zeta_2^{(k)}-\zeta_1^{(k)})}\{-\frac{(y_2^{(k)}-y_1^{(k)})}{(\zeta_2^{(k)}-\zeta_1^{(k)})}-\ln(\frac{\zeta_2-\zeta_0^{(m)}}{\zeta_1^{(k)}-\zeta_0^{(m)}}).[\frac{(y_1^{(k)}-y_0^{(m)})}{(\zeta_2^{(k)}-\zeta_1^{(k)})}\\ &\quad -2\frac{(y_2^{(k)}-y_1^{(k)})(\zeta_1^{(k)}-\zeta_0^{(m)})}{(\zeta_2^{(k)}-\zeta_1^{(k)})^2}]-\frac{(y_2^{(k)}-y_0^{(m)})(\zeta_1^{(k)}-\zeta_0^{(m)})}{(\zeta_2^{(k)}-\zeta_1^{(k)})(\zeta_2^{(k)}-\zeta_0^{(m)})}+\frac{(y_1^{(k)}-y_0^{(m)})}{(\zeta_2^{(k)}-\zeta_1^{(k)})}\}\end{aligned}$$

$$H_c^1(\zeta_2^{(k)},\zeta_1^{(k)},\zeta_0^{(m)}) = \frac{r_{21}^{(k)}}{(\zeta_2^{(k)}-\zeta_1^{(k)})}\ln(\frac{\zeta_2^{(k)}-\zeta_0^{(m)}}{\zeta_1^{(k)}-\zeta_0^{(m)}})-H_c^2(\zeta_2^{(k)},\zeta_1^{(k)},\zeta_0^{(m)})$$

$$H_v^1(\zeta_2^{(k)},\zeta_1^{(k)},\zeta_0^{(m)}) = \frac{r_{21}^{(k)}}{(\zeta_2^{(k)}-\zeta_1^{(k)})}\{\frac{(y_2^{(k)}-y_0^{(k)})}{(\zeta_2^{(k)}-\zeta_0^{(m)})}-\frac{(y_1^{(k)}-y_0^{(k)})}{(\zeta_1^{(k)}-\zeta_0^{(m)})}-\ln(\frac{\zeta_2^{(k)}-\zeta_0^{(m)}}{\zeta_1^{(k)}-\zeta_0^{(m)}}).\frac{(y_2^{(k)}-y_1^{(k)})}{(\zeta_2^{(k)}-\zeta_1^{(k)})}-H_v^2(\zeta_2^{(k)},\zeta_1^{(k)},\zeta_0^{(m)})$$

$$\begin{aligned}G_c^2(\zeta_2^{(k)},\zeta_1^{(k)},\zeta_0^{(m)}) &= \frac{r_{21}^{(k)}}{(\zeta_2^{(k)}-\zeta_1^{(k)})^2}\{\ln(\zeta_2^{(k)}-\zeta_0^{(m)}).[\frac{1}{2}(\zeta_2^{(k)}-\zeta_0^{(m)})^2-(\zeta_2^{(k)}-\zeta_0^{(m)})(\zeta_1^{(k)}-\zeta_0)]\\ &\quad +\frac{1}{2}(\zeta_1^{(k)}-\zeta_0^{(m)})^2.\ln(\zeta_1^{(k)}-\zeta_0^{(m)})-\frac{1}{4}(\zeta_2^{(k)}-\zeta_0^{(m)})^2-\frac{3}{4}(\zeta_1^{(k)}-\zeta_0^{(m)})^2\\ &\quad +(\zeta_2^{(k)}-\zeta_0^{(m)})(\zeta_1^{(k)}-\zeta_0^{(m)})\}\end{aligned}$$

$$\begin{aligned}G_v^2(\zeta_2^{(k)},\zeta_1^{(k)},\zeta_0^{(m)}) &= \frac{r_{21}^{(k)}}{(\zeta_2^{(k)}-\zeta_1^{(k)})^2}\{\ln(\zeta_2^{(k)}-\zeta_0^{(m)}).[(\zeta_2^{(k)}-\zeta_1^{(k)})(y_2^{(k)}-y_0^{(m)})-(y_1^{(k)}-y_0^{(m)})(\zeta_2^{(k)}-\zeta_0^{(m)})\\ &\quad -\frac{(\zeta_2^{(k)}-\zeta_0^{(m)})^2(y_2^{(k)}-y_1^{(k)})}{(\zeta_2^{(k)}-\zeta_1^{(k)})}+2\frac{(\zeta_2^{(k)}-\zeta_0^{(m)})(\zeta_1^{(k)}-\zeta_0^{(m)})(y_2^{(k)}-y_1^{(k)})}{(\zeta_2^{(k)}-\zeta_1^{(k)})}]\\ &\quad +\ln(\zeta_1^{(k)}-\zeta_0^{(m)}).[(\zeta_1^{(k)}-\zeta_0^{(m)})(y_1^{(k)}-y_0^{(m)})-\frac{(\zeta_1^{(k)}-\zeta_0^{(m)})^2(y_2^{(k)}-y_1^{(k)})}{(\zeta_2^{(k)}-\zeta_1^{(k)})}]\\ &\quad +\frac{1}{2}\frac{(y_2^{(k)}-y_1^{(k)})}{(\zeta_2^{(k)}-\zeta_1^{(k)})}[(\zeta_2^{(k)}-\zeta_0^{(m)})^2+3(\zeta_1^{(k)}-\zeta_0^{(m)})^2-4(\zeta_2^{(k)}-\zeta_0^{(m)})(\zeta_1^{(k)}-\zeta_0^{(m)})]\\ &\quad +(y_1^{(k)}-y_0^{(m)})(\zeta_2^{(k)}-\zeta_1^{(k)})\}\end{aligned}$$

$$G_c^1(\zeta_2^{(k)},\zeta_1^{(k)},\zeta_0^{(m)})=\frac{r_{21}^{(k)}}{(\zeta_2^{(k)}-\zeta_1^{(k)})}\{[\ln(\zeta_2^{(k)}-\zeta_0^{(m)})-1](\zeta_2^{(k)}-\zeta_0^{(m)})-[\ln(\zeta_1^{(k)}-\zeta_0^{(m)})-1](\zeta_1^{(k)}-\zeta_0^{(m)})\}$$

$$-G_c^2(\zeta_2^{(k)},\zeta_1^{(k)},\zeta_0^{(m)})$$

$$H_c^2(\zeta_2^{(k)},\zeta_1^{(k)},\zeta_0^{(m)})=\frac{r_{21}^{(k)}}{(\zeta_2^{(k)}-\zeta_1^{(k)})}\{1-\frac{(\zeta_1^{(k)}-\zeta_0^{(m)})}{(\zeta_2^{(k)}-\zeta_1^{(k)})}\ln(\frac{\zeta_2^{(k)}-\zeta_0^{(m)}}{\zeta_1^{(k)}-\zeta_0^{(m)}})\}$$

$$H_v^2(\zeta_2^{(k)},\zeta_1^{(k)},\zeta_0^{(m)})=\frac{r_{21}^{(k)}}{(\zeta_2^{(k)}-\zeta_1^{(k)})}\{-\frac{(y_2^{(k)}-y_1^{(k)})}{(\zeta_2^{(k)}-\zeta_1^{(k)})}-\ln(\frac{\zeta_2-\zeta_0^{(m)}}{\zeta_1^{(k)}-\zeta_0^{(m)}}).[\frac{(y_1^{(k)}-y_0^{(m)})}{(\zeta_2^{(k)}-\zeta_1^{(k)})}$$

$$-2\frac{(y_2^{(k)}-y_1^{(k)})(\zeta_1^{(k)}-\zeta_0^{(m)})}{(\zeta_2^{(k)}-\zeta_1^{(k)})^2}]-\frac{(y_2^{(k)}-y_0^{(m)})(\zeta_1^{(k)}-\zeta_0^{(m)})}{(\zeta_2^{(k)}-\zeta_1^{(k)})(\zeta_2^{(k)}-\zeta_0^{(m)})}+\frac{(y_1^{(k)}-y_0^{(m)})}{(\zeta_2^{(k)}-\zeta_1^{(k)})}\}$$

$$H_c^1(\zeta_2^{(k)},\zeta_1^{(k)},\zeta_0^{(m)})=\frac{r_{21}^{(k)}}{(\zeta_2^{(k)}-\zeta_1^{(k)})}\ln(\frac{\zeta_2^{(k)}-\zeta_0^{(m)}}{\zeta_1^{(k)}-\zeta_0^{(m)}})-H_c^2(\zeta_2^{(k)},\zeta_1^{(k)},\zeta_0^{(m)})$$

$$H_v^1(\zeta_2^{(k)},\zeta_1^{(k)},\zeta_0^{(m)})=\frac{r_{21}^{(k)}}{(\zeta_2^{(k)}-\zeta_1^{(k)})}\{\frac{(y_2^{(k)}-y_0^{(k)})}{(\zeta_2^{(k)}-\zeta_0^{(m)})}-\frac{(y_1^{(k)}-y_0^{(k)})}{(\zeta_1^{(k)}-\zeta_0^{(m)})}-\ln(\frac{\zeta_2^{(k)}-\zeta_0^{(m)}}{\zeta_1^{(k)}-\zeta_0^{(m)}}).\frac{(y_2^{(k)}-y_1^{(k)})}{(\zeta_2^{(k)}-\zeta_1^{(k)})}-H_v^2(\zeta_2^{(k)},\zeta_1^{(k)},\zeta_0^{(m)})$$

$$G_c^2(\zeta_2^{(k)},\zeta_1^{(k)},\zeta_0^{(m)})=\frac{r_{21}^{(k)}}{(\zeta_2^{(k)}-\zeta_1^{(k)})^2}\{\ln(\zeta_2^{(k)}-\zeta_0^{(m)}).[\frac{1}{2}(\zeta_2^{(k)}-\zeta_0^{(m)})^2-(\zeta_2^{(k)}-\zeta_0^{(m)})(\zeta_1^{(k)}-\zeta_0)]$$

$$+\frac{1}{2}(\zeta_1^{(k)}-\zeta_0^{(m)})^2.\ln(\zeta_1^{(k)}-\zeta_0^{(m)})-\frac{1}{4}(\zeta_2^{(k)}-\zeta_0^{(m)})^2-\frac{3}{4}(\zeta_1^{(k)}-\zeta_0^{(m)})^2$$

$$+(\zeta_2^{(k)}-\zeta_0^{(m)})(\zeta_1^{(k)}-\zeta_0^{(m)})\}$$

$$G_v^2(\zeta_2^{(k)},\zeta_1^{(k)},\zeta_0^{(m)})=\frac{r_{21}^{(k)}}{(\zeta_2^{(k)}-\zeta_1^{(k)})^2}\{\ln(\zeta_2^{(k)}-\zeta_0^{(m)}).[(\zeta_2^{(k)}-\zeta_1^{(k)})(y_2^{(k)}-y_0^{(m)})-(y_1^{(k)}-y_0^{(m)})(\zeta_2^{(k)}-\zeta_0^{(m)})$$

$$-\frac{(\zeta_2^{(k)}-\zeta_0^{(m)})^2(y_2^{(k)}-y_1^{(k)})}{(\zeta_2^{(k)}-\zeta_1^{(k)})}+2\frac{(\zeta_2^{(k)}-\zeta_0^{(m)})(\zeta_1^{(k)}-\zeta_0^{(m)})(y_2^{(k)}-y_1^{(k)})}{(\zeta_2^{(k)}-\zeta_1^{(k)})}]$$

$$+\ln(\zeta_1^{(k)}-\zeta_0^{(m)}).[(\zeta_1^{(k)}-\zeta_0^{(m)})(y_1^{(k)}-y_0^{(m)})-\frac{(\zeta_1^{(k)}-\zeta_0^{(m)})^2(y_2^{(k)}-y_1^{(k)})}{(\zeta_2^{(k)}-\zeta_1^{(k)})}]$$

$$+\frac{1}{2}\frac{(y_2^{(k)}-y_1^{(k)})}{(\zeta_2^{(k)}-\zeta_1^{(k)})}[(\zeta_2^{(k)}-\zeta_0^{(m)})^2+3(\zeta_1^{(k)}-\zeta_0^{(m)})^2-4(\zeta_2^{(k)}-\zeta_0^{(m)})(\zeta_1^{(k)}-\zeta_0^{(m)})]$$

$$+(y_1^{(k)}-y_0^{(m)})(\zeta_2^{(k)}-\zeta_1^{(k)})\}$$

$$G_c^1(\zeta_2^{(k)},\zeta_1^{(k)},\zeta_0^{(m)})=\frac{r_{21}^{(k)}}{(\zeta_2^{(k)}-\zeta_1^{(k)})}\{[\ln(\zeta_2^{(k)}-\zeta_0^{(m)})-1](\zeta_2^{(k)}-\zeta_0^{(m)})-[\ln(\zeta_1^{(k)}-\zeta_0^{(m)})-1](\zeta_1^{(k)}-\zeta_0^{(m)})\}$$

$$-G_c^2(\zeta_2^{(k)},\zeta_1^{(k)},\zeta_0^{(m)})$$

$$G_v^1(\zeta_2^{(k)},\zeta_1^{(k)},\zeta_0^{(m)})=\frac{r_{21}^{(k)}}{(\zeta_2^{(k)}-\zeta_1^{(k)})}\{\ln(\zeta_2^{(k)}-\zeta_0^{(m)}).[(y_2^{(k)}-y_0^{(m)})-\frac{(\zeta_2^{(k)}-\zeta_0^{(m)})(y_2^{(k)}-y_1^{(k)})}{(\zeta_2^{(k)}-\zeta_1^{(k)})}]$$

$$-\ln(\zeta_1^{(k)}-\zeta_0^{(m)}).[(y_1^{(k)}-y_0^{(m)})-\frac{(\zeta_1^{(k)}-\zeta_0^{(m)})(y_2^{(k)}-y_1^{(k)})}{(\zeta_2^{(k)}-\zeta_1^{(k)})}]$$

$$+\frac{(\zeta_2^{(k)}-\zeta_1^{(k)})(y_2^{(k)}-y_1^{(k)})}{(\zeta_2^{(k)}-\zeta_1^{(k)})}\}-G_v^2(\zeta_2^{(k)},\zeta_1^{(k)},\zeta_0^{(m)})$$

$$N_c^2(\zeta_2^{(k)},\zeta_1^{(k)},\zeta_0^{(m)})=\frac{r_{21}^{(k)}i}{(\zeta_2^{(k)}-\zeta_1^{(k)})}\{1+\frac{(\zeta_1^{(k)}-\zeta_0^{(m)})}{(\zeta_2^{(k)}-\zeta_1^{(k)})}\ln(\frac{\zeta_2^{(k)}-\zeta_0^{(m)}}{\zeta_1^{(k)}-\zeta_0^{(m)}})\}$$

$$N_v^2(\zeta_2^{(k)},\zeta_1^{(k)},\zeta_0^{(m)})=\frac{r_{21}^{(k)}}{(\zeta_2^{(k)}-\zeta_1^{(k)})}\{\ln(\frac{\zeta_2^{(k)}-\zeta_0^{(m)}}{\zeta_1^{(k)}-\zeta_0^{(m)}}).[\frac{(\zeta_1^{(k)}-\zeta_0^{(m)})+(y_1^{(k)}-y_0^{(m)})i}{(\zeta_2^{(k)}-\zeta_1^{(k)})}-2\frac{(y_2^{(k)}-y_1^{(k)})(\zeta_1^{(k)}-\zeta_0^{(m)})}{(\zeta_2^{(k)}-\zeta_1^{(k)})^2}i]$$

$$+\frac{(y_2^{(k)}-y_0^{(m)})(\zeta_1^{(k)}-\zeta_0^{(m)})}{(\zeta_2^{(k)}-\zeta_1^{(k)})(\zeta_2^{(k)}-\zeta_0^{(m)})}i-\frac{(y_1^{(k)}-y_0^{(m)})}{(\zeta_2^{(k)}-\zeta_1^{(k)})}i+\frac{(x_2^{(k)}-x_1^{(k)})}{(\zeta_2^{(k)}-\zeta_1^{(k)})}\}$$

$$N_c^1(\zeta_2^{(k)},\zeta_1^{(k)},\zeta_0^{(m)})=\frac{-r_{21}^{(k)}i}{(\zeta_2^{(k)}-\zeta_1^{(k)})}\{1+\frac{(\zeta_2^{(k)}-\zeta_0^{(m)})}{(\zeta_2^{(k)}-\zeta_1^{(k)})}\ln(\frac{\zeta_2^{(k)}-\zeta_0^{(m)}}{\zeta_1^{(k)}-\zeta_0^{(m)}})\}$$

$$N_v^1(\zeta_2^{(k)},\zeta_1^{(k)},\zeta_0^{(m)})=\frac{-r_{21}^{(k)}}{(\zeta_2^{(k)}-\zeta_1^{(k)})}\{\ln(\frac{\zeta_2^{(k)}-\zeta_0^{(m)}}{\zeta_1^{(k)}-\zeta_0^{(m)}}).[\frac{(\zeta_2^{(k)}-\zeta_0^{(m)})+(y_2^{(k)}-y_0^{(m)})i}{(\zeta_2^{(k)}-\zeta_1^{(k)})}-2\frac{(y_2^{(k)}-y_1^{(k)})(\zeta_2^{(k)}-\zeta_0^{(m)})}{(\zeta_2^{(k)}-\zeta_1^{(k)})^2}i]$$

$$+\frac{(y_1^{(k)}-y_0^{(m)})(\zeta_2^{(k)}-\zeta_0^{(m)})}{(\zeta_2^{(k)}-\zeta_1^{(k)})(\zeta_1^{(k)}-\zeta_0^{(m)})}i-\frac{(y_2^{(k)}-y_0^{(m)})}{(\zeta_2^{(k)}-\zeta_1^{(k)})}i+\frac{(x_2^{(k)}-x_1^{(k)})}{(\zeta_2^{(k)}-\zeta_1^{(k)})}\}$$

$$M_c(\zeta_2^{(k)},\zeta_1^{(k)},\zeta_0^{(m)})=\frac{r_{21}^{(k)}}{(\zeta_2^{(k)}-\zeta_1^{(k)})}$$

$$M_v(\zeta_2^{(k)},\zeta_1^{(k)},\zeta_0^{(m)})=\frac{-r_{21}^{(k)}(y_2^{(k)}-y_1^{(k)})}{(\zeta_2^{(k)}-\zeta_1^{(k)})^2}$$

BIBLIOGRAPHY

[1] N. R. Tao, Z. B. Wang, W. P. Tong, M. L. Sui, J. Lu, K. Lu, Acta Mater. **50** (2002) p.4603

[2] G. Liu, S. C. Wang, X. F. Lou, J. Lu and K. Lu, Scripta Mater. **44** (2001) p.1791.

[3] K. Lu and J. Lu, Mater. Sci. Eng. A **375-377** (2004) p.38.

[4] K. Dai and L. Shaw, Mater. Sci. Eng. A **463** (2007) p.46.

[5] X. Y. Wang and D. Y. Li, Wear **255** (2003) p.836.

[6] M. Sato, N. Tsuji, Y. Minamino, Y. Koizumi, Sci. Technol. Adv. Mater. **5** (2004) p.145.

[7] D. A. Hughes and N. Hansen, Phys. Rev. Lett. **87** (2001) p.135503.

[8] J. L. Liu, M. Umemoto, Y. Todaka and K. Tsuchiya, J. Mater. Sci. **42** (2007) p.7716.

[9] S. Bagheri, M. Guagliano, Surf. Eng. **25** (2009) p.3.

[10] B. N. Mordyuk, G. I. Prokopenko, J. Sound Vib. **308** (2007) p.855.

[11] H. Gleiter and Prog. Mater. Sci. **33** (1988) p.223.

[12] C. Suryanarayana, Int. Mater. Rev. **40** (1995) p.41.

[13] K. Lu, Mater. Sci. Eng. R**16** (1996) p.161.

[14] D.G. Morris, Mechanical Behaviour of Nanostructured Materials, Trans.Tech. Publications Ltd., Switzerland (1998) p.70.

[15] S.X. McFadden, R.S. Mishra, R.Z. Valiev, A.P. Zhilyaev, A.K. Mukherjee, Nature **298** (1999) p.684.

[16] L. Lu, M.L. Sui, K. Lu, Science **287** (2000) p.1463.

[17] J.A. Greenwood and J.B.P. Williamson, Proc. Roy. Soc. London A **295** (1966) p.300.

[18] A.Majumdar and B. Bhushan, ASME J. Tribol. **113** (1991) p.1.

[19] I.A. Polonsky and L.M. Keer, ASME J. Tribol. **122** (2000) p.30.

[20] S. Hyun, L. Pei, J.F. Molinari, Physical Review E **70** (2004) 026117.

[21] Ciavarella, M., Demelio, G., Barber, J. R. Jang, Y. H. Proc. R. Soc. A **456** (2000) p.387.

[22] Y.F. Gao and A.F. Bower, Proc. Roy. Soc. London A **462** (2006) p.319.

[23] L. Pei, S. Hyun, J.F. Molinari, and M.O. Robbins, J. Mech. Phys. Solids **53** (2005) p.2385.

[24] N.A. Fleck, G.M. Muller, M.F. Ashby and J.W. Hutchinson, Acta metall. mater. **42** (1994) p.475.

[25] J.S. Stolken and A.G. Evans, Acta Mater. **46** (1998) p.5109.

[26] Q. Ma and D.R. Clarke,J. Mater. Res. **10** (1995) p.853.

[27] W.D. Nix, and H. Gao, J. Mech. Phys. Solids **43** (1998) p.411.

[28] F.G. Swadener, E.P. George and G.M. Pharr , J. Mech. Phys. Solids **50** (2202) p.681.

[30] A. Acharya and J.L. Bassani, J. Mech. Phys. Solids **48** (2000) p.1565.

[31] N.A. Fleck and J.W. Hutchinson, J. Mech. Phys. Solids **49** (2001) p.2245.

[32] M.E. Gurtin, J. Mech. Phys. Solids **50** (2002) p.5.

[33] P. Gudmundson, J. Mech. Phys. Solids **52** (2004) p.1379.

[34] B. Devincre and L.P. Kubin, Modelling Simul. Mater. Sci. Eng. **2** (1994) p.559.

[35] K.W. Schwarz, J. Appl. Phys. **85** (1999) p.108.

[36] H.M. Zbib, T.D. de la Rubia, M. Rhee and J.P. Hirth, J. Nucl. Mater. **276** (2000) p.154.

[37] D. Weygand, L.H. Friedman, E. Van der Giessen and A. Needleman, Modelling Simul. Mater. Sci. Eng. **10** (2002) p.437.

[38] X. Han, N.M. Ghoniem and Z. Wang, Phil. Mag **83** (2003) p.3705.

[39] W. Cai and V.V Bulatov, Mat. Sci. Eng. A **387** (2004) p.277.

[40] I.A. Polonsky and L.M. Keer, J. Tribol. **118** (1996) p.335.

[41] H.G.M. Kreuzer and R. Pippan, Comp. Mech. **33** (2004) p.292.

[42] H.G.M. Kreuzer and R. Pippan, Mat. Sci. Engin. A **400-401** (2005) p.460.

[43] A. Widjaja, E. Van der Giessen, A. Needleman,Mater. Sci. Eng. A **400** (2005) p.456.

[44] D.S. Balint, V.S. Deshpande, A. Needleman, E.Van der Giessen, J. Mech. Phys. Solids **54** (2006) p.2281.

[45] J.A. Zimmerman, C.L. Kelchner, P.A. Klein, J.C. Hamilton, S.M. Foiles, Phys. Rev. Lett. **87** (2001) 165507.

[46] J. Li, K. J. Van Vliet, T. Zhu , S. Yip, S. Suresh, Nature **418** (2002) p.307.

[47] Yu, H.H., Shrotriya, P., Gao, Y.F., Kim, K.-S., J. Mech. Phys. Solids **55** (2007) p.489.

[48] Kim, K.-S., 1980. Ph.D. Thesis, Brown University, Providence, RI.

[49] J.D. Kiely, R.Q. Hwang, J.E. Houston, Phys. Rev. Lett. **81**, (1998) p.4424.

[50] A. Gouldstone, K.J. Van Vliet, S. Suresh, Nature **411** (2001) p.656.

[51] O.R. De la Fuente, J.A. Zimmerman, M.A. Gonza´ lez, J. De la Figuera, J.C. Hamilton, W.-W. Pai , J.M. Rojo, Phys. Rev. Lett. **88** (2002) 036101.

[52] J.R. Rice and R. Thomson, Phil. Mag. **29** (1973) p.73.

[53] J.R. Rice, J. Mech. Phys.Solids **40** (1992) p.271.

[54] J. Knap, K. Sieradzki, Phys. Rev. Lett. **82** (1999) p.1703.

[55] Gao, Y.F., Yu, H.H., Kim, K.-S., 2006b. J. Mech. Phys. Solids **56** (2008) p.2759.

[56] R. Rizzo, Quarterly Journal of Applied Mathematics **25** (1967) p. 83.

[57] N. Ghosh, H. Rajiyah, S. Ghosh and S. Mukherjee, ASME J. Appl. Mech. **53** (1986) p.67

[58] Wu, K.C., Chiu, Y.-T., and Hwu, Z.H., ASME J. Appl. Mech. **59** (1992) p.344.

[59] Okada, H., Rajiyah, H., Atluri, S.N.. Journal of Applied Mechanics, **55** (1988) p.786.

[60] H.H.Yu ,W. Yang, J. Mech. Phys. Solids **43** (1995) p.207.

[61] J.D. Eshelby, W.T. Read and W. Shockley, Acta Metall. **1** (1953) p.251.

[62] A.N. Stroh, Phil. Mag. **7** (1958) p.625.

[63] S.G. Lekhnitskii, Theory of elasticity of an anisotropic body.SanFrancisco, (1953) p.153, Holden-Day.

[64] Z.Suo, Media, Proc. Roy. Soc. Lond. A **427** (1990) p.331.

[65] Brebbia, C.A.(1978), The Boundary Element Method For Engineers, John Wiley and Sons,New York.

[66] R.J. Amodeo and N.M. Ghoniem, Phys. Rev. B **41** (1990) p.6958.

[67] R.J. Amodeo and N.M. Ghoniem, Phys. Rev. B **41** (1990) p.6968.

[68] I. Lepinoux and L.P. Kubin, Scr. Metaii. **21** (1987) p.833.

[69] L.P. Kubin, G. Canova,M. Condat, B. Devincre, V. Pontikis and Y.Bdchet,Nonlinear Phenomena in Marerials Science II ed. G Martin and L.P. Kubin, (Vaduz: Sci-Tech) (1992) p.455.

[70] E. Van der Giessen and A. Needleman, Modelling Simui. Mater. Sci. Eng. **3** (1995) p.689.

[71] V. Lubarda, J.A. Blume and A. Needleman, Acta Metalll. Mater. **41** (1993) 625.

[72] F.R.N. Nabarro, Theory of Crystal Dislocations, Oxford University Press, Oxford, (1967).

[73] J.P. Hirth and J. Lothe, Theory of Dislocations, McGraw-Hill, New York, (1968).

[74] Cleveringa, H.H.M., van der Giessen, E. and Needleman, A., Int. J. Plasticity **15** (1998) p.837.

[75] D.S. Balint, V.S. Deshpande, A. Needleman, E. Van der Giessen, Mater. Sci. Eng. A **400** (2005) p.186.

[76] Z. Suo and J. W. Hutchinson, Int. J. Solids Struct. **25** (1989) p.1337.

[77] J.R. Rice, J. Mech. Phys.Solids **40** (1992) p.239.

[78] Liu, Y., Van der Giessen, E., Needleman, A., Int. J. Solids Struct. **44** (2007) p.1719.

[79] R. Peierls, Proc. Phys. Soc. **52** (1940).p.34.

[80] F.R.N Nabarro, Proc. Phys. Soc. **59** (1947) p.256.

[81] A.A. Benzerga, Y. Bréchet, A. Needleman, E. Van der Giessen, Modelling Simulation Mater. Sci. Eng. **12** (2004), p. 159.